

Air Force Office of Scientific Research (AFOSR)



***Lockheed Martin Aeronautics Company***  
***Pulsed Injection for Nozzle Throat***  
***Area Control***

**Final Technical Report**

**Contract Number F49620-98-C-0016**

**CLIN Sequence No. 0002AA**

20010316 099

**DISTRIBUTION STATEMENT A.**

Approved for public release; distribution is unlimited.

# REPORT DOCUMENTATION PAGE

Public reporting burden for this collection of information is estimated to average 1 hour per response, including the time for reviewing data needed, and completing and reviewing this collection of information. Send comments regarding this burden estimate or any other aspect of this collection of information, including suggestions for reducing this burden, to Washington Headquarters Services, Directorate for Information Operations and Reports (0704-0188), Washington, DC 20540-6001. Respondents should be aware that notwithstanding any other provision of law, no person shall be subject to any penalty for failing to comply with a collection of information if it does not have a valid OMB control number. PLEASE DO NOT RETURN YOUR FORM TO THE ABOVE ADDRESS.

AFRL-SR-BL-TR-01-

ing the  
diting  
200-  
urrent:

1. REPORT DATE (DD-MM-YYYY)

05-02-2001

2. REPORT TYPE

Final Technical Report

0141

March 1998 - December 2000

4. TITLE AND SUBTITLE

Pulsed Injection for Nozzle Throat Area Control

5a. CONTRACT NUMBER

F49620-98-C-0016

5b. GRANT NUMBER

5c. PROGRAM ELEMENT NUMBER

5d. PROJECT NUMBER

5e. TASK NUMBER

5f. WORK UNIT NUMBER

6. AUTHOR(S)

Miller, Daniel N.; Yagle, Patrick J.; Bender, Erich E.; Ginn, K. Brant; Smith, Brian R.

7. PERFORMING ORGANIZATION NAME(S) AND ADDRESS(ES)

Lockheed Martin Aeronautics Company  
Air Vehicle Sciences and Systems  
P.O. Box 748  
Fort Worth, TX 76101  
Attn: Daniel N. Miller, MZ 9333

University of Tennessee Space Institute  
Mechanical and Aerospace Engr. Dept.  
Mail Stop 26  
Tullahoma, TN 37388-8897  
Attn: Ahmad D. Vakili

8. PERFORMING ORGANIZATION REPORT NUMBER

Lockheed Martin Aeronautics  
Company Report No. FZM-8644

9. SPONSORING / MONITORING AGENCY NAME(S) AND ADDRESS(ES)

Air Force Office of Scientific Research  
AFOSR/NA  
801 N. Randolph St., Rm 732  
Arlington, VA 22203-1977  
Attn: Dr. Thomas J. Beutner

10. SPONSOR/MONITOR'S ACRONYM(S)  
AFOSR/NA

11. SPONSOR/MONITOR'S REPORT  
NUMBER(S)

12. DISTRIBUTION / AVAILABILITY STATEMENT

DISTRIBUTION STATEMENT A. Approved for public release; distribution is unlimited.

AIR FORCE OFFICE OF SCIENTIFIC RESEARCH (AFOSR)  
NOTICE OF TRANSMITTAL DTIC. THIS TECHNICAL REPORT  
HAS BEEN REVIEWED AND IS APPROVED FOR PUBLIC RELEASE  
LAW AFR 190-12. DISTRIBUTION IS UNLIMITED.

13. SUPPLEMENTARY NOTES

14. ABSTRACT

Computational fluid dynamics (CFD) and experimental methods were used to investigate two unsteady injection techniques for increasing the penetration and blockage of an injected stream in a confined, expanding crossflow. The obstruction produced by an injected stream is a basic mechanism related to the efficacy of fluidic nozzle control techniques. A CFD simulation methodology was developed for unsteady injection, which showed the effects of grid resolution, turbulence model, and numerical discretization on solution accuracy. CFD simulations were used to explore the basic effects of injector pulsing frequency, Mach number, and geometry on injector-jet trajectory, penetration, diameter, and blockage in a nozzle crossflow. Two actuators were experimentally evaluated for pulsing an injected stream that issues into a nozzle crossflow. CFD simulations were also used to investigate a pulsed-ejection technique, which used a pulsed high-pressure primary stream to boost the entrainment of a co-annular, low-pressure secondary flow. Simulations revealed the effects of primary-jet pulsing frequency and ejector geometry on ejector pumping effectiveness relative to a steady-jet ejector. A simplified CFD model was developed to capture the essential effect of the unsteady primary stream on the secondary flow, without the need of a highly resolved simulation. Results of CFD solutions were compared with available data.

15. SUBJECT TERMS

fluidic nozzle, pulsed injection, jet in crossflow, vortex ring, pulsed ejection, unsteady computational fluid dynamics, CFD simulation and modeling, pulse actuator

16. SECURITY CLASSIFICATION OF:

a. REPORT  
Unclassified

b. ABSTRACT  
Unclassified

c. THIS PAGE  
Unclassified

17. LIMITATION  
OF ABSTRACT

UU

18. NUMBER  
OF PAGES

78

19a. NAME OF RESPONSIBLE PERSON  
Daniel N. Miller

19b. TELEPHONE NUMBER (include area  
code)  
817.935.1132

# ***Pulsed Injection for Nozzle Throat Area Control***

**Final Technical Report**

**Contract Number F49620-98-C-0016**

**CLIN Sequence No. 0002AA**

**05 February 2001**

Releasability of this material under the Freedom of Information Act is subject to the restrictions on release in DoD Regulation 5400.4-R and DoD Directive 5230.25.

Copyright © 2001 by Lockheed Martin Corporation.  
All rights reserved.

This material may be reproduced by or for the U. S. Government pursuant to the copyright license under the clause at DFARS 252.227-7013 (October 1988).

# ***Pulsed Injection for Nozzle Throat Area Control***


**Final Technical Report**

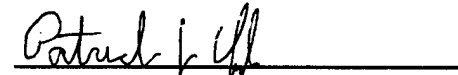
**Contract Number F49620-98-C-0016**


*Prepared by*

  
Daniel N. Miller

*Reviewed by*

  
Jeffrey W. Hamstra

  
Patrick J. Yagle

  
Erich E. Bender

  
K. Brant Ginn

  
Brian R. Smith

## Table of Contents

List of Figures .....	v
Nomenclature .....	vii
Abstract .....	xi
<b>1.0 Introduction .....</b>	<b>1</b>
1.1 Background/Motivation .....	1
1.2 Research Objectives .....	2
1.3 Research Approach Overview .....	2
1.4 Previous Work .....	4
1.4.1 Steady Injection in Crossflow .....	4
1.4.2 Fluidic Jet Control .....	4
1.4.3 Pulsed Injection into a Crossflow .....	6
1.4.4 CFD-Based Simulation of Pulsed Injection .....	7
<b>2.0 A Simulation Methodology for Pulsed Injection Into a Crossflow Using 3-D Unsteady CFD .....</b>	<b>8</b>
2.1 Introduction .....	8
2.2 Experimental Configuration and Measurements .....	8
2.2.1 Test Configuration .....	8
2.2.2 Flow Conditions .....	9
2.2.3 Measurements .....	10
2.3 CFD Methodology .....	10
2.3.1 Discretization .....	10
2.3.2 Turbulence Models .....	10
2.3.3 Solvers .....	10
2.4 Results and Discussion .....	11
2.4.1 Grid and Boundary Conditions .....	11
2.4.2 Temporal Resolution .....	13
2.4.3 Velocity Scaling .....	13
2.4.4 Numerical Simulation of Hot-Film Anemometer .....	14
2.4.5 Effect of Grid Resolution - Steady Injector jet .....	14
2.4.6 Effect of Grid Resolution - Pulsed Injector jet .....	15
2.4.7 Effect of Turbulence Modeling .....	18
2.4.8 Effect of Numerical Discretization .....	19
2.5 Task Summary .....	22
<b>3.0 A Computational Investigation of Pulsed Injection Into a Confined, Expanding Crossflow .....</b>	<b>23</b>
3.1 High-Speed Simulations .....	23
3.2 Effects of Injector-Jet Pulsing Frequency .....	24
3.3 Effects of Injector-Jet Pulsing Mach Number .....	26

3.4	Effects of Injector Jet Geometry .....	28
3.5	Effects of Compressibility .....	30
3.6	Task Summary with Implications for Actuator Requirements .....	32
<b>4.0</b>	<b>A Preliminary Experimental Evaluation of Actuators for Pulsed Injection in the Compressible Flow Regime.....</b>	<b>33</b>
4.1	Nozzle Test Model .....	33
4.2	Pulsing Devices .....	34
4.3	Test Facility.....	36
4.4	Test Approach .....	38
4.5	Results and Discussion .....	39
4.6	Task Summary.....	45
<b>5.0</b>	<b>A Computational Investigation of Pulsed Ejection .....</b>	<b>46</b>
5.1	Pulsed Ejection Technique & Benefits .....	46
5.2	Investigation Approach .....	47
5.3	CFD Investigation .....	48
5.3.1	Steady-Jet Ejector Characteristics.....	48
5.3.2	Pulsed-Jet Ejector: Effect of Frequency.....	49
5.3.3	Pulsed-Jet Ejector: Effect of Geometry.....	51
5.3.4	Comparison of Steady vs. Pulsed Ejector Performance .....	51
5.3.5	Comparison of 3-D and Axisymmetric CFD .....	53
5.4	Preliminary Experimental Investigation.....	55
5.5	Task Summary.....	56
<b>6.0</b>	<b>A Simplified Model of Pulsed Ejection Using 1-D CFD .....</b>	<b>57</b>
6.1	Motivation.....	57
6.2	Governing Equations .....	57
6.3	Viscous Mixing Model .....	59
6.4	Numerical Approach .....	60
6.5	Preliminary Results and Validation .....	60
6.6	Task Summary.....	63
<b>7.0</b>	<b>Overall Project Conclusions.....</b>	<b>64</b>
<b>8.0</b>	<b>Acknowledgements .....</b>	<b>66</b>
<b>9.0</b>	<b>Recommendations for Future Work.....</b>	<b>67</b>
<b>10.0</b>	<b>References.....</b>	<b>69</b>
<b>11.0</b>	<b>Appendix: Test Data Plots .....</b>	<b>72</b>
11.1	Publications .....	72
11.2	Awards Received .....	72
11.3	Transitions.....	72
11.4	Personnel .....	72
11.4.1	Lockheed Martin Aeronautics Company .....	72
11.4.2	University of Tennessee Space Institute.....	73



FZM-8644  
05 February 2001

11.5 Model Drawings.....	74
--------------------------	----

## List of Figures

Figure 1: Steady Injection Schemes in Development for Jet Control in Structurally Fixed Nozzle Systems..	1
Figure 2: Project Overview: Investigation of Unsteady Injection Techniques for Increasing Fluidic Control-Jet Blockage .....	3
Figure 3: Two Promising Techniques for Fixed Nozzle Vectoring Use a Steady Injected Stream to Produce a Fluidic Obstruction.....	5
Figure 4: Schematic of Test Configuration. ....	9
Figure 5: Fine Grid. Injector Jet Orifice Location is Marked in Red. ....	12
Figure 6: Close-up of Fine Grid. Injector Jet Orifice Location is Marked in Red.....	13
Figure 7: Effect of Grid Resolution on Velocity Magnitude Profiles for the Steady Injector Jet.....	15
Figure 8: Three-Dimensional View of Ring Structure as Surfaces of Constant Vorticity Magnitude .....	16
Figure 9: Effect of Grid Resolution on Vorticity Magnitude for Pulsed Injection .....	17
Figure 10: Effect of Grid Resolution on Velocity Magnitude Profiles for the Pulsed Injector Jet, using LES model and Second Order Accuracy.....	18
Figure 11: Effect of Turbulence Model on Velocity Magnitude Profiles. Simulation used Fine Grid and Second Order Accuracy .....	19
Figure 12: Effect of Flux Limiters on Velocity Magnitude Profiles. Simulations used Fine Grid, LES Model, and Second Order Accuracy.....	20
Figure 13: Effect of Order of Accuracy on Velocity Magnitude Profiles. Simulations used Fine Grid, LES Model, with no Flux Limiter .....	21
Figure 14: CFD Simulation Used to Investigate Basic Pulsing Scheme on Injector Jet in Crossflow .....	23
Figure 15: Effect of Pulsing Frequency on Injector-Jet Structure, Penetration, and Blockage (Vorticity Contours: Red-High, Blue-Low).....	24
Figure 16: Effect of Pulsing Frequency and Mach Number on Injector-Jet Penetration Relative to Steady Injection .....	25
Figure 17: Effect of Jet Frequency on Injector-Jet Diameter .....	25
Figure 18: Effect of Pulsing Mach Number on Injector-Jet Structure, Penetration, and Blockage .....	26
Figure 19: Effect of Injector-Jet Pulsing on Entrainment.....	27
Figure 20: Effect of Number of Injection Holes on Penetration .....	28
Figure 21: Effect of Number of Injection Holes on Blockage.....	28
Figure 22: Effect of Injector Angle on Injector-Jet Penetration and Blockage .....	29
Figure 23: Effect of Injector Angle on Injector Jet Penetration .....	30
Figure 24: Comparison of Experimental and CFD-Predicted Penetration .....	30
Figure 25: Effect of Pulsing on Injector-Jet Shock Strength.....	31
Figure 26: Simple Two-Dimensional Nozzle Model.....	33
Figure 27: Injection Orifice Designs .....	34
Figure 28: Two Tested Pulse Generating Devices .....	35

Figure 29: Allied Signal Fluidic Diverter Pulse Valve.....	35
Figure 30: Nozzle Model Installed in UTSI Facility.....	36
Figure 31: "Muffler" Installation Required with Allied Signal Device .....	37
Figure 32: Hot-Film Data from Bench Test of ASFDV .....	39
Figure 33: Comparison of Test and CFD Lower Surface Pressures for $NPR = 2.0$ , No Injection .....	40
Figure 34: Comparison of Test and CFD Lower Surface Pressures for $NPR = 2.0$ , 10% Injection.....	41
Figure 35: Nozzle Discharge Coefficient with Steady Injection for $NPR = 2.0$ .....	41
Figure 36: Effect of Pulsed Injection on Nozzle Discharge Coefficient for $NPR = 2.0$ .....	42
Figure 37: Injection Plenum Pressure with the ASFDV.....	43
Figure 38: Injection Plenum Pressure with the AFIG.....	43
Figure 39: PIV Results for Steady and Pulsed Injection .....	44
Figure 40: Pulsed Ejector Schematic .....	46
Figure 41: Effect of Ejector Length on Frequency Response.....	48
Figure 42: Effect of Mixing Tube Area on Frequency Response.....	49
Figure 43: Effect of Pulsing Frequency on Pumping Effectiveness .....	50
Figure 44: Secondary Mass Flux Time Histories .....	50
Figure 45: Effect of Pulsed-Ejector Geometry on Pumping Effectiveness.....	51
Figure 46: Comparison of Steady and Unsteady Ejector Performance .....	52
Figure 47: 3-D Ejector CFD Solution .....	53
Figure 48: Comparison of Axisymmetric and 3-D CFD Simulations.....	54
Figure 49: Pulsed Ejector Test Apparatus Schematic .....	55
Figure 50: Schematic of Ejector Geometry .....	58
Figure 51: Mass flux and Mach number as a function of time for $c=0.02$ .....	61
Figure 52: Mass flux and Mach number as a function of time for $c=0.002$ .....	62

## Nomenclature

$A$	Area
AFPG	UTSI Axial Flow Pulse Generator
AFRL	Air Force Research Labs
$A_I$	Interface Area Factor
ASFDV	Allied Signal Fluidic Diverter Valve
ASME	American Society of Mechanical Engineers
Axi	Axisymmetric
$c$	Compression Factor
$C_d$	Discharge Coefficient
CFD	Computational Fluid Dynamics
CFL	Courant-Friedrichs-Lewy
$D$	Diameter
$E$	Total Energy
$e$	Internal Energy
$f$	Frequency
$\gamma$	Ratio of Specific Heats
$H$	Height
IR&D	Independent Research and Development
$k$	Turbulent Kinetic Energy
$l$	Turbulent Length Scale
$L$	Length

LES	Large Eddy Simulation
LM	Lockheed Martin
$M$	Mach Number
$\overline{M}$	Mean Mach Number
MPI	Message Passing Interface
$\mu_t$	Turbulent Viscosity
NPR	Nozzle Pressure Ratio
$P, p$	Pressure
PIV	Particle Image Velocimetry
$Pr$	Prandtl Number
$Pr_t$	Turbulent Prandtl Number
PSD	Power Spectral Density
PVM	Parallel Virtual Machine
$q$	Heat Diffusion
RANS	Reynolds Averaged Navier Stokes
$Re$	Reynolds Number
$\rho$	Density
SGS	Symmetric Gauss-Seidel
SIP	Strongly Implicit Procedure
$St$	Strouhal Number
$T$	Temperature
$t$	Time

T/V	Thrust Vectoring
$\tau$	Turbulent Shear Stress
TSI	Thermal Systems Incorporated
$U, u$	Velocity
UAV	Uninhabited Air Vehicle
UTSI	University of Tennessee Space Institute
$V$	Velocity
$V_E$	Viscous Mixing Term, Energy Equation
$V_M$	Viscous Mixing Term, Momentum Equation
$\omega$	Frequency
$W$	Mass Flow
$X$	Axial Distance
$Y$	Vertical Distance
Subscripts	
$e$	Exit Conditions
$ej$	Ejector
$\infty$	Reference or Freestream Conditions
$inj$	Injector Conditions
$jet$	Jet Properties
$m$	Mixing Tube
$p, primary$	Primary Conditions
$ring$	Vortex Ring Properties



FZM-8644  
05 February 2001

*s, secondary*      Secondary Properties

*t*      Total Conditions

## Abstract

Computational fluid dynamics (CFD) and experimental methods were used to investigate two unsteady injection techniques for increasing the penetration and blockage of an injected stream in a confined, expanding crossflow. The obstruction produced by an injected stream is a basic mechanism related to the efficacy of fluidic nozzle control techniques. A CFD simulation methodology was developed for unsteady injection, which showed the effects of grid resolution, turbulence model, and numerical discretization on solution accuracy. CFD simulations were used to explore the basic effects of injector pulsing frequency, Mach number, and geometry on injector-jet trajectory, penetration, diameter, and blockage in a nozzle crossflow. Two actuators were experimentally evaluated for pulsing an injected stream that issues into a nozzle crossflow. CFD simulations were also used to investigate a pulsed-ejection technique, which used a pulsed high-pressure primary stream to boost the entrainment of a co-annular, low-pressure secondary flow. Simulations revealed the effects of primary-jet pulsing frequency and ejector geometry on ejector pumping effectiveness relative to a steady-jet ejector. A simplified CFD model was developed to capture the essential effect of the unsteady primary stream on the secondary flow, without the need of a highly resolved simulation. Results of CFD solutions were compared with available data.

## 1.0 Introduction

### 1.1 Background/Motivation

The weight and cost of tactical aircraft exhaust systems have increased at an alarming rate with the incorporation of features for afterburning, thrust vectoring, and advanced shaping. Historically, afterburning and vectoring have required variation of the nozzle geometry. A typical turbofan engine's nozzle throat area must increase in size when afterburning. Vectoring has required deflection of nozzle divergent flaps, if not rotation of the entire nozzle assembly. Aperture shaping for afterbody integration further imposed the use of less structurally efficient two-dimensional, rather than axisymmetric, nozzles. These capabilities required greater mechanical complexity in the system, as illustrated by the F-15 Short Take-Off and Landing Maneuver nozzle and the F-22 nozzle, both of which are significantly (~50%) heavier than the less capable nozzles of current tactical aircraft. Simply stated, there is a technical need to obtain jet control (thrust vectoring and afterburning) within the confines of a mechanically simple nozzle that retains as much fixed structure as possible. Such simplicity reduces parts count, weight, and cost (Terrier, 1995). The objective of this simplified concept is to combine the functionality of an F-22-class nozzle with the integration benefits of a fully fixed nozzle by fluidically controlling the aerodynamic flow of the jet.

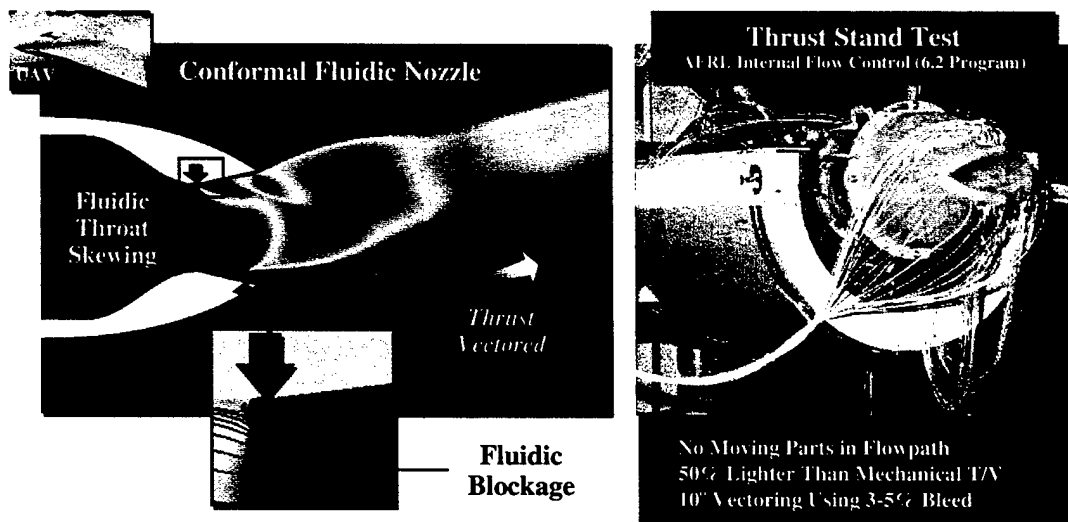


**Figure 1: Steady Injection Schemes in Development for Jet Control in Structurally Fixed Nozzle Systems**

Fluidic injection technology is being developed to provide virtual internal flowpath shape variation for achieving jet throat area and thrust vector control in

structurally fixed nozzles (Figure 1). Results of previous work have shown that the injection of a flow into the exhaust stream of a nozzle can produce a stable fluidic blockage or obstruction (Miller et al., 1995, 1997, 1999; Yagle et al., 2000). By metering injector flow, the size of this obstruction, and hence, the virtual internal flowpath shape can be actively modified to control both jet area and thrust vector angle without requiring movement of flowpath surfaces. However, steady injection techniques require injected air, typically bled from the engine. This tends to lower the performance of the weapon system. Research is required into new injection techniques, which increase the apparent blockage produced by a given amount of injected flow.

## **1.2 Research Objectives**

The overall objective of this research effort was to investigate basic, unsteady injection techniques, which could be exploited for enhancing fluidic nozzle control. Fluidic jet control techniques rely on the use of an injected flow to create a fluidic obstruction in the presence of the jet crossflow (see Previous Work, Section 1.4). If greater blockage can be obtained by pulsed injection, the mass flow required for nozzle jet control can be reduced. Reducing injector flow is desired to achieve the peak system performance. Specific objectives in the project are to:

- **Develop a Computational Fluid Dynamics (CFD) Simulation Methodology for Pulsed Injection**

Simulations are required to provide detailed understanding of a 3-D, unsteady flow field.

- **Explore Basic Schemes Using Pulsed Injection to Increase Fluidic Blockage**

General relationships between injector-jet structure, penetration, entrainment and blockage are sought for pulsed injection techniques.

- **Identify Fundamental Issues for Pulsed-Injection for Higher-Speed Flow**

Basic issues need to be explored with simulations of pulsed injection into a compressible flow and compared with the characteristics of an available pulsing actuator for injection.

- **Develop a Rapid Analysis Method**

An efficient CFD modeling method for pulsed injection is desired for design studies.

## **1.3 Research Approach Overview**

This research effort investigated two unsteady injection techniques for increasing the fluidic blockage produced by an injector. The first technique, denoted *pulsed injection*, addressed the periodic modulation of an injector stream into a crossflow to increase stream penetration, diameter, and blockage relative to steady injection. The second technique, denoted *pulsed ejection*, exploited the nature of a periodically modulated primary stream for increasing the entrainment of a co-annular secondary flow.

In principal, the high-pressure primary air would be bled from the engine compressor, and the lower-pressure secondary air would be bled from the engine fan. The combined stream would feed the control injector to provide greater mass flow and, therefore, blockage without requiring additional compressor air. To address the project objectives, this research effort was organized into five basic tasks. A summary of these tasks is described below and illustrated in Figure 2.

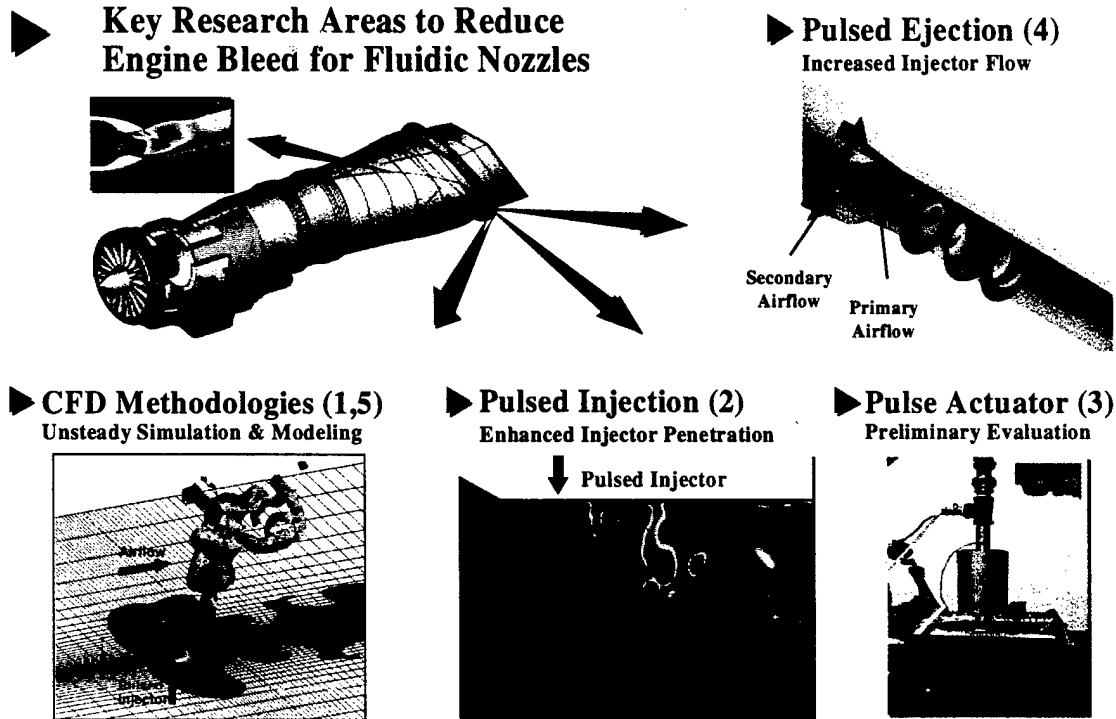


**Figure 2: Project Overview: Investigation of Unsteady Injection Techniques for Increasing Fluidic Control-Jet Blockage**

### (1) CFD Simulation: Methodology

A systematic study of CFD simulations for pulsed and steady injection into a crossflow was completed. The resulting methodology showed the effects of grid resolution, turbulence model, and numerical discretization on accuracy with comparison to test data. This task is detailed in Section 2.0.

### (2) Pulsed Injection Investigation

The first basic scheme investigated in this project (denoted *pulsed injection*) involved the periodic modulation of an injector stream into a nozzle crossflow to increase stream penetration and blockage relative to steady injection. The 3-D simulation methodology described above was used to explore the effects of injector pulsing frequency, Mach number and geometry on injector-jet trajectory, penetration, diameter, and blockage. This task is detailed in Section 3.0.

### (3) Pulse Actuator Evaluation

An investigation of pulsed injection actuators was conducted at the University of Tennessee Space Institute (UTSI). In this task, two actuators were evaluated for injector-jet penetration and blockage in a compressible, confined crossflow. The airflow of an injector issuing into a 2-D nozzle was visualized through a side-view window. Measurements were taken of static and unsteady pressure, mass flow rate, and injector jet velocity. This task is detailed in Section 4.0.

#### **(4) Pulsed Ejection Investigation**

The second basic scheme (denoted *pulsed ejection*) used a pulsed high-pressure primary stream to boost the entrainment of a co-annular, secondary flow. Such a device could be used to increase mass flow and, therefore, blockage of an injected stream without requiring additional high-pressure primary flow (e.g. compressor bleed air). Sources for the secondary stream include ambient or engine fan air. CFD simulations were used to investigate the effects of the following governing parameters on ejector pumping efficiency: primary-jet pulsing frequency, primary/secondary area ratio, and ejector mixing tube length. This task is detailed in Section 5.0.

#### **(5) Simplified CFD Model**

Many solutions will be required to optimize parameter settings, when evaluating injection techniques for flow control in a design environment. Simulation of pulsed injection is computationally intensive and for applications with multiple injectors, large grids will be required for adequate resolution. For such cases, simulation is too costly. A simplified CFD model was developed for the case of Pulsed Ejection that sought to capture the essential effect of the unsteady injected stream on the secondary flow, without the need of a highly resolved simulation. This task is detailed in Section 6.0.

### **1.4 Previous Work**

#### **1.4.1 Steady Injection in Crossflow**

Use of steady injection introduced at near normal angles into a confined crossflow has been the topic of many research studies (Broadwell et al., 1984; Fric et al., 1989; Gruber, 1995; Papamaschou et al., 1986). These studies characterize the interaction of the two streams by the subsequent entrainment, mixing, and penetration of the injector flow (secondary) into the crossflow (primary). For the context of this investigation, we have limited this summary to studies where a steady-state injector is used to fluidically control the jet of a nozzle.

#### **1.4.2 Fluidic Jet Control**

Foundational work on using fluidic injection to control exhaust system effective throat area was conducted in the late 1950s and early 1960s (Blaszak et al., 1960; Gunter et al., 1961; McAulay, 1959). Historic literature provides useful physical insight into the use of a steady-state injector jet to control nozzle throat area by producing a fluidic obstruction or blockage. It addresses the basic effects of internal nozzle contour, flow conditions, injector angle, and injector location on nozzle discharge coefficient. However,

the mass flow required to provide adequate throttling for application to afterburning turbofan engines was excessive. A more recent effort produced similar levels of performance (Federspiel, 1995). A thorough and current perspective of these efforts is found in several technical papers (Gridley et al., 1996, Yagle et al., 2000).

A summary of fluidic jet thrust vectoring concepts is found in a paper by Gridley et al. (1996). The concepts presented there include coanda surface blowing, counterflow, and shock-based thrust vector control.

The coanda surface blowing technique for thrust vector control was investigated by Chiarelli et al. (1993). This method achieved thrust vectoring if the wall-bounded jet adheres to a solid surface (the Coanda surface). For this concept, vectoring was achieved by moving Coanda flaps in the desired direction of jet turning. Secondary flow was introduced tangentially to the outward turned flap to prevent jet separation from the flap surface. This method achieved relatively low thrust-vector angles and required variable geometry (the Coanda flaps) for operation.

The "counterflow" thrust-vectoring method was investigated by Strykowski et al. (1994). This concept used a suction source to induce a secondary flow along one of the nozzle divergent flaps of a highly over-expanded nozzle. This "counterflow" vectored the primary jet by causing the jet to attach and, therefore, turn the jet toward the flap with secondary suction activated. Thrust vector angles of  $16^\circ$  were reported at relatively low suction-mass-flow rates (Gridley et al., 1996). Unfortunately, this concept must contend with the thrust loss, weight penalty, and possible instability associated with a highly over-expanded nozzle, as well as finding a suitable suction source.

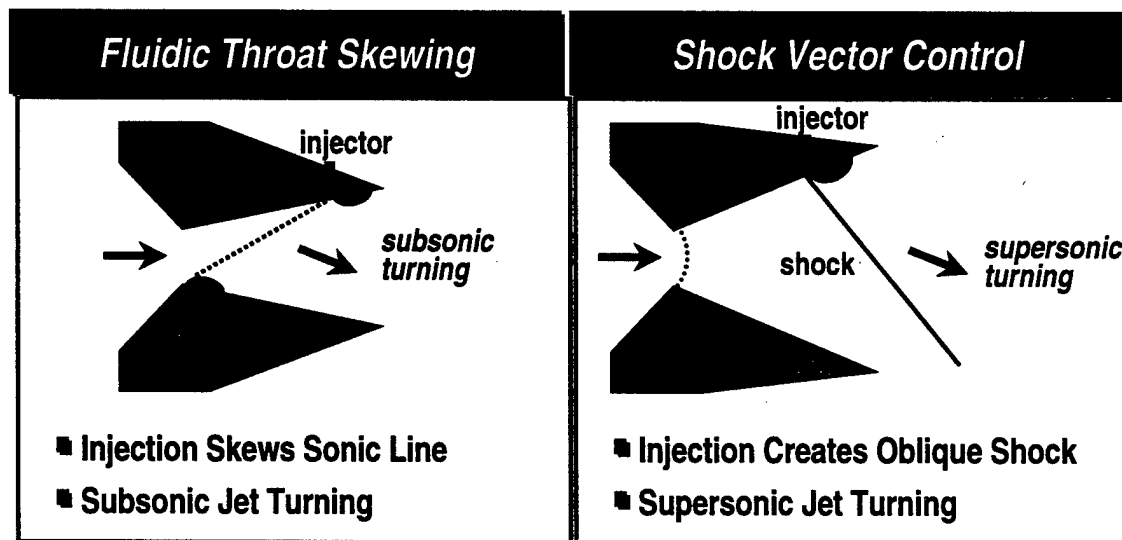


**Figure 3: Two Promising Techniques for Fixed Nozzle Vectoring Use a Steady Injected Stream to Produce a Fluidic Obstruction**

Historically, shock-based methods have been the most commonly investigated technique for fluidic thrust vector control (Gunter et al., 1961; Walker, 1997; Wing, 1994). Shock vector control methods use the formation of a strong oblique shock in the

divergent section of the nozzle to turn the primary jet. Introducing an injected flow into the supersonic primary nozzle flow produces a fluidic obstruction or blockage, as shown in Figure 3, generating the oblique shock (Wing, 1994).

The fluidic throat skewing method (Miller et al., 1999) incorporated previously developed methods for optimum jet area control (Catt et al., 1995; Miller et al., 1997) with additional features for thrust vectoring. The fluidic throat skewing technique features symmetric injection near the throat for jet area control and asymmetric injection to *subsonically* skew the sonic plane for thrust vector control (Figure 3). Injection slots are located at the nozzle throat and flap (near exit) on both interior sides of the nozzle. Introducing an injected flow to product a local obstruction on one side at the nozzle throat station and the opposing side at the nozzle flap station, the sonic plane is inclined or skewed, which turns the jet flow subsonically. By controlling the distribution of the injected flow between the throat and flap, area control is maintained while vectoring the jet.

Both the shock vector control and fluidic throat skewing techniques rely on the mechanism of blockage produced by an injected stream into the primary nozzle crossflow. Previous research efforts have focused on optimizing nozzle and injector geometry to achieve greater blockage (and, therefore, more area or vector control) for a given amount of steady injected mass flow. Further research is required into methods to increase the blockage of the injected stream beyond that of a steady jet.

#### 1.4.3 Pulsed Injection into a Crossflow

Effects of periodic disturbances on the structure, mixing, entrainment, and penetration of injectors in crossflow have been published for low-speed flows. Many of these experimental studies revealed dramatic increases in injector penetration, over and above steady injection. The mechanism responsible for this enhancement is the proper formation, spacing, and strength of trains of vortex rings generated at the injector exit.

In water-tunnel investigations using a mechanical, high-speed valve, Vakili et al. (1990, 1991) and Eroglu et al. (1991) have independently measured a 100% increase in pulsed-injector penetration over and above a steady-injector. When the flow rate of the injector was periodically modulated, distinct vortex rings were created whose spacing and strength were dictated by pulsing frequency for a given jet and crossflow combination. By tuning the pulsing frequency for a given injector to crossflow velocity ratio, it was observed that vortex-ring spacing and strength could be set to maximize injector penetration. Intuitively, since the mean flow rate of the pulsed jet is maintained constant, momentum flux of each emitted pulse is greater than that of the steady jet. Therefore, the increased momentum flux associated with each ring drives the increase in penetration.

Vermeulen et al. (1986, 1988) have also measured increase in transverse pulsed-injector penetration of 92% over and above a steady injector in low-speed combustor testing using an acoustically-pulsed fuel injector. They noted that vortex rings doubled in size after exiting the injector. An increase in fluidic blockage induced by the pulsed injector was postulated by measuring as much as a 24% decrease in primary mass flow over and above a steady jet (1993, 1996). They attribute the increase in flow blockage to

05 February 2001

enhanced penetration and increased physical diameter of the vortex ring due to the pulsed injector. While this observation suggested the feasibility of pulsed-jet blockage enhancement, its discovery was only incidental and was not the intent of their research.

The effects of pulsing on increased penetration have been documented for pulsed injection into very low-speed external flows. However, there has been little assessment of this phenomenon and its potential relationship to blockage in a higher-speed regime relevant to an internal/confined nozzle crossflow. Low frequency pulsing tends to increase penetration, but will also increase spacing between vortex rings. Maximum blockage may occur at a frequency that is higher than that for maximum penetration. Much of the experimental work to date has been done at much lower Reynolds numbers than we require for detailed understanding in nozzle flow fields. Although trends may be correct at Reynolds numbers above 1000, new issues may arise in the subsequent mixing, entrainment, penetration, and blockage effects as small-scale turbulence becomes more pronounced.

#### 1.4.4 CFD-Based Simulation of Pulsed Injection

Little research had been published on Navier-Stokes simulation of pulsed injection at the time this project commenced. Simulation of pulsed injection presents several significant challenges. The effective blockage and penetration of vortical structures is highly dependent on viscous effects. Vortex methods have been developed for tracking pulsed jets in a crossflow (Vakili et al., 1991). Since vortex methods do not include viscous effects, their use for predicting blockage or penetration is limited. Steady injector jets in subsonic and supersonic crossflows have been simulated with Navier-Stokes solutions with two-equation turbulence models (Gerlinger, 1996). Kral et al. (1997) performed a two-dimensional, incompressible numerical simulation of a pulsed-jet actuator blowing into a quiescent flow using a Reynolds-Averaged Navier-Stokes (RANS) based turbulence model. Rizzetta et al. (1998) conducted a low speed, incompressible, direct numerical simulation of a synthetic-jet actuator blowing into a quiescent flow.

## **2.0 A Simulation Methodology for Pulsed Injection Into a Crossflow Using 3-D Unsteady CFD**

### **2.1 Introduction**

For the design of fluidic nozzle configurations using steady injection techniques, CFD has been an essential analysis tool. Likewise, CFD will be important in developing efficient fluidic nozzle control concepts using pulsed injection. However, analysis of unsteady flows is much more complex and demanding than steady flows in terms of required grid resolution, computational time and flow physics modeling. The purpose of this work is to evaluate these requirements by comparing CFD analysis to experimental data of an unsteady pulsed injector jet issuing into an internal crossflow (Vermeulen et al., 1990; Vermeulen and Ramesh, 1997).

The intended application of the CFD analysis is to provide adequate qualitative structure and quantitative data of the injector-jet flow field sufficient to investigate and exploit its potential for enhancing fluidic blockage of the crossflow. This will require appropriate selection of turbulence model, numerical resolution, and numerical scheme. To guide the appropriate selection of these CFD parameters, simulations of a pulsed-injection test apparatus were conducted and compared with corresponding experimental measurements. For quantitative assessment, CFD simulations of the pulsed-injection configuration tested by Vermeulen, Chin and Yu (1990) were performed. This experimental configuration consisted of a 19 mm-diameter injector jet issuing at 19 m/s into a 10 m/s crossflow. Data acquired in the test included time-averaged hot-film measurements of velocity and mass-flow measurements of the main and injected streams. Both steady and pulsed injector jets at several frequencies were measured. In this study, results for steady injection and pulsed injection at 208 Hz were used for comparison to analysis. The Lockheed Martin Aeronautics Company's CFD code FALCON was selected for the simulations of the experimental configuration.

### **2.2 Experimental Configuration and Measurements**

Vermeulen, Chin, and Yu (1990) investigated the mixing of both steady injector jets and acoustically excited pulsed injector jets injected normal to a confined crossflow. The effects of varying the injector jet to crossflow velocity ratio and injector-jet pulsation strength were studied. They were able to show that, by pulsing the injector jet, a significant increase in both injector-jet penetration and mixing were obtained with the same total mass flow as compared to the steady-injector case.

#### **2.2.1 Test Configuration**

The test configuration is shown in Figure 4 consists of a rectangular test section, 114 mm high, 343 mm wide, and 889 mm long. The orifice of the injector jet is centered on the lower surface of the test section and has a diameter  $D$  of 20.0 mm. The orifice of the injector jet has a lip that extends 4mm above the lower surface. The test section and

injector jet were fed by a 45-kW blower. Mass flow to the injector jet was varied by means of orifice resistance plates mounted in downstream of the branching of the main flow. The injector jet was pulsed using a 200W driver operating through a tube connected at right angles to the injector jet tube.

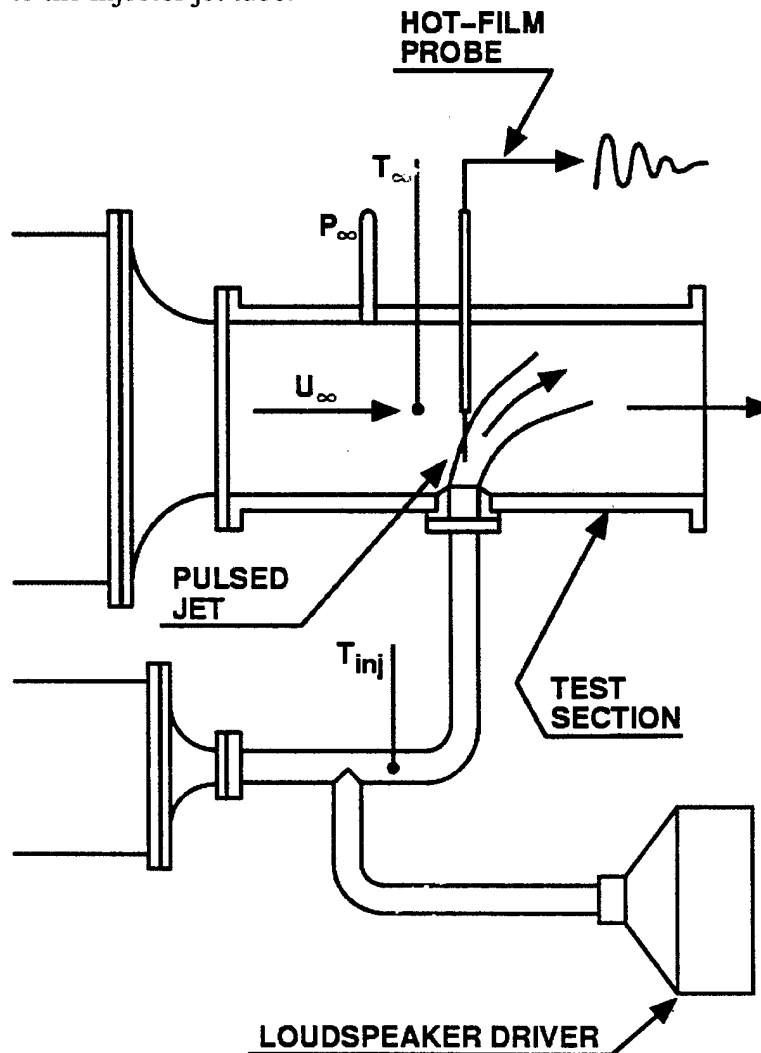


Figure 4: Schematic of Test Configuration.

### 2.2.2 Flow Conditions

For the present study, one case was selected for comparison to numerical results. The conditions for the selected case are:

$$U_\infty = 9.94 \text{ m/s}$$

$$U_{inj} = 19.0 \text{ m/s}$$

$$U_e / U_{inj} = 1.18$$

$$\omega = 208 \text{ Hz}$$

$$Re_{inj} = 20294$$

$$Re_\infty = 83567$$

### 2.2.3 Measurements

The primary set of measurements that were made in the experiment was done using a hot-film anemometer mounted on a vertically traversing mechanism along the centerline of the test section. This allows for time-averaged and RMS measurements of velocity magnitude. Velocity magnitude profiles were taken at centerline locations of  $X/D$  of 0.0, 1.43, 2.86, 5.72, and 11.44. The velocity profiles became mostly uniform at  $X/D$  of 5.72 and beyond, so comparisons with numerical results were restricted to the three upstream measurement locations. A complete description of the experimental procedures, calibration, and measurements, is contained in Vermeulen, Chin, and Yu (1990).

## **2.3 CFD Methodology**

Lockheed Martin Aeronautics Company's CFD code FALCON was used in the present study. The code uses a structured-grid, multi-block topology, with compressible finite volume discretization and the option of two turbulence models. The code uses implicit solvers and has a parallel solver capability. The code is used primarily for external and internal flows over military aircraft configurations. It is used extensively in the analysis of fighter inlet and nozzle configurations.

### 2.3.1 Discretization

FALCON uses the upwind flux difference splitting of Roe (1981) for the convective terms. This discretization uses second or third order MUSCL (van Leer, 1995) extrapolation of the fluxes with the option of flux limiting using the MINMOD (Roe, 1981) or SUPERBEE (Sweby, 1984) limiters.

For time accurate solutions, FALCON uses a second-order, three point backward difference of the time term. Viscous fluxes are discretized using second-order central differences.

### 2.3.2 Turbulence Models

FALCON has RANS and Large Eddy Simulation (LES) models. The primary RANS turbulence model is the  $k-kl$  two-equation model of Smith (1990). This model consists of transport equations for the turbulent kinetic energy,  $k$ , and the product of  $k$  and the turbulent length scale,  $kl$ . The turbulent transport equations are discretized in an analogous fashion to the Navier-Stokes equations using upwind flux difference splitting for the convective terms and central differences for the viscous and source terms. The LES model is based on the formulation of Smagorinski (1963). It has been extended to include compressibility effects.

### 2.3.3 Solvers

Two implicit solvers are available, a symmetric Gauss-Seidel (SGS) method and the Strongly Implicit Procedure (SIP) of Stone (1968). The SGS method is used when computer memory constraints are a consideration and the SIP method is used for fastest

convergence. For unsteady solutions, a dual time stepping approach is used where the solution is iterated at each time step to convergence using one of the solvers. The implicit solvers allow for rapid convergence of the solution at each time step. This approach removes CFL restrictions resulting from fine grid spacing near no-slip walls. As a result, fewer iterations are required in the unsteady solution.

Both solvers can operate in parallel. Parallelization is achieved by partitioning the grid into blocks and running each on a separate processor. Updates of the flow solution at block interfaces are done explicitly. Transfer of interface information between processes is accomplished using either the Parallel Virtual Machine (PVM) or Message Passage Interface (MPI) message passing libraries.

## **2.4 Results and Discussion**

A series of runs for the conditions described above were simulated using FALCON. Four studies are described here. Two grid-resolution studies, one for a steady-injector jet using a two-equation turbulence model, the other for a pulsed-injector jet using the LES model, were done to characterize the differences in grid resolution requirements between steady and pulsed-injector jets. A third study examines the applicability of two-equation vs. LES turbulence models for the pulsed-injector jet simulations. The fourth study examines the effect of numerical discretization on the pulsed-injector jet simulations. For each of these studies, time-averaged velocity profiles were computed from the CFD solution at locations of 0.0, 1.43, 2.86 injector jet diameters downstream of the injector jet centerline. These results are presented below with comparison to experimental data.

### **2.4.1 Grid and Boundary Conditions**

Three grids were used in these tests, a coarse resolution grid of 65,772 cells, a medium resolution grid of 382,800 cells, and a fine resolution grid of 630,952 cells. All grids were subdivided into multiple blocks to allow for parallel computation. The grids were constructed such that approximately uniform resolution in all directions was obtained in the flow region of interest. Figure 5 shows the fine grid distribution along the symmetry plane and the lower surface of the test section. Figure 6 shows a close-up of the injector-jet orifice area.

Characteristic subsonic inflow and outflow boundary conditions are specified at the inlet and exit of the computational domain. A no-slip condition is specified on the lower surface. In order to conserve computational resources, slip-wall boundary conditions with relatively coarse spacing were applied on the upper surface and sidewall of the test section. Flow symmetry was specified along the symmetry plane of the test section. There is some question as to the validity of this boundary condition as the vortex rings in the pulsed-injector jet will most likely undergo an asymmetric break down at some point in the flow. Computational resource limitations have precluded the use of a full-symmetry grid to model asymmetric effects.

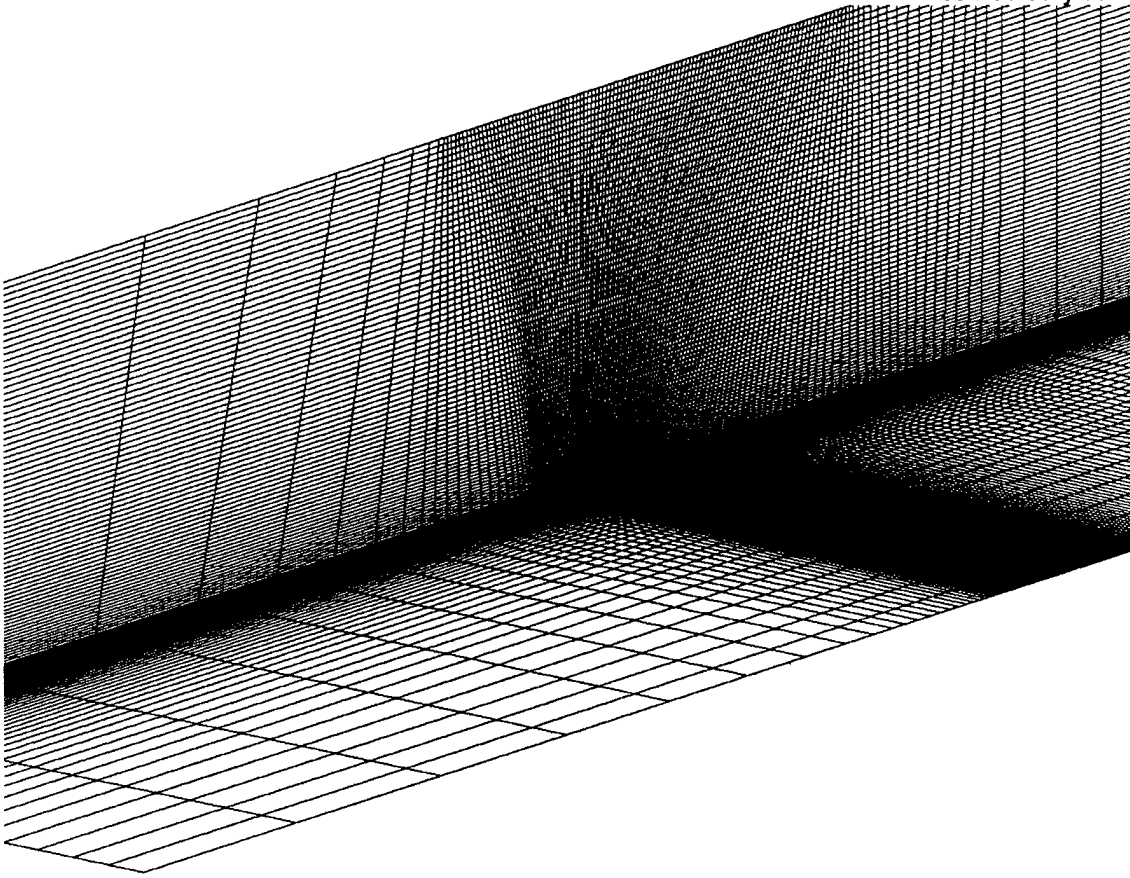


**Figure 5: Fine Grid. Injector Jet Orifice Location is Marked in Red.**

The pulsed-injector-jet boundary condition of Kral et al. (1997) was applied at the injector jet orifice. The velocity as a function of time was specified and a one-dimensional approximation of the incompressible momentum equation was used to determine the pressure gradient. The actual waveform as measured in the experiment was nearly sinusoidal. The waveform specified in the computation is specified by the equation

$$U(t) = U_{inj} + U_e \sin(2\pi\omega t)$$

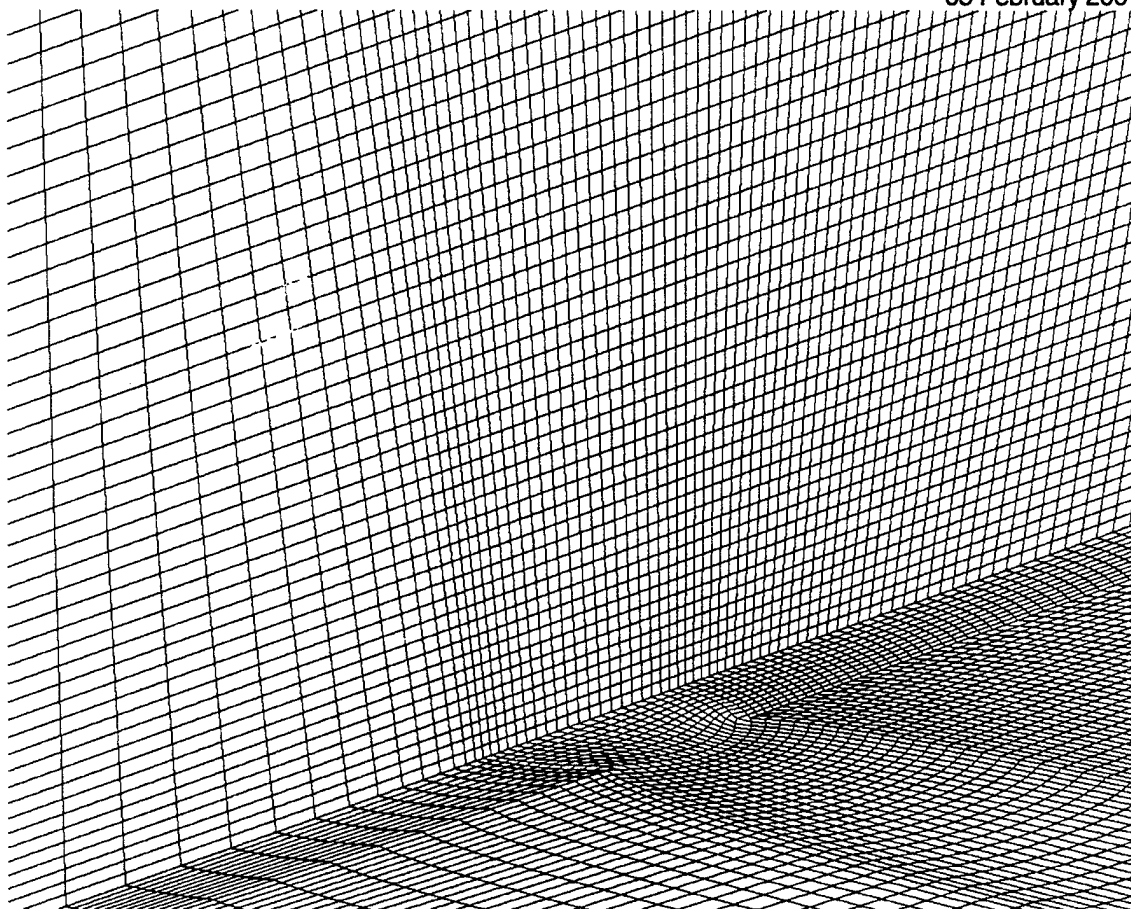


**Figure 6: Close-up of Fine Grid. Injector Jet Orifice Location is Marked in Red.**

#### 2.4.2 Temporal Resolution

A time step of  $1.2 \times 10^{-5}$  seconds has been used for all runs in this study. For a 208 Hz pulsing frequency this gives 400 time steps per pulsing cycle. An initial solution was computed over a large number of cycles to determine the number of cycles required to obtain a statistically stationary solution. Time-averaged velocity profiles were computed over varying number of cycles. The results showed that eight cycles were required to achieve statistical convergence. In addition, the first two or three cycles are not included in the time averaging computations in order to avoid transient effects.

#### 2.4.3 Velocity Scaling

The Mach number of the main flow in the experiment is 0.03. FALCON is a compressible flow solver, and can generate excessive numerical diffusion when run at very low Mach numbers, due to the nature of the upwind discretization of the convective terms. Tests were run on the medium grid to characterize the effects of the reference Mach number. These tests showed that if the velocities in the computation were re-scaled to produce a main-flow Mach number of 0.1, numerical diffusion was reduced to acceptable levels and no unwanted compressibility effects were detected. All runs reported here have been run with velocities scaled to Mach 0.1.

It should be noted that the use of the results of this work are intended to be applied to pulsed-injector jets in a moderate subsonic or transonic compressible flow. The issues of low speed numerical diffusion are only important here because the experimental data are incompressible.

#### 2.4.4 Numerical Simulation of Hot-Film Anemometer

Experimental measurements were made at the centerline of the test section using a single-wire hot-film anemometer. This probe senses the magnitude of two components of the velocity normal to the wire. In the experiment, the measurements were averaged in time to get an average velocity magnitude as a function of height at various locations along the centerline of the test section downstream of the injector jet.

To simulate hot-wire measurements in the CFD solutions, the axial and vertical components of the computed instantaneous velocities of the nearest computational cells were interpolated to the measurement location. The magnitude of the interpolated instantaneous velocities was taken. The interpolated instantaneous velocity magnitude was then numerically integrated in time to obtain average two-component velocity magnitudes. Profiles of the computed time-averaged velocity magnitude profiles were then plotted against the experimental values and are given below.

#### 2.4.5 Effect of Grid Resolution - Steady Injector jet

Solutions were obtained for both steady and pulsed-injector jets on grids of varying resolutions to determine grid requirements to adequately resolve the flow. The steady-injector jet case was run with FALCON's two-equation turbulence model and a steady solution was obtained.

The steady-injector jet was run on the coarse and medium grids. The velocity magnitude profiles are compared along with experimental data in Figure 7.

The coarse and medium grid results agree well with each other, suggesting the grid resolution is adequate for steady-injector jets. However, both solutions overpredict the penetration of the injector jet when compared to experimental data. This is likely because the two-equation model does not account for strong flow curvature in the injector jet.

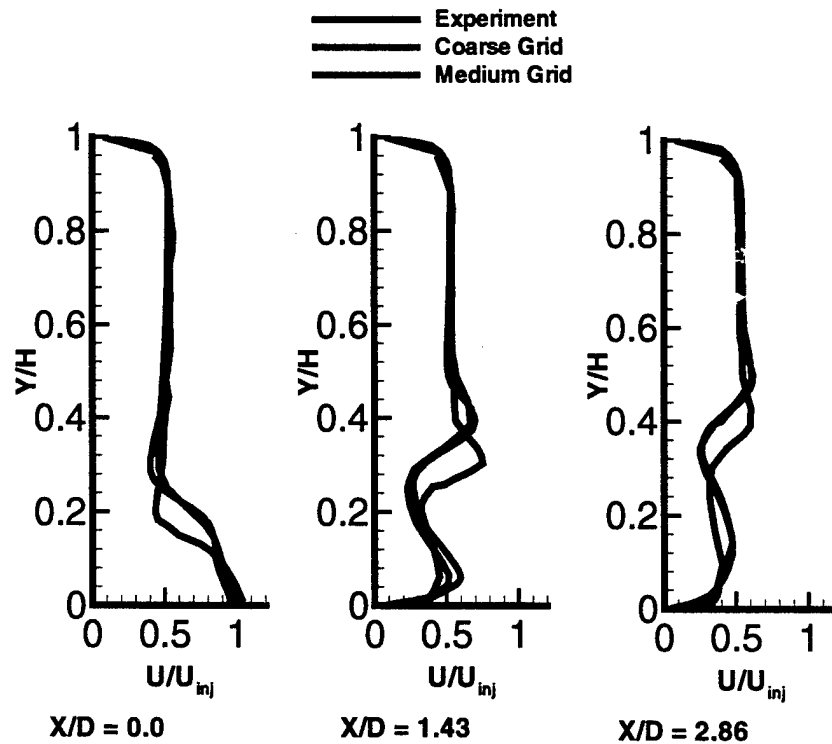


**Figure 7: Effect of Grid Resolution on Velocity Magnitude Profiles for the Steady Injector Jet**

#### 2.4.6 Effect of Grid Resolution - Pulsed Injector jet

The pulsed-injector jet solutions were run on the coarse, medium, and fine grids. The coarse and medium grids were identical to those run for the steady-injector jet solutions. All solutions for the grid-resolution study were run using the LES turbulence model, and second-order discretization.

An instantaneous three-dimensional view of the vortex ring structure of the pulsed-injector jet is shown in Figure 8. This visualization is obtained by plotting surfaces of constant vorticity magnitude. Two vortex rings are evident, one emanating from the injector-jet orifice and a second above it. This figure shows the evolution of the rings as they interact with the crossflow. The ring diameter grows substantially, and the ring structure deforms as it moves away from the injector-jet orifice.

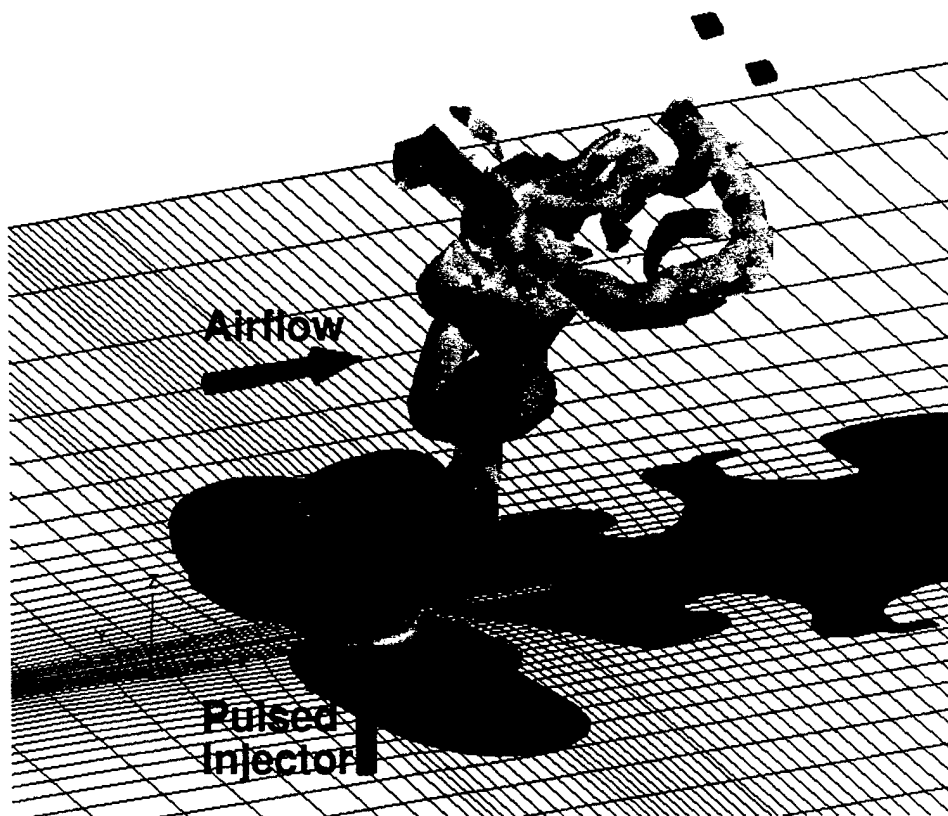


**Figure 8: Three-Dimensional View of Ring Structure as Surfaces of Constant Vorticity Magnitude**

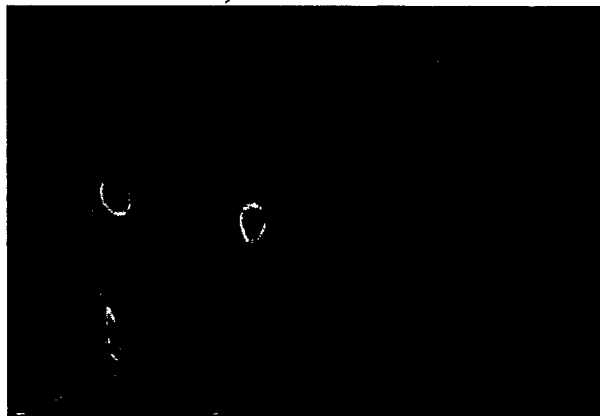
Instantaneous vorticity-magnitude contours on the test section centerline are given in Figure 9 for the three different grid resolutions. Mean velocity profiles for the three grids and for the experiment are shown Figure 10.

The effect of grid resolution is clearly shown in these figures. While the coarse grid solution produced good results for the steady-injector jet, it was totally inadequate for resolving the structure of the pulsed-injector jet. The time averaging of the flow field by the RANS models in the steady case has the effect of smoothing spatial gradients, thereby reducing requirements for spatial grid resolution.

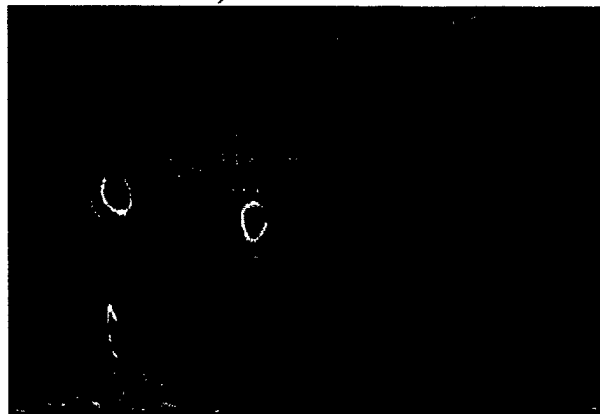
The medium and fine grid results agree very well with each other for the pulsed-injector jet, with excellent agreement at  $X/D$  of 0.0 and 1.43. The solutions are in reasonable agreement with experiment, although they tend to underpredict injector-jet penetration.



a) Coarse Grid



b) Medium Grid



c) Fine Grid

**Figure 9: Effect of Grid Resolution on Vorticity Magnitude for Pulsed Injection**

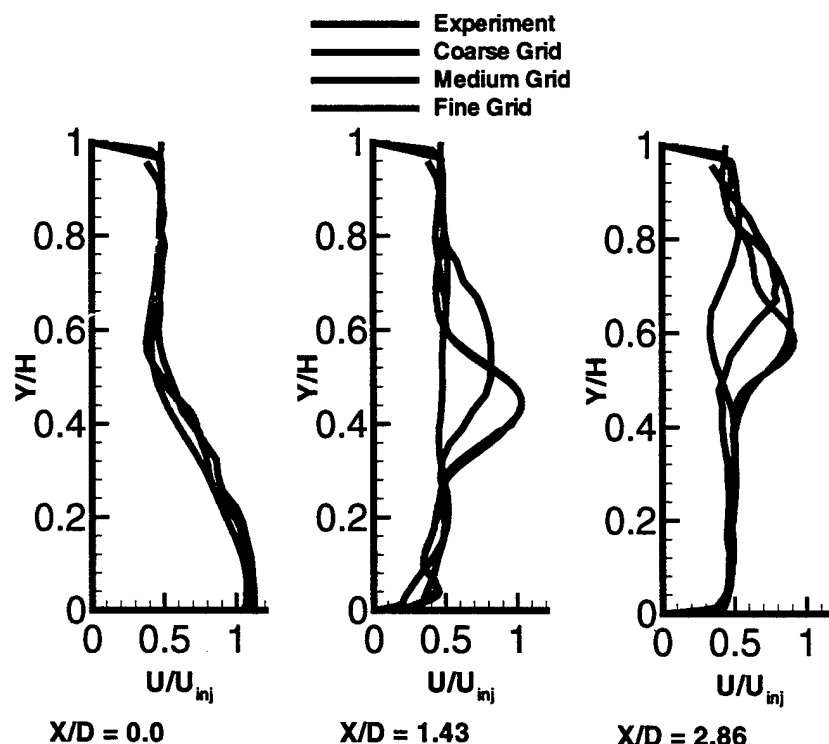


**Figure 10: Effect of Grid Resolution on Velocity Magnitude Profiles for the Pulsed Injector Jet, using LES model and Second Order Accuracy**

#### 2.4.7 Effect of Turbulence Modeling

RANS turbulence models such as the  $k-k_l$  model are derived by time averaging the unsteady Navier-Stokes equations. While valid for steady flows, they are only valid for unsteady flows if the time scales of interest are much larger than the turbulent time scales of the flow that are being modeled. LES models, on the other hand, only model the turbulent scales that cannot be resolved by the computational mesh and are inherently unsteady. The purpose of this test is to determine the applicability of these models to the pulsed-injector jet simulations under consideration here.

Three simulations were run for this test. The first uses the  $k-k_l$  model, the second used the Smagorinski LES model, and the third was run LES with no turbulence model. The LES no-model run includes molecular viscosity and no slip walls. The numerical diffusion in the flow solver acts as a sub-grid scale model (Okong'o and Knight, 1998). All cases were run with the fine grid using second order discretization. Figure 11 shows the velocity profiles of the three cases compared with experiment. While good agreement is shown at  $X/D = 0.0$ , the profiles generated by the  $k-k_l$  model at the other two locations were considerably more diffused than the other two cases, and differ considerably from experiment. This indicated that the model is not applicable for simulating this class of flow field. The other two cases have reasonable agreement with experiment, although the location of the peak in the velocity profile is lower than that of the experiment.

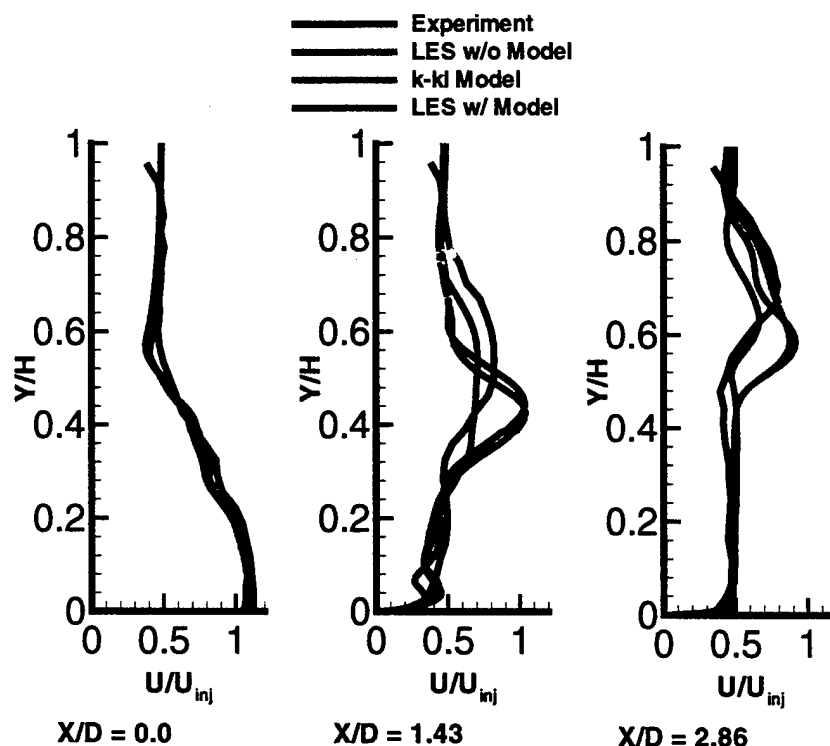


**Figure 11: Effect of Turbulence Model on Velocity Magnitude Profiles. Simulation used Fine Grid and Second Order Accuracy**

The LES solutions with the Smagorinski model and with no model are in close agreement. This implies that the magnitude of the numerical diffusion is comparable to or larger than the subgrid scale stresses in the LES model. In the laminar solution, the numerical diffusion acts as an LES model.

#### 2.4.8 Effect of Numerical Discretization

FALCON typically uses 2<sup>nd</sup> or 3<sup>rd</sup> order upwind discretization of the inviscid fluxes. In compressible flows, in order to avoid spurious oscillations at flow discontinuities such as shocks or contact surfaces the accuracy of the discretization must be reduced to first order. This is accomplished using a flux limiter. One of the most common is the MINMOD limiter (Roe, 1981). One disadvantage of this limiter is that it reduces the order of accuracy of the discretization to one at a flow extremum, even if the solution at the extremum is smooth and higher order accuracy is desired. This problem is partially alleviated in FALCON by using the SUPERBEE limiter with a compression factor. The compression factor,  $c$ , is a user-defined parameter that can be set from 1.0 to 2.0. Setting  $c = 1.0$  is equivalent to the MINMOD limiter, while  $c = 2.0$  gives the full SUPERBEE limiter. The authors experience has shown that  $c = 1.2$  gives the best compromise between accuracy and stability.

The pulsed-injector jet simulations obviously have a large number of extrema in the flow field; therefore, accuracy of the discretization with flux limiters is of particular

concern. The present flow simulations were incompressible and as such did not require flux limiting. However, the intent is to extend the results of this study to compressible flows, so the effect of flux limiters cannot be ignored.

In order to test the effect of the limiters on the accuracy of the pulsed-injector jet simulations, three cases were run. For first case  $c$  was set to one, i.e. the MINMOD limiter was used. The second was run with  $c = 1.2$ . A third case was run unlimited for comparison. All of these cases were run with the fine grid and the LES model. The velocity profiles for these runs are given in Figure 12.

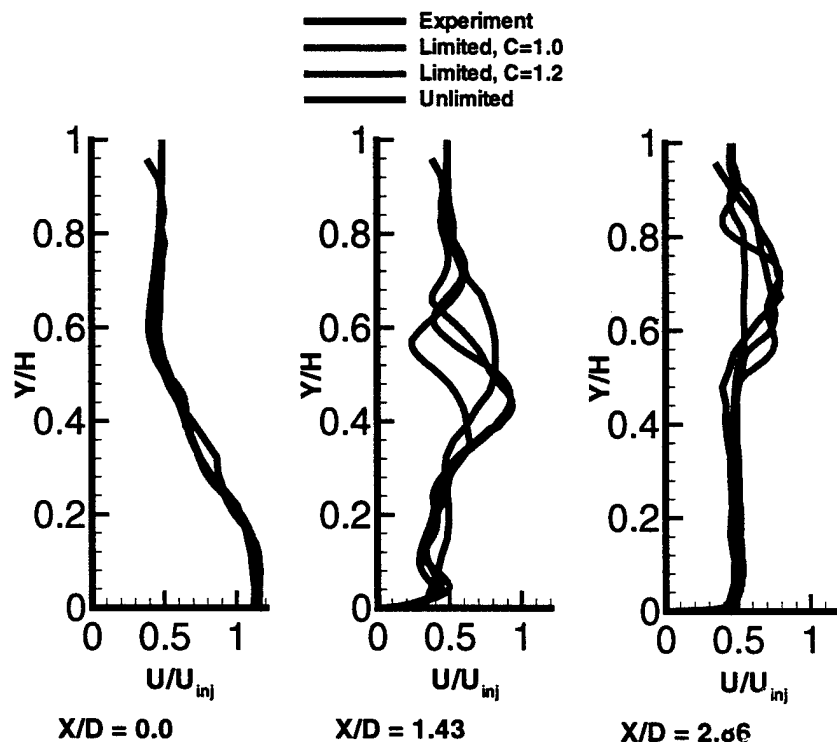


**Figure 12: Effect of Flux Limiters on Velocity Magnitude Profiles. Simulations used Fine Grid, LES Model, and Second Order Accuracy**

As can be seen in the figure, the profiles for  $c = 1.0$  case are severely diffused at  $X/D$  of 1.43 and 2.86. The agreement between the  $c = 1.2$  and the unlimited cases is much better, although there are differences at the upper part of the profile at  $X/D = 2.86$ . Comparison of the last two cases with experiment is reasonable, although the simulations show a double peaked profile at  $X/D = 1.43$  while the experiment shows a fuller single peak.

An additional test of the numerical discretization examined the effects of the order of accuracy on the pulsed-injector jet simulations. Two cases were run, one using second order discretization, and the other using third order. Both cases were run using the fine grid, the LES turbulence model, and no flux limiter. As can be seen in Figure 13, the third order result matched the penetration height of the experimental data better than the

second order result at  $X/D = 1.43$ . The double peaked profile was still evident in the simulation.

This double-peaked profile is caused by the passage of a coherent vortex ring past the  $X/D$  location of the profile. As the vortex ring moves rearward, it is also moving upward. The rear of the vortex ring passes the profile location where the lower peak occurs, while the front of the ring causes the upper peak of the profile. If the vortex rings in the experiment were undergoing asymmetric (and non-periodic) distortion as they moved downstream, the time-averaged velocity profiles would not show this double peaked behavior. Since the current simulations have been run by imposing symmetry at the test section centerline to reduce computational requirements, any tendency toward asymmetric distortion would be suppressed in the simulations.

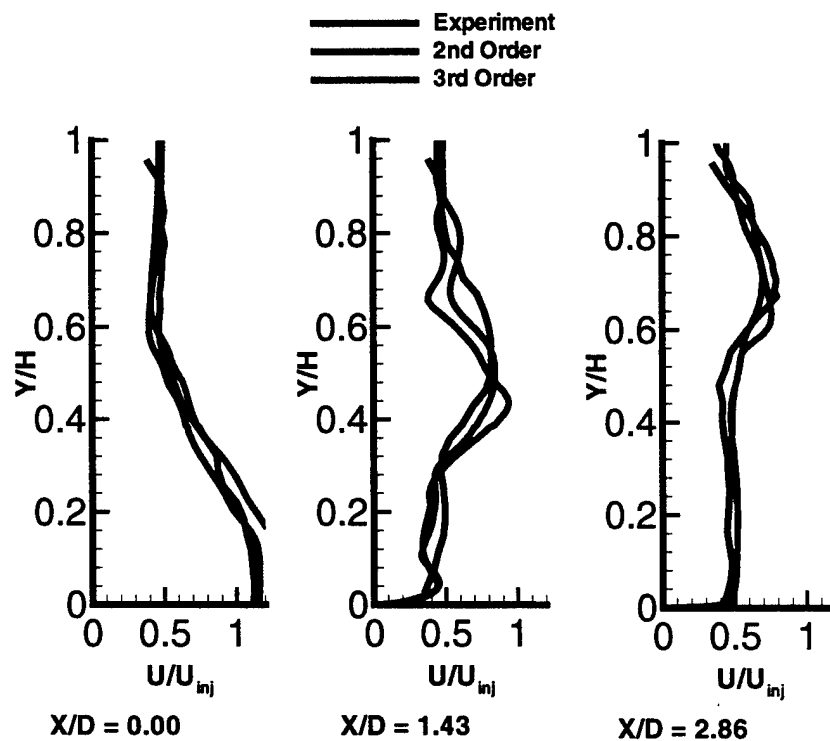


**Figure 13: Effect of Order of Accuracy on Velocity Magnitude Profiles. Simulations used Fine Grid, LES Model, with no Flux Limiter**

In the last case presented here, both simulations were run using a slightly higher mass flow for the injector jet than the other cases. The original injector-jet profile at the orifice was assumed to be a symmetric, fully turbulent profile with a peak-average centerline velocity of  $U_{inj}$ . One of the researchers (Vermeulen) suggested that the injector-jet profile may not have been symmetric due to a bend in the pipe geometry upstream of the orifice. In addition,  $U_{inj}$  may not have been the peak velocity in the profile thus resulting in a reduced injector-jet mass flow in the original simulations vs. the experiment. To address this issue, the profile in these last runs was based on mass flow measurements of the injector-jet flow, and not on  $U_{inj}$ .

## **2.5 Task Summary**

A systematic study comparing unsteady CFD analysis to experimental data has been performed to determine parametric requirements to accurately simulate pulsed-injector jets injecting into a crossflow. The effects of grid resolution, turbulence modeling, and numerical discretization were examined.

Considerably better grid resolution was required for pulsed-injector jet simulations as compared to a steady-injector jet of the same mass flow. The time averaging of the two-equation model in the steady-injector jet simulation smoothes spatial gradients, reducing resolution requirements.

The RANS-based turbulence models were not adequate for pulsed-injector jet simulations, however, since the same time-averaging process removes relevant features of the unsteady flow. LES simulations with and without the Smagorinski model produced very similar results.

The accuracy of the pulsed-injector jet simulations was very sensitive to treatment of the upwind discretization. In particular, the selection of a flux-limiting method for the upwind discretization is important. Investigation of better flux limiters and higher-order methods applicable to compressible flows is needed. The use of third-order discretization of the convective fluxes improved the prediction of injector-jet penetration height over second-order discretization.

### 3.0 A Computational Investigation of Pulsed Injection Into a Confined, Expanding Crossflow

#### 3.1 High-Speed Simulations

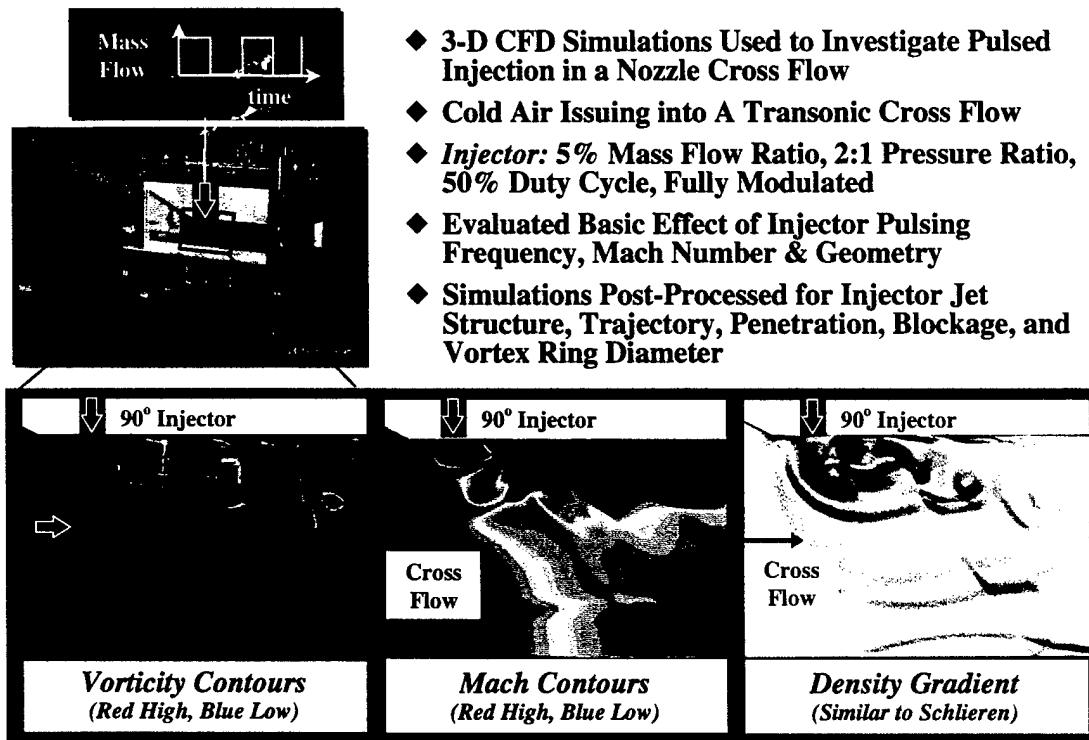


Figure 14: CFD Simulation Used to Investigate Basic Pulsing Scheme on Injector Jet in Crossflow

The first basic scheme investigated in this project (denoted *pulsed injection*) involved the periodic modulation of an injector stream into a confined, expanding, compressible crossflow. The objective of this task was to determine if pulsing could be used to increase injector-jet stream penetration and blockage relative to steady injection at flow field speeds relevant to an advanced turbofan nozzle. A 3-D unsteady CFD simulation methodology was used to generate solutions for this investigation (see Section 2.0 for details on the methodology). An overview of the approach used in this investigation is illustrated in Figure 14. Simulations were run with cold air issuing from transverse or angled injectors into a transonic nozzle crossflow. Simulations were run with either nine or 28 injectors distributed across the span of the nozzle. Geometric details of the nozzle geometry used in these simulations are provided in Sections 4.0 and 11.5. A characteristic-theory based total-pressure/total-temperature boundary condition was used to model the primary-nozzle inflow stream. This boundary condition was located two characteristic nozzle heights upstream of the injector exit. A static-pressure-based outflow boundary condition was applied at the nozzle exit. The nozzle-entrance total pressure to exit station static pressure ratio was held at 2.0. The nozzle walls were

modeled as no-slip and adiabatic. Time-accurate solutions were run using a fine resolution grid, a second or third-order upwind discretization scheme, and an LES turbulence model. To evaluate the effect of pulsing relative to non-pulsing, steady injection cases were also run using a RANS-based turbulence model. Since injector mass flow rate has been found to be the primary governing parameter of its effective blockage on the nozzle crossflow (Federspiel, 1995; Miller et al, 1995, 1997), the time-averaged injector-to-nozzle mass flow ratio ( $\bar{W}_{inj}/W_p$ ) was held at 0.05. Therefore, any benefits to injector-jet penetration and blockage observed from pulsing would not be gained by increasing total mass flowrate. A boundary condition was applied at the injector orifice exit to effectively specify a square pulsed-jet waveform as a function of time. The injector was fully modulated between a specified peak Mach number and zero-flow conditions using a 50% duty cycle. Injector-exit static temperature was held constant, while static pressure was set to achieve the desired mass flow rate.

Multiple solutions were run to evaluate the effects of varying injector-jet pulsing conditions and geometry on the injector jet stream and its interaction with the nozzle crossflow. A procedure was developed to post-process computational flow-field images stored from the time-accurate CFD solutions to evaluate the resulting injector-jet structure, trajectory, penetration, diameter, entrainment, and blockage. Images of vorticity-magnitude contours were found to be most effective for viewing the train of vortex structures generated by the pulsed injector. To observe injector-jet entrainment, particles were computationally released into the crossflow and superimposed on the vorticity contours. Images of Mach-number contours were used to reveal the sonic line and associated shock structures generated by the pulsed injector. Images of black-and-white density-gradient contours were also generated for potential future comparison to experimental schlieren imaging measurements.

### 3.2 Effects of Injector-Jet Pulsing Frequency

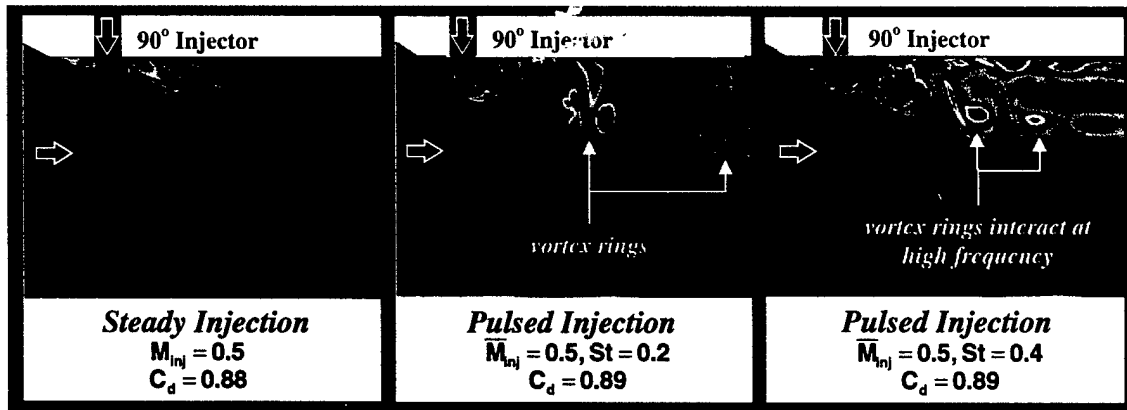


**Figure 15: Effect of Pulsing Frequency on Injector-Jet Structure, Penetration, and Blockage (Vorticity Contours: Red-High, Blue-Low)**

The effect of pulsing frequency ( $f$ ) or Strouhal No. ( $St = f \cdot D_{inj} / V$ ) on injector-jet structure, trajectory, penetration, and diameter is illustrated in Figures 15, 16 and 17. Figure 15 contains a comparison of vorticity contour images taken from a steady-injection

solution with an injector Mach number of 1.0 and pulsed injection simulations with a time-averaged injector Mach number ( $\bar{M}_{inj}$ ) of 0.5. Figure 16 contains measurements of injector-jet trajectory and penetration in the near-field region of the injector exit with varying pulsing frequency and Mach number. Points along the trajectory were measured from the center of the injector exit to the approximate center of the path taken by the vortex rings. Figure 17 contains measurements of the vortex-ring diameter along the injector-jet trajectory.

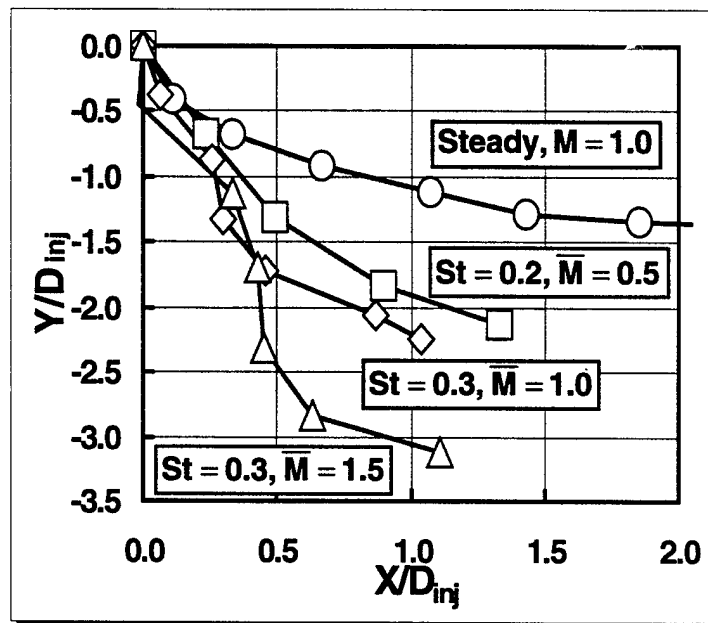


Figure 16: Effect of Pulsing Frequency and Mach Number on Injector-Jet Penetration Relative to Steady Injection

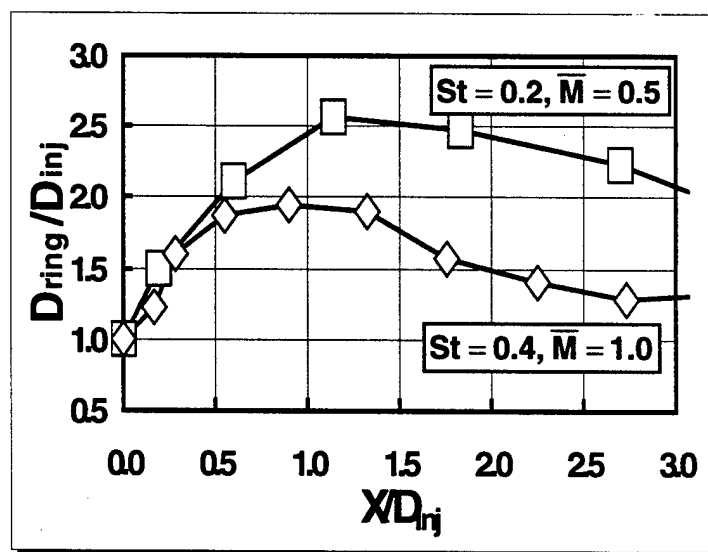


Figure 17: Effect of Jet Frequency on Injector-Jet Diameter

The shear layer defined by the injected stream and its associated penetration into the nozzle crossflow can be seen in the steady injection solution (Figure 15). In the pulsing simulations, a series of vortex rings were seen emerging from the injector exit. As these rings were convected downstream, they became stretched and distorted while beginning to break down rapidly because of the turbulent interaction with the nozzle crossflow. The pulsing frequency appeared to determine the spacing between subsequent vortex rings. Pulsing generally produced a measured increase in injector-jet stream penetration and diameter over that of a steady injector. Injector penetration was a function of pulsing frequency. Gains of approximately 50-100% in penetration were measured relative to the steady case at the same time-averaged mass flow rate and momentum flux. Peak penetration was achieved with a  $St$  of 0.3. The basic mechanism governing this enhanced penetration is believed to be the appropriate formation, spacing, and strength of the vortex rings generated at the injector exit. At the frequency for peak penetration, the rings penetrated deeper into the crossflow, in part, because each ring traveled in the wake region of the neighboring downstream ring. Higher frequency pulsing ( $St > 0.4$ ) produced very close vortex ring spacing, which evidently causes the rings to adversely interact with one another, decreasing penetration. This close ring-ring interaction was characterized by the merging of adjacent rings. Previous work established the effect of pulsing on injector jet penetration into an *incompressible* flow (Eroglu et al., 1991; Vakili et al., 1999; Vermeulen et al., 1996).

The vortex-ring diameter generally increased (relative to the exit diameter) in the near field region ( $< 1 \cdot D_{inj}$ ), as a likely result of the rapid entrainment associated with the regions of high vorticity and shear near the rings. The vortex-ring shape and diameter was a strong function of pulsing frequency. While injector-jet structure, penetration and diameter were strong functions of frequency, the injector-jet blockage was relatively unaffected by pulsing frequency (see Figure 15). The injector-jet blockage was measured by the time-averaged primary-nozzle discharge coefficient ( $C_d = W/W_{ideal}$ ). More discussion on blockage will follow below.

### 3.3 Effects of Injector-Jet Pulsing Mach Number

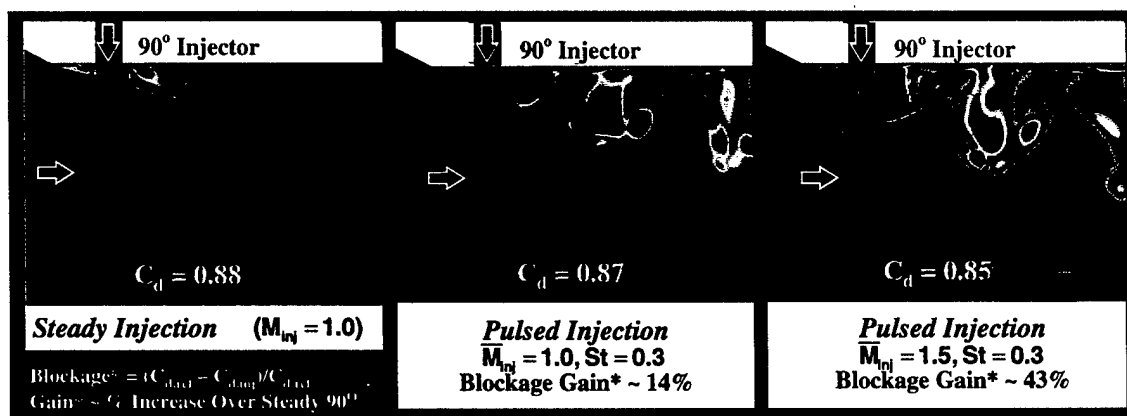
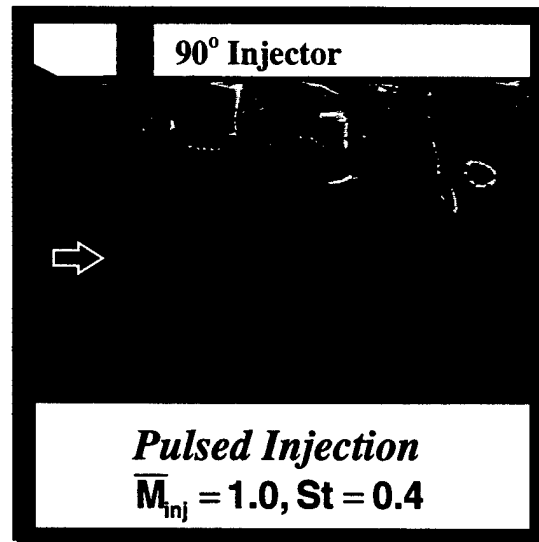


Figure 18: Effect of Pulsing Mach Number on Injector-Jet Structure, Penetration, and Blockage

The effect of pulsing Mach number on injector-jet structure, trajectory, penetration, and blockage is illustrated in Figures 15-17 (described above), 18 and 19. Figure 18 contains a comparison of vorticity contour images taken from a steady-injection solution with an injector Mach number of 1.0 and pulsed-injection simulations with a  $St$  of 0.3 and time-averaged injector Mach number ( $\bar{M}_{inj}$ ) of 0.5, 1.0, and 1.5. Figure 19 contains a vorticity contour image of a pulsing simulation with particles seeded in the crossflow upstream of the injector exit.



**Figure 19: Effect of Injector-Jet Pulsing on Entrainment**

The pulsing Mach number appeared to determine the relative strength of the vortex rings as measured by their respective vorticity magnitude, penetration, diameter, and persistence downstream. Increasing  $\bar{M}_{inj}$  in the case of pulsing produced gains in injector-jet penetration and blockage over that of steady injection at the same time-averaged mass flow rate. Gains in blockage over steady injection were not observed until  $\bar{M}_{inj}$  was increased above 0.5 (i.e. peak Mach number during pulsing greater than 1.0). This result suggests that an increase in blockage over that of the steady case was primarily related to an increase in the time-averaged momentum flux. Images in Figure 18 revealed that increasing  $\bar{M}_{inj}$  caused vortex rings to penetrate deeper into the crossflow both in the near and far field region. At  $\bar{M}_{inj}$  of 1.5, the rings began to incline relative to the nozzle upper and lower surfaces as they convected downstream. While increasing  $\bar{M}_{inj}$  produced a significant increase in penetration, the increase in blockage was modest. This finding suggests that entrainment effects may confound the relationship between injector-jet penetration and blockage, for the case of pulsing. As noted above, pulsing promoted entrainment of the nozzle crossflow as evidenced by the growth in ring diameter. Simulations also revealed that the vortex rings not only entrain mass flow within their own structure, but also effectively entrain mass flow within the wake zone between injector pulses and their associated rings. Particle trajectories seeded in the nozzle crossflow in Figure 19 illustrate this mechanism of increased entrainment.

### 3.4 Effects of Injector Jet Geometry

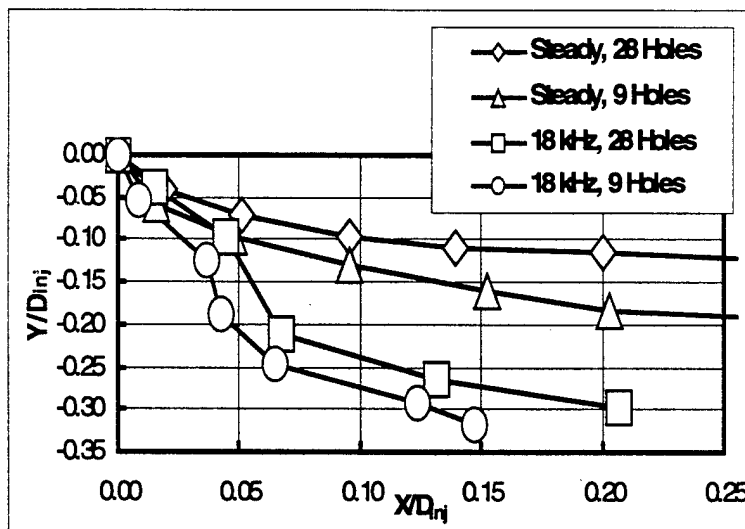


**Figure 20: Effect of Number of Injection Holes on Penetration**

The effect of injector exit geometry on injector-jet structure, trajectory, penetration, and blockage is illustrated in Figures 20-23. Figure 20 contains measurements of injector-jet trajectory and penetration in the near-field region of the injector exit. These measurements are shown with varying number of injector holes across the span of the nozzle upper surface. Figure 21 summarizes the effect of the number of injector holes on blockage for the cases of steady and pulsed injection. Figure 22 contains a comparison of vorticity contour images taken from a steady-injection solution with an injector angled at 90 degrees, a steady-injection solution with an injector angled at 45 degrees, and a pulsed-injection simulation with an injector angled at 45 degrees. Figure 23 contains measurements of injector-jet trajectory and penetration in the near-field region of the injector exit for the case of steady and pulsed injection with both injectors angled at 90 and 45 degrees opposed to the crossflow.

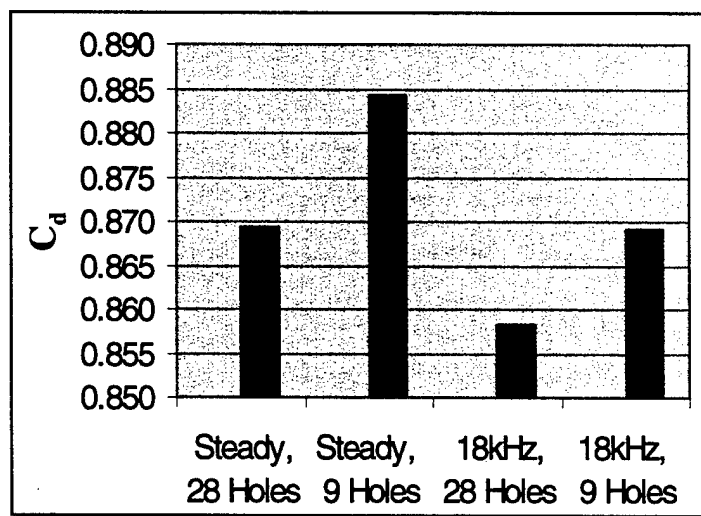


**Figure 21: Effect of Number of Injection Holes on Blockage**

The effect of increasing the number of injector holes across the span of the nozzle was evaluated for the same injector conditions. As the number of holes was increased, the injector diameter was subsequently reduced to maintain a constant-total injector area. Increasing the number of holes from nine to 28 decreased penetration. However, blockage was increased for the cases of steady and pulsed injection. Intuitively, increasing the number of holes across the span of the nozzle while keeping the total injector area constant decreases the area and momentum of each individual injector jet, and therefore, could decrease penetration. Holdeman et al. (1977) alluded to this type of relationship in a study of steady injection in a low-speed, confined crossflow. This simplified explanation assumes that the interaction effects between adjacent injector jets are secondary. The effect of increasing blockage, however, suggests an additional factor related to the injector area distribution across the nozzle span. For the case of steady injection, this observation is consistent with that of Miller et al. (1997). Increasing the number of holes increases the percentage of total span-wise distance covered by the injectors. It is believed that, while penetration may decrease for this case, closer spacing between injectors reduces the amount of leakage and entrainment occurring between the injector-jet streams, which would increase blockage.

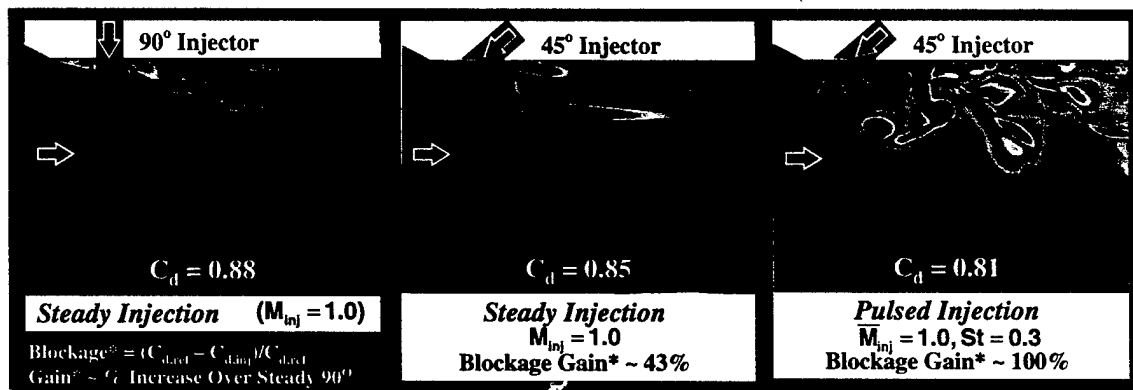


**Figure 22: Effect of Injector Angle on Injector-Jet Penetration and Blockage**

Maximum injector-jet penetration and blockage for the cases of steady and pulsed injection was obtained when the injector was angled upstream into the crossflow at 45 degrees. The trajectory of the angled injection stream achieved a much greater penetration in the near-field region, as shown in Figures 22 and 23. Figure 22 reveals a very complex train of vortex ring structures with noticeable ring-ring interaction and merging. For the case of steady injection, this observation is consistent with that of previous efforts (Federspiel, 1995; Miller et al., 1995, 1997). Perhaps more significant is the observation that the effect of pulsing on increased blockage (at the same  $\bar{M}_{inj}$ ) is far greater for the angled injector geometry, than for the transverse injector geometry. Blockage is defined here as the reduction in  $C_d$  below the reference case of no injection ( $C_d = 0.95$ ). The blockage gain is defined as the increase in blockage over the 90° steady case, as defined in Figures 18 and 22. The blockage gain for the 90° pulsing case was only 14%, while the blockage gain for the 45° pulsing case was 100%. While angling the injector in the steady case made 43% of this gain, the remaining 57% is clearly due to the effect of pulsing on

blockage. It is believed that by angling the injector into the crossflow, the entrainment effect of the vortex rings is suppressed, and the blockage effect is magnified. These results also suggest that a gain in injector-jet blockage is related to an increase in penetration in the very near-field (and even upstream) region of the injector exit (Figure 23). Gains in penetration in the very near-field region may be more likely to influence the development and displacement of the nozzle sonic line, which influences the effective throat area.

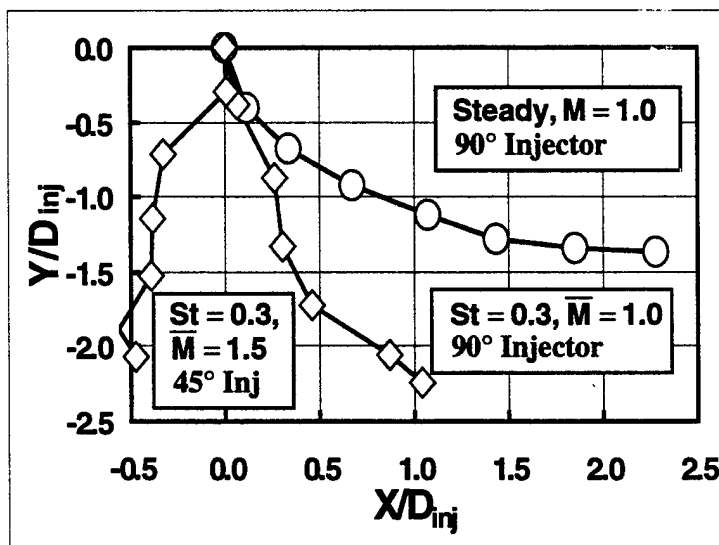


Figure 23: Effect of Injector Angle on Injector Jet Penetration

### 3.5 Effects of Compressibility

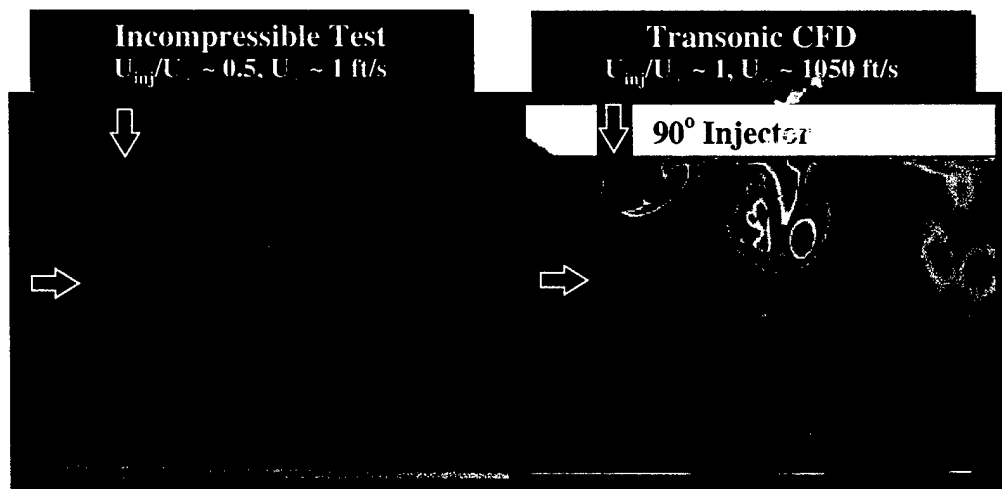
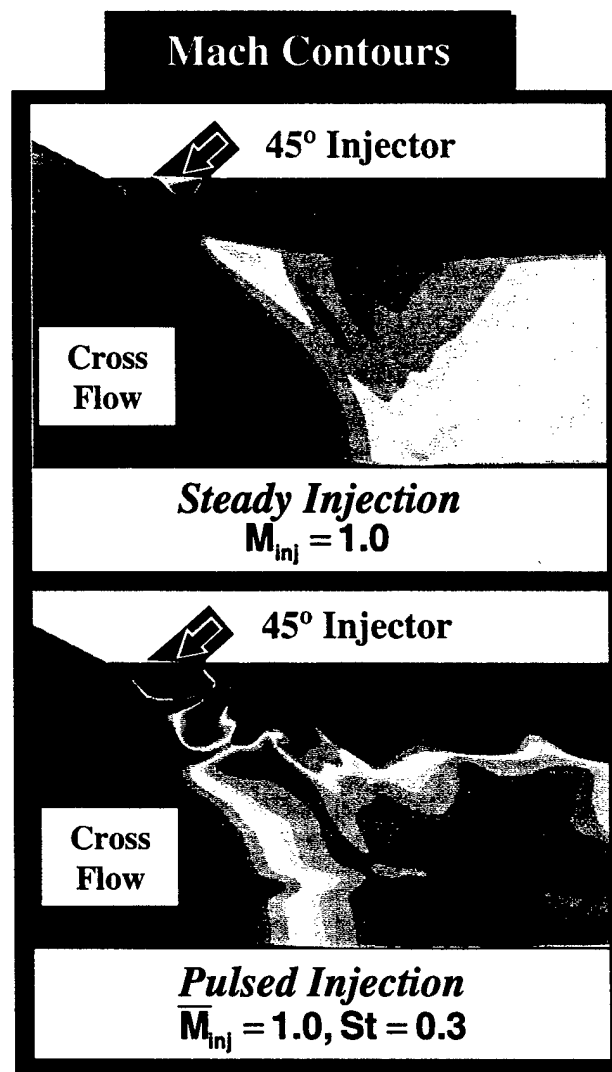


Figure 24: Comparison of Experimental and CFD-Predicted Penetration

Qualitative effects of compressibility at transonic flow conditions on injector-jet structure and penetration are illustrated in Figures 24 and 25. Figure 24 contains a comparison of a vorticity-contour image taken from a pulsed-injection simulation at transonic conditions to a flow visualization image taken from prior water-tunnel testing.

Figure 25 contains a comparison of Mach contour images taken from both a steady and pulsed-injection solution at the same time-averaged mass flow rate and Mach number.



**Figure 25: Effect of Pulsing on Injector-Jet Shock Strength**

Gains in penetration using pulsing were smaller than observed in previous incompressible studies. Figure 24 reveals shows much greater penetration for pulsed injection in the incompressible regime as compared to results in the transonic compressible regime. In the incompressible flow regime, additional velocity (over the steady case) is imparted during pulsing, which yields an increase in instantaneous momentum. This increased momentum during pulsing achieves an increase in penetration over that of the steady case. For the compressible case, Figure 25 shows a dramatic increase in injector-jet shock strength for the case of pulsed injection over that of steady injection at the same time-averaged mass flow rate and Mach number. The additional momentum imparted during pulsing may be partially dissipated in the compressible regime because of increased injector-jet shock strength. These additional losses may contribute to the reduced gain in penetration compared to the incompressible case.

### 3.6 Task Summary with Implications for Actuator Requirements

An investigation of pulsed injection into a confined, expanding crossflow was conducted. CFD simulations were run with varying injector conditions and geometry to evaluate their effect on injector-jet structure, trajectory, penetration, diameter, entrainment, and blockage. Results of these simulations revealed that pulsing generally produced a measured increase in injector-jet stream penetration and diameter over that of a steady injector. The basic mechanism governing this enhanced penetration is believed to be the appropriate formation, spacing, and strength of the vortex rings generated at the injector exit. Injector penetration was a function of pulsing frequency. The vortex-ring diameter generally increased (relative to the exit diameter) in the near field region, as a likely result of the rapid entrainment associated with the regions of high vorticity and shear near the rings. The injector-jet blockage was relatively unaffected by pulsing frequency. Increasing time-averaged pulsing Mach number in the case of pulsing produced gains in injector-jet penetration and blockage over that of steady injection. Gains in blockage over steady injection were not observed until  $\overline{M}_{inj}$  was increased above 0.5 (i.e. peak Mach number during pulsing greater than 1.0). This result suggests that an increase in blockage over that of the steady case was primarily related to an increase in the time-averaged momentum flux. While increasing  $\overline{M}_{inj}$  produced a significant increase in penetration, the increase in blockage was modest. Pronounced entrainment effects may confound the relationship between injector-jet penetration and blockage, for the case of pulsing. Increasing the number of injector holes across the nozzle span decreased penetration, but increased blockage for the cases of steady and pulsed injection. Maximum injector-jet penetration and blockage was obtained when the injector was angled upstream into the crossflow at 45 degrees. Gains in penetration using pulsing were smaller than observed in previous incompressible studies.

The findings in this investigation have several implications for defining requirements of pulsing actuators to be used for increasing injector jet penetration and blockage in the transonic flow regime. To achieve an increase in near-field penetration, actuators must be able to operate at very high frequencies. In this investigation, a  $St$  of 0.3 achieved peak penetration of the injector jet. For a full-scale configuration, this translates to roughly 1500 Hz and as much as 15 kHz for a model-scale configuration. To achieve an increase in blockage, actuators must be able to produce peak exit Mach numbers greater than 1.0 during pulsing. In addition, the flow must be modulated as much as possible during the remaining portion of the pulsing period (modulated to zero flow in the case of this investigation). The actuators should be integrated in a distributed fashion to produce pulsing across an array of injector holes across the span of the flowpath. The injector exit should be directed upstream to oppose the crossflow. This investigation has demonstrated the feasibility of using pulsing to increase injector-jet penetration and blockage in a transonic crossflow. However, limitations on the frequency and exit velocity capability of current pulsing actuators will likely leave further experimental investigations of this technique to future studies.

## 4.0 A Preliminary Experimental Evaluation of Actuators for Pulsed Injection in the Compressible Flow Regime

Previous experimental studies (Vakili et al., 1999; Vermeulen and Ramesh, 1996) of injection into an incompressible crossflow have shown an increase in injector-jet penetration with pulsed injection relative to steady injection. The purpose of the test activity reported here was to experimentally evaluate the capability of available pulsed-injection actuators for application in the compressible flow regime. The basic approach was to measure the output from such actuators used for pulsed injection and show any effects on injector-jet structure, penetration, and blockage of a crossflow.

### 4.1 Nozzle Test Model

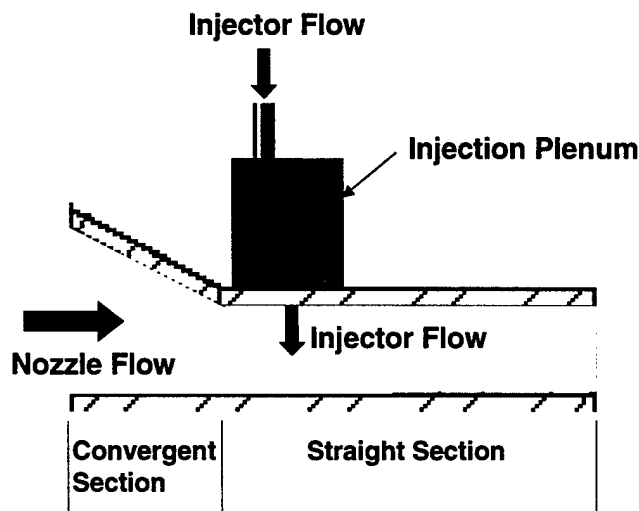
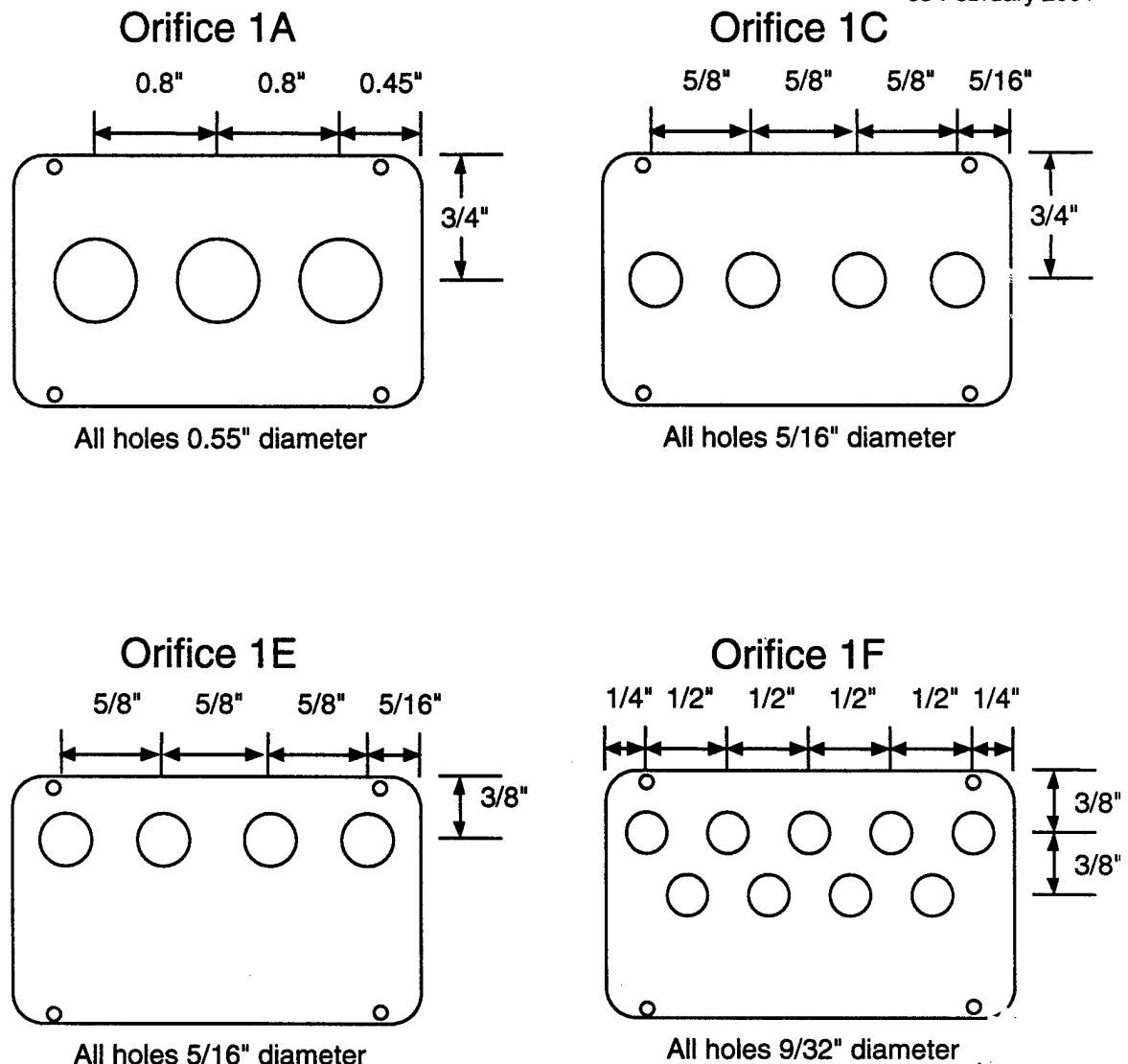


Figure 26: Simple Two-Dimensional Nozzle Model

This experimental task was conducted UTSI. A simple rectangular nozzle model was used for this test. This nozzle provided a realistic transonic flow environment in which to investigate injection for throat area control. As illustrated in Figure 26, the nozzle design consisted of a convergent section (with all convergence due to the converging top plate) followed by a straight, constant area section. Due to manufacturing imperfections, the straight section was not actually constant area. The straight section was very slightly divergent, with the exit area being 1.003 times larger than the inlet. The sides of the nozzle were straight and parallel and included transparent Lexan windows to allow optical access for the use of Particle Imaging Velocimetry (PIV). The top and bottom surfaces of the nozzle straight section included static pressure orifices. Drawings of major nozzle-model parts are included in the Appendix, Section 11.5.

The injected flow entered the nozzle through a set of orifices forming the interface between the injection plenum and the nozzle upper surface.

Figure 27 shows orifice plates designed for this test. Of this set, only the "Orifice 1C" plate was tested. The orifice holes were tapered on the upstream side of the plate.



**Figure 27: Injection Orifice Designs**

## 4.2 Pulsing Devices

Two pulse generating devices were examined in this effort (Figure 28). These were the Allied Signal Fluidic Diverter Valve (ASFDV) and the UTSI Axial Flow Pulse Generator (AFPG). The ASFDV is an adaptation of an "off the shelf" Allied Signal product known as a "supersonic bi-stable amplifier." The device is shown schematically in Figure 29. This device produces pulses by alternately diverting flow into either of two exit legs. For this application, the flow from only one of these legs was injected into the model and flow from the other leg was exhausted to atmosphere. This required modifications to the test facility, which are described in Section 4.3. The ASFDV included an electronic frequency controller/driver for setting and controlling pulsing frequency and had an upper frequency limit of about 400 Hz. By the time testing with this device was underway, CFD-based analytical studies had shown that pulsing frequencies

on the order of 10 kHz (for the current sized model) would be required to produce the kind of vortex structures desired. Though the ASFDV could not attain this frequency range, it was still felt that, even at these low frequencies, useful data on the effectiveness of the actuator could be taken at subsonic speeds.

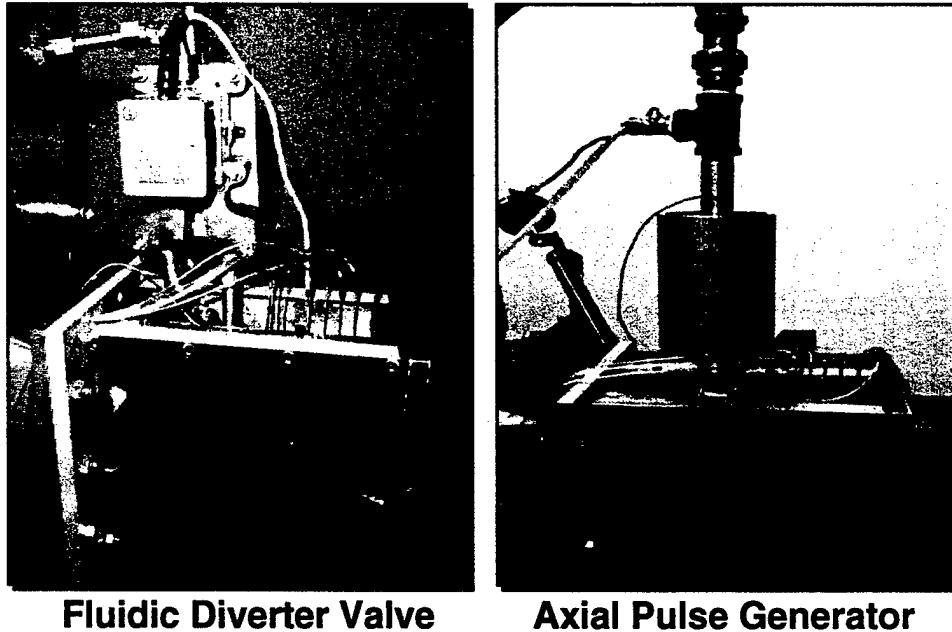


**Figure 28: Two Tested Pulse Generating Devices**

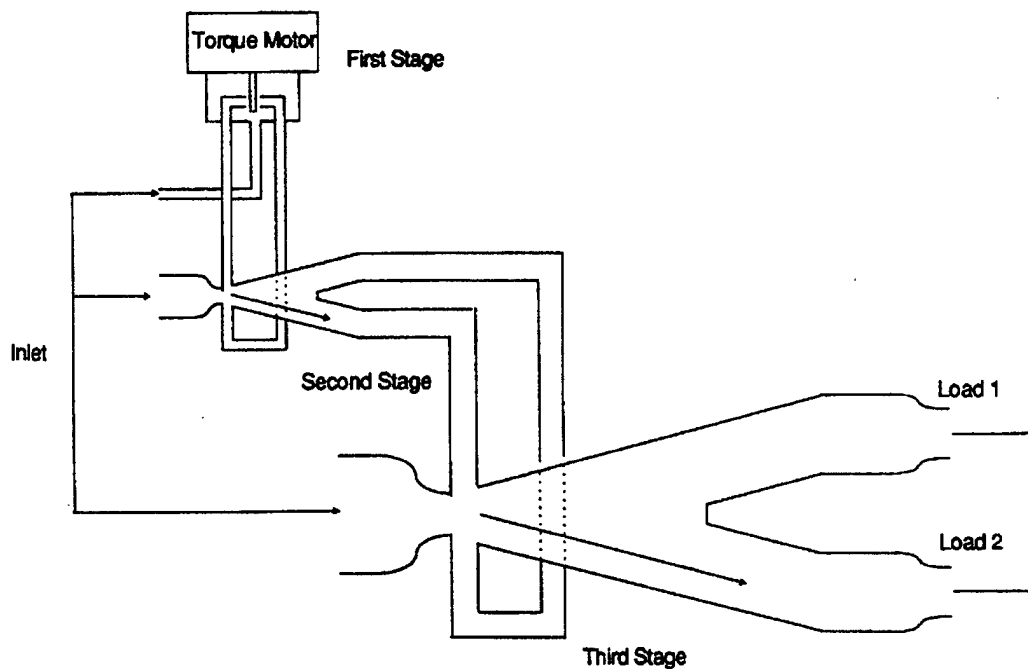


**Figure 29: Allied Signal Fluidic Diverter Pulse Valve**

The UTSI-developed AFPG operates based on flow-generated frequency amplification in a specially designed internal valve geometry. Since this device is

proprietary to UTSI, its design will not be discussed in detail. This device may be operated in active or adaptive modes and may reach frequencies up to 8.0 kHz. Unlike the ASFDV, this device produced only one outlet stream, resulting in a simpler integration into the model/test facility than for the ASFDV.

### 4.3 Test Facility

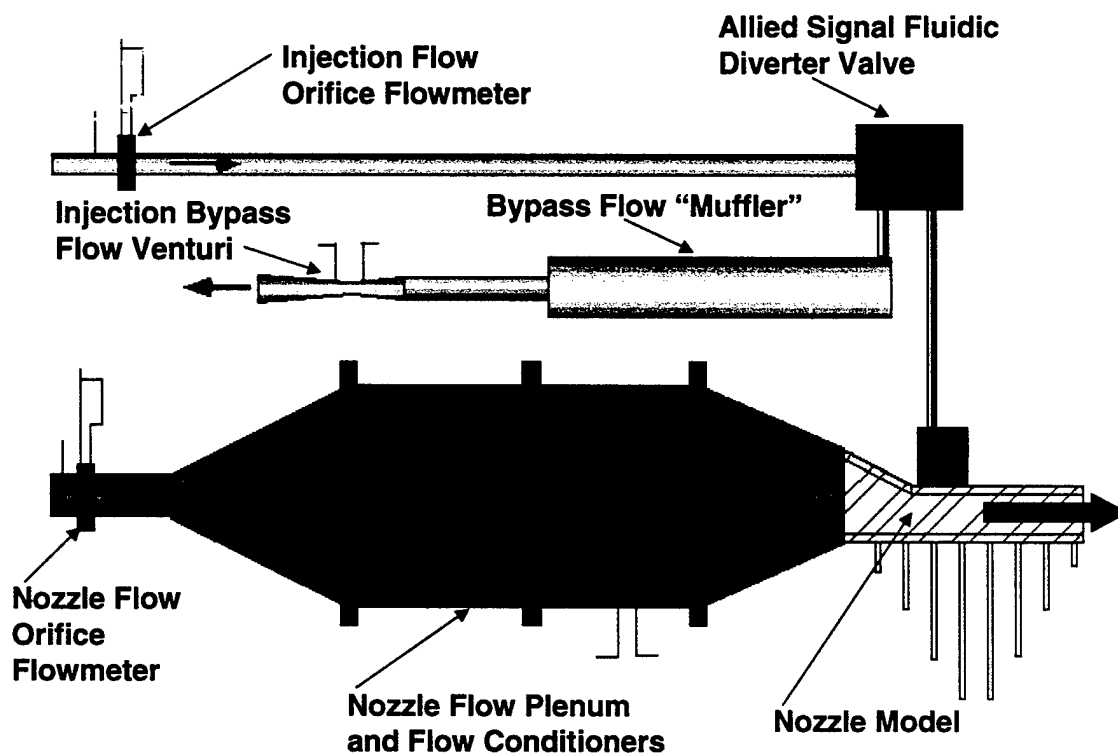
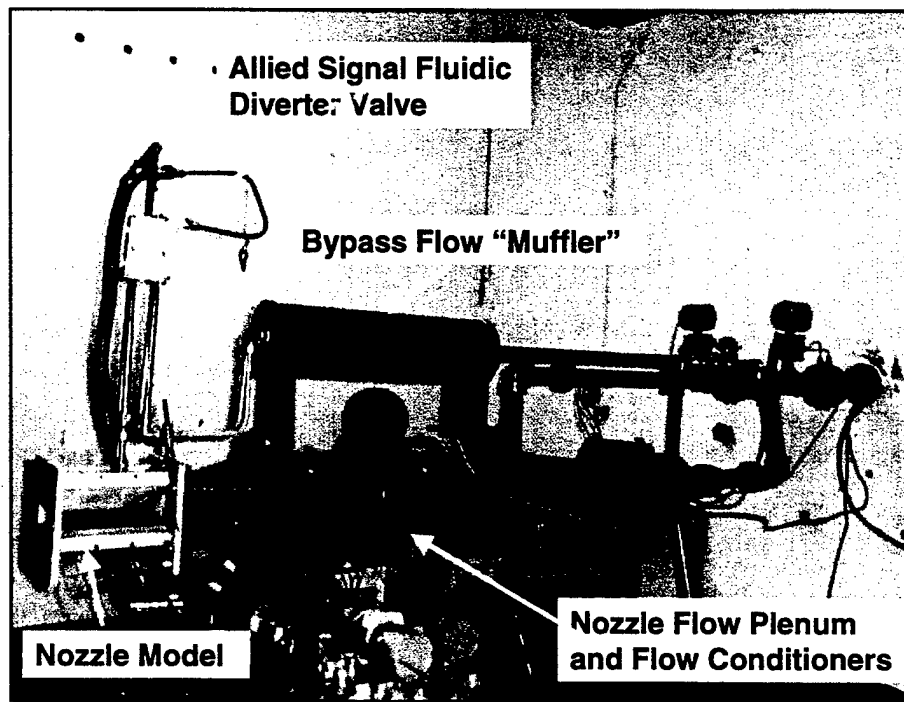


Figure 30: Nozzle Model Installed in UTSI Facility

The model described above was installed in a flow-calibration test rig at UTSI. Figure 30 schematically illustrates the installation of the nozzle model in the test facility. High-pressure air for the nozzle and injection flows was supplied from storage tanks. The nozzle flow rate was set at about 4.0 lbm/sec. Injection flow rate was varied from zero to about 20% of the nozzle flow. Nozzle and injection flows were measured with ASME flow orifices. Also illustrated in Figure 30 is the installation of the ASFDV in the test rig. As discussed earlier, this device produced flow pulses by switching the injection flow alternately between two valve-exit flow paths. One exit flow fed the injector plenum. The other exit flow bypassed the model and was exhausted to atmosphere. If the valve were operating with equal flow resistance on each of the exits, the injection flow would be split equally between the two exits. However, equal resistance could not be guaranteed in this experiment, thus complicating the determination of the actual flow rate entering the injection plenum. This challenge was compounded by the unsteady nature of the flow downstream of the pulsing device, since conventional flow meters require steady flow. To overcome this difficulty, the unused flow exiting the pulsing valve (the bypass flow) was routed through a "muffler" to eliminate the pulses and then through a venturi for flow rate measurement. The flow entering the injection plenum could then be calculated as the

difference between the flow measured at an upstream injection flow meter and the bypass flow venturi meter. Figure 31 is a photograph of the test setup illustrated schematically in Figure 30. The other pulsing device used in this test, the AFGP, did not split the flow and, therefore, did not require the "bypass/muffler" approach described above.



**Figure 31: "Muffler" Installation Required with Allied Signal Device**

Steady state pressure measurements were made with Rosemont pressure transducers calibrated to the ranges expected in the test. These measurements included model wall static pressures and plenum pressures. Two Kistler 25 psid dynamic pressure transducers were used for dynamic pressure measurements. Flow temperatures were measured with thermocouples. Data acquisition and processing was performed by a PC-based system running the LabView program.

Bench testing of the pulsing devices employed a Thermal Systems Incorporated (TSI) IFA 300 hot wire/hot film system for waveform verification. The intent was to test both hot-film and hot-wire probes for this application to verify that there was no time-response limitation associated with the hot film (which had a frequency response of about 5 kHz). However, the hot wire probes proved too fragile for this application, so data was acquired only with the hot film probe. The probes were calibrated for velocities up to about 350 ft/s (107 m/s). Though this was lower than the velocities expected in the test, it was felt that analysis of the voltage output from the IFA 300 would be adequate to verify the pulse waveform of the pulsing devices.

A TSI, Inc. PIV system was available for use in nozzle model flow field velocity and vorticity measurement. The nozzle model sidewalls were made of transparent Lexan to allow optical access. PIV measurements require seeding the flow with very small

particles. Various water atomizers were tried unsuccessfully for this. Ultimately, it was found that micron sized aluminum particles suspended in alcohol provided adequate seeding for PIV. This technique had previously been used at NASA Glenn Research Center (Wernet and Bright, 1999).

#### **4.4 Test Approach**

A build-up approach was employed in this test effort to help ensure proper operation of the pulsing devices, the nozzle model, and the facility. Bench testing was performed for the ASFDV pulsing device before incorporation into the nozzle model. This allowed the UTSI test team to become familiar with the operation of this device and provided an opportunity to study the uninstalled pulse waveforms. The ASFDV pulsing device was tested at a pulsing frequency of 200 Hz. However, since only one of the two alternating exit flows were intended for injection into the model, the effective pulsing frequency was 100 Hz. Since the AFPD device used in this effort was built at UTSI, the test team was already familiar with its operation and no additional bench testing was required. During the course of each stage of testing, CFD analyses were performed at LM to make comparisons with the test results.

A standard reference nozzle with known performance is typically used for facility verification. A comparison of the known reference performance with data produced by the facility allows identification of model or facility problems. In this case it was felt that the model was sufficiently simple to allow analytical performance predictions (for a no-injection case) to substitute for known performance data. CFD analyses, as well as simple 1-D theory performance (nozzle discharge coefficient and pressures) predictions were compared with initial test data for a no-injection case. A slight discrepancy was found between the model-design and as-built dimensions. Other typical testing problems (model leaks, etc.) were also identified and dealt with. In addition to serving as a facility checkout exercise, testing the model with no injection provided baseline performance data to compare with steady and pulsed-injection data.

After testing with no injection, the model was tested with steady injection. This helped check out the flow measurement for the injection system and provided a reference level against which to compare the effect of pulsed injection. Performance measurements included nozzle flowrate, injection flowrate, flow pressures, and flow temperatures. Nozzle discharge coefficients were calculated based on these measurements. During this testing, the main nozzle pressure ratio (NPR) was held constant as injected flow was varied from zero to about 20% of the main nozzle flow. Main nozzle discharge coefficient was tracked as injection flow was varied to determine the effectiveness of the injected flow for producing blockage.

After steady flow testing, pulsed injection testing was performed. Data measurements included the same data as for steady injection, plus dynamic pressure measurements for the injected flow. PIV measurements were also taken for pulsed as well as steady-injection cases.

#### 4.5 Results and Discussion

Bench testing of the ASFDV revealed that its operation was sensitive to control pressure (the pressure of the control flow used to induce switching of the flow from one exit to the other). Control pressure was varied until an appropriate level was found to produce pulsing. Hot film measurements were made to determine the pulse waveforms. As indicated earlier, the calibration of the hot film probe was not adequate to accurately measure the maximum pulsed flow velocities. Therefore, the output from the hot film system can only be used to help understand the waveform shape, rather than absolute levels. Figure 32 contains an example of the hot film data collected. These data indicate that the flow at the device exit does not display a square waveform, which was considered ideal for pulsed injection (see Section 11.5). In addition, the data indicated that the injected flow did not completely modulate (shut off at the bottom of each pulse). It is felt that the capacitance and impedance of the flow passages in the valve are at least partly responsible for these two observations. It is also known that the pulsing performance of this type of device is sensitive to the pressure ratio between the device inlet and exit. If this pressure ratio is above some upper limit, some of the flow intended for the "on" side will spill over into the circuit, which is supposed to be off. If this pressure ratio is below some lower limit, the "off" side will actually flow in reverse. These upper and lower limits were not known to the UTSI test team and these sensitivities were not understood at test time. The sensitivity of this device to pressure ratios and ducting characteristics presents challenges to incorporating it into a working injection system.

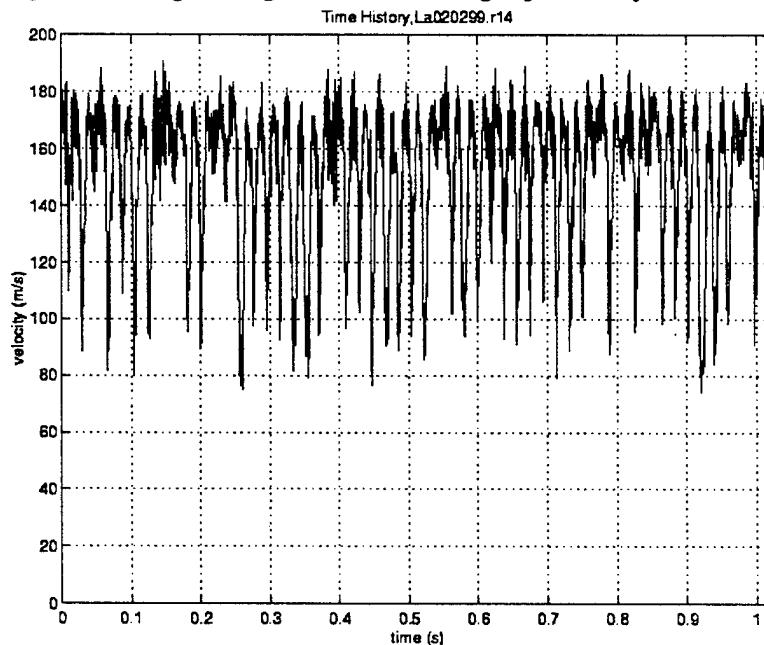


**Figure 32: Hot-Film Data from Bench Test of ASFDV**

Initial testing of the nozzle model was accomplished with no injection. No-injection data provided a means of checking the operation of the model and the facility before the more complex runs with injection. Initial nozzle-wall-pressure comparisons between 2-D CFD analysis and test results with no injection revealed significant

differences. These differences led to a detailed inspection of the nozzle model hardware, which revealed several leaks that were subsequently sealed. It was also found that a 3-D CFD analysis was necessary to capture the sidewall boundary-layer growth, which is necessary to determine the correct shock location.

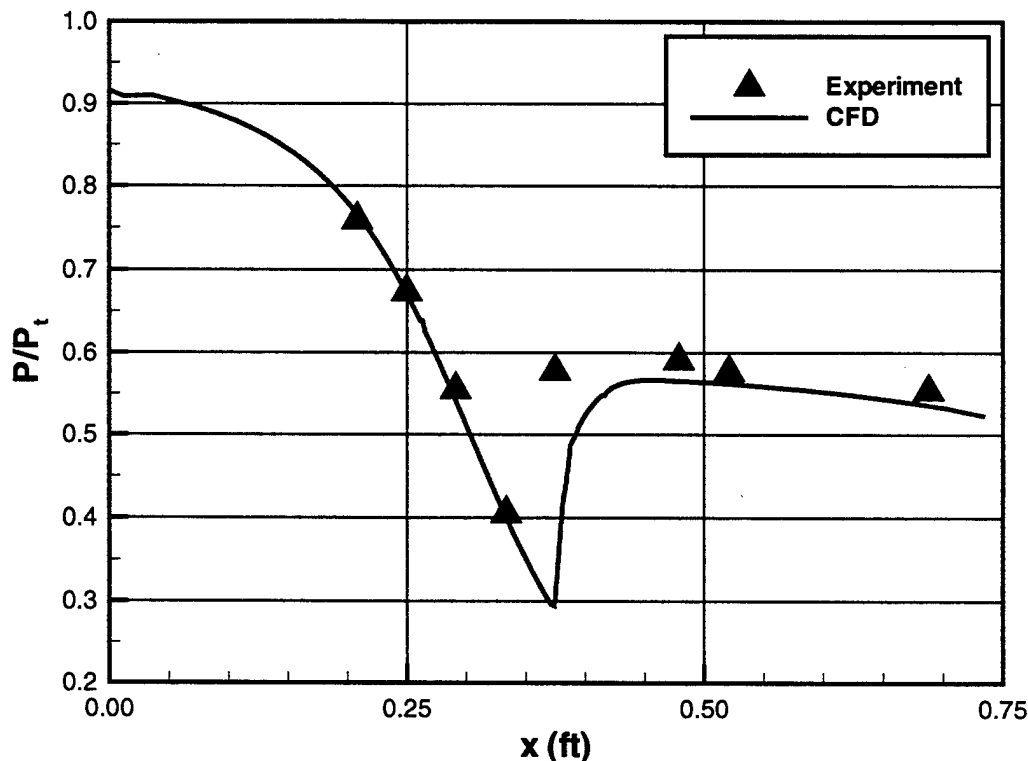


**Figure 33: Comparison of Test and CFD Lower Surface Pressures for  $NPR = 2.0$ , No Injection**

After these issues were dealt with, reasonable agreement was seen between CFD predicted wall pressures and those measured in the test, as seen in Figure 33. Unless otherwise indicated, data shown in this section are for  $NPR = 2.0$ .

An examination of the initial mass-flow-measurement data from the test revealed a problem with the flow calculation procedure and the geometry of the primary flow orifice used at UTSI. CFD analysis at LM was used to predict a nozzle discharge coefficient ( $C_d$ ) of 0.95, while the test data showed a value of 1.2 (an impossibility). After correcting the flow calculation procedure, test data showed a value of 0.93. The flow measurement orifice was also found to be outside of ASME specifications. For this reason, it was concluded that the 2% discrepancy between test and CFD was largely due to accuracy limitations of the primary flow orifice. Therefore in subsequent injection-on investigations,  $C_d$  comparisons between test and CFD focused on the slope of the  $C_d$  versus injected-flow ratio curves rather than the absolute levels.

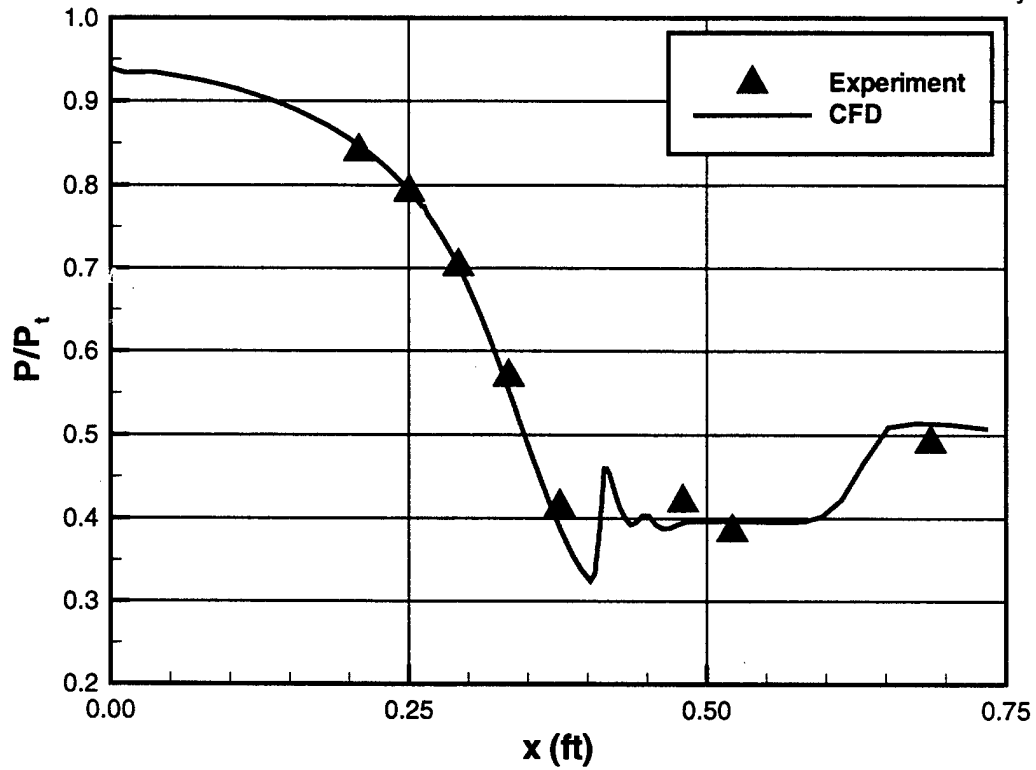


Figure 34: Comparison of Test and CFD Lower Surface Pressures for  $NPR = 2.0$ , 10% Injection

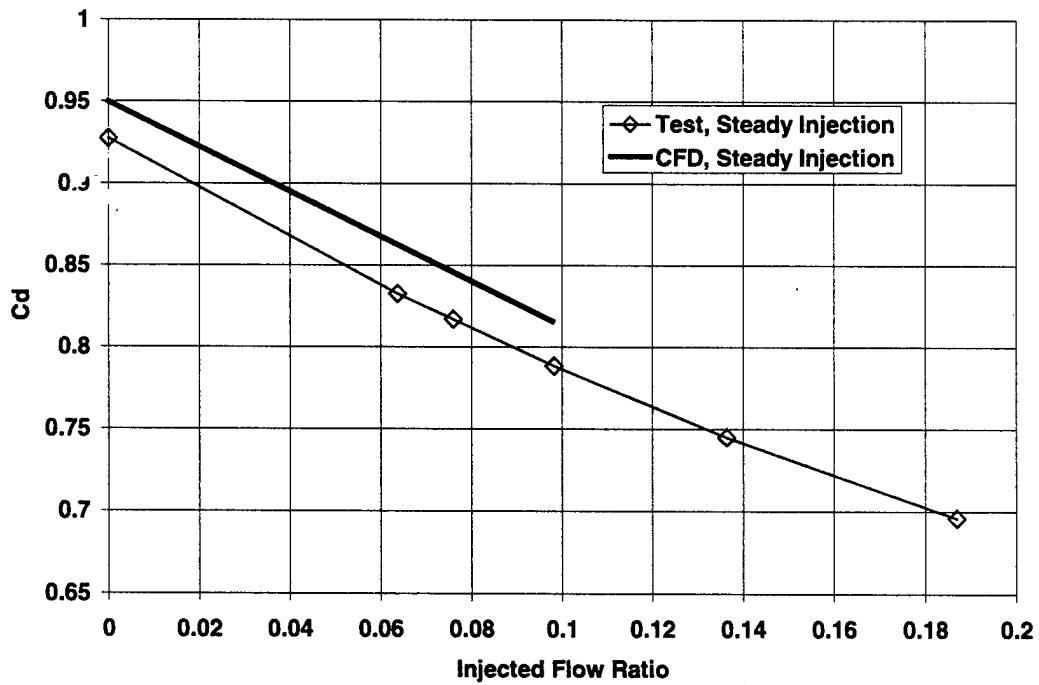
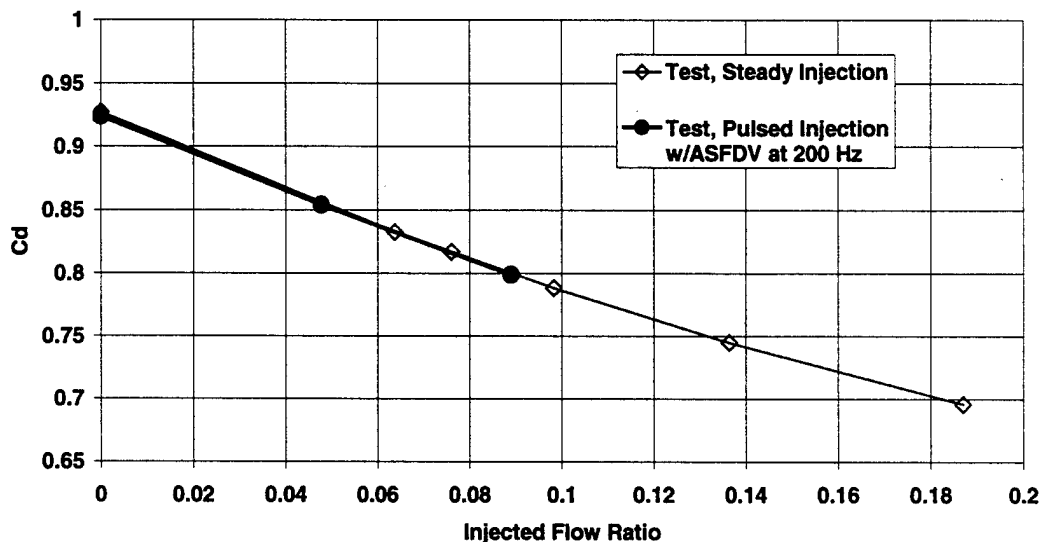


Figure 35: Nozzle Discharge Coefficient with Steady Injection for  $NPR = 2.0$

After basic checks were performed with no-injection data, the model was run with steady injection. Again, comparisons were made between test and analysis. Figure 34 summarizes a comparison of test and 3-D CFD-derived nozzle upper wall pressures for an injected flow ratio (ratio of injected flow to main nozzle flow) of 10% at  $NPR = 2$ . As can be seen, the agreement is quite reasonable. Figure 35 shows a comparison of test and CFD-based nozzle discharge coefficients for steady injection. As indicated earlier, the difference in  $C_d$  levels is likely attributable to accuracy limitations of the primary flow measurement orifice. However, it is seen that the slopes of the curves agree quite well.



**Figure 36: Effect of Pulsed Injection on Nozzle Discharge Coefficient for  $NPR = 2.0$**

Figure 36 summarizes a comparison of discharge coefficients for steady injection and pulsed injection with the ASFDV at 200 Hz (at injection plenum). These data show no discernable impact on flow blockage due to pulsing as implemented here. Results of CFD simulations (discussed in Section 3.0) revealed that a much higher pulsing frequency (e.g. kHz) was required for increased penetration of the injector jet. To achieve an increase in blockage, simulations also showed that the injector exit peak Mach number should be varied between a peak value greater than 1.0 and a minimum near zero. The relatively low frequency, peak velocity, and extent of modulation provided by the ASFDV was likely inadequate to achieve an increase in blockage. Earlier discussions addressed challenges of producing a suitable waveform with the ASFDV in bench testing. With the device installed in the model, the situation is even more challenging due to the additional impedance and capacitance of the ducting and the injection plenum. These effects tend to dampen and distort the pulses actually entering the model. Figure 37 shows injection plenum pressure measured with dynamic pressure instrumentation for the ASFDV.

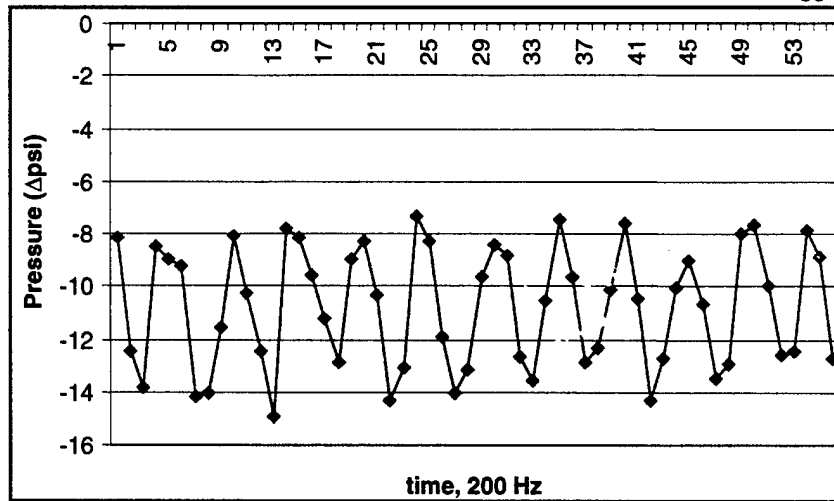


**Figure 37: Injection Plenum Pressure with the ASFDV**

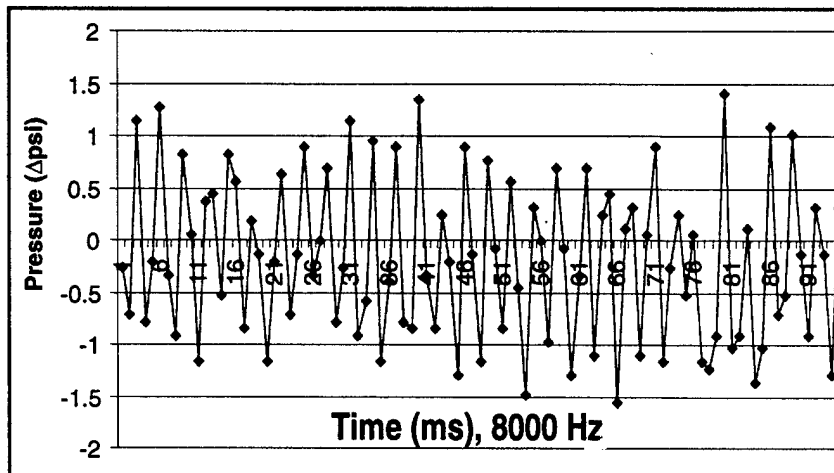


**Figure 38: Injection Plenum Pressure with the AFPG**

Figure 38 shows injection plenum pressure with the AFPG operating. As seen in Figure 38 this device produces higher frequency pulses than the ASFDV, but does not produce the desired square or rectangular waveform. In addition, comparison of Figure 37 and Figure 38 shows reduced amplitude of the flow pulses for the AFPG relative to the ASFDV. As discussed earlier, the AFPG has only one exit flowpath and did not need the bypass system used with the ASFDV. However, this device faces similar challenges due to impedance and capacitance of the ducting and the injection plenum. Unless a way can be found to “tune” the entire pulsed flow delivery flowpath, any pulse generator will suffer from pulse damping and distortion due to ducting/plenum impedance and capacitance. During the course of this test, efforts were made at UTSI to reduce ducting lengths between the pulsing devices and the injection plenum and, also, to reduce the volume of the injection plenum to improve pulsing performance. However, no discernible benefit was achieved.

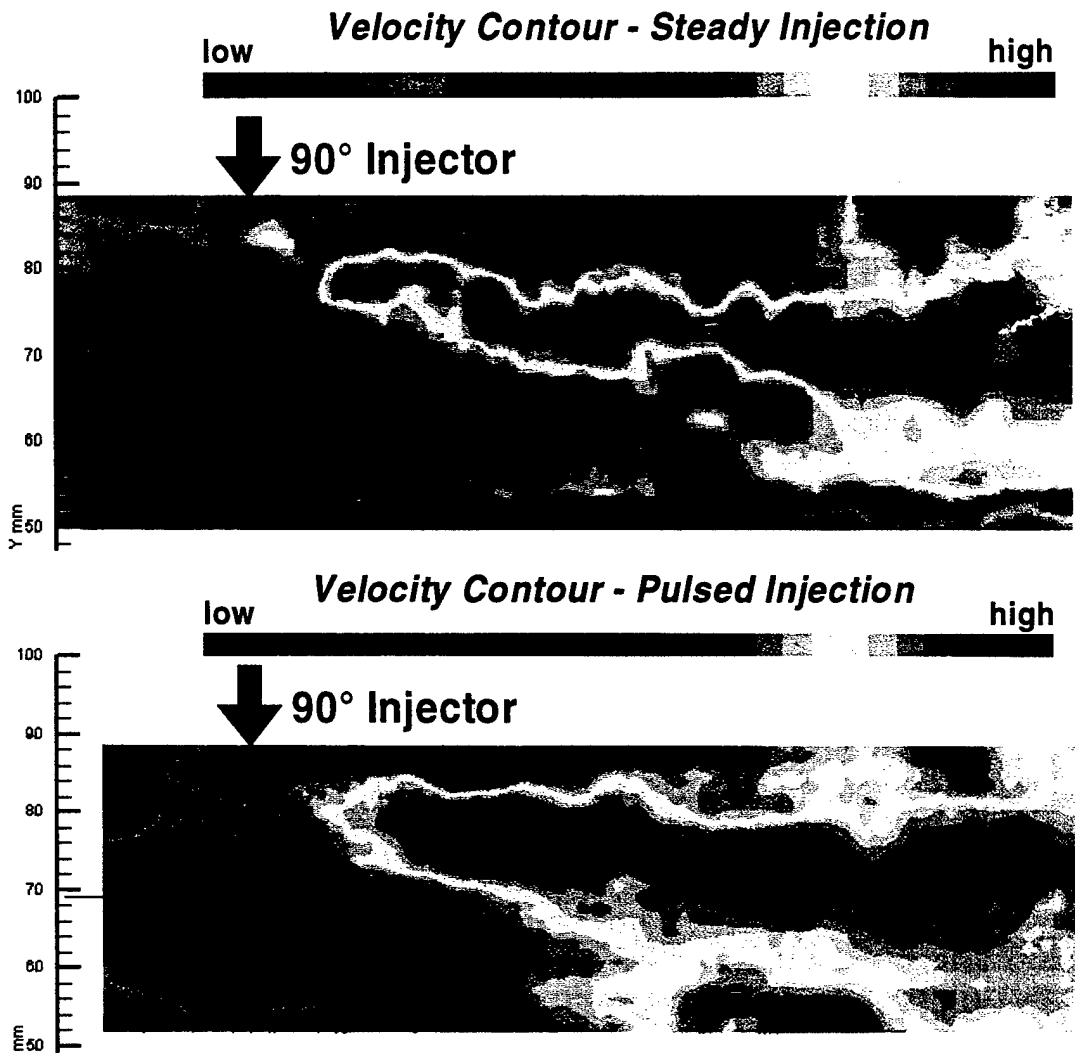


**Figure 39: PIV Results for Steady and Pulsed Injection**

Figure 39 contains velocity data taken with PIV for both steady and pulsed injection. The pulsed injection data was taken with the AFPG actuator. The PIV measurements were taken to qualitatively investigate the flow field produced by the UTSI pulsing system. Results in Figure 39 revealed some small differences in injector-jet penetration and mixing between steady and pulsed injection. No discernable vortex-ring structures were observed in the case of pulsed injection. These results confirmed that the pulsing system (actuator plus ducting) were inadequate to generate the type of disturbance necessary to see increases in penetration or blockage

#### 4.6 Task Summary

Two pulsing actuators were experimentally evaluated for modulating an injected stream issuing into a nozzle crossflow. The nozzle model was initially tested with no injection and with steady-state injection. CFD-based wall-pressure predictions with no injection and with steady-state injection agreed reasonably well with the test measurements at comparable conditions. Bench test measurements on the ASFDV revealed that the flow at the device exit did not display a square waveform, which was considered ideal for pulsed injection. The data also indicated that the injected flow did not completely modulate (shut off at the bottom of each pulse). Test results using the ASFDV to pulse the injected flow in the nozzle revealed no discernable gain in blockage over that of a steady injector case at a comparable mass flow rate. Unsteady pressure measurements in the injector plenum showed a relatively weak and quasi-periodic waveform. The stability of the measured ASFDV waveform was found to be sensitive to differences in backpressure of the two output legs. It also is believed that the capacitance of the flow passages in the valve and injector are partly responsible for the relatively weak output waveform. Unsteady pressure measurements in the injector plenum using the AFPG showed a relatively high frequency capability ( $\sim$ kHz), but the output waveform at the injector was also relatively weak and non-periodic. PIV measurements of the nozzle flow field revealed a discernable increase in injector-jet penetration and spreading using the AFPG to pulse the injected stream, however, no discernable vortex ring structures were observed. These experimental results are considered to be inconclusive regarding the use of these two actuators for pulsed injection in this application. Unfortunately, the UTSI test team was unable to overcome difficulties with actuator operation and adverse effects of capacitance in the injector ducting.

Lessons learned during the course of this experimental investigation are described below. CFD simulations were used toward the latter portion of testing to reveal problems with the integration of the actuator into the injector plenum. Unfortunately, the CFD simulation methodology was not completed until much of the testing was already done. In retrospect, future experimental efforts of this nature should include a detailed CFD evaluation of the injector and associated ducting geometry to guide its design prior to testing. The length and volume of the ducting between the actuator and injector should be minimized to avoid adverse capacitance and dampening effects of the pulse waveform. The ASFDV needs to be carefully integrated into an injector system to ensure that the output legs are relatively load-balanced.

## 5.0 A Computational Investigation of Pulsed Ejection

### 5.1 Pulsed Ejection Technique & Benefits

Various means of supplying high-pressure air for fluidic injection have been considered (Miller et al., 1995; Federspiel, 1995). Engine-compressor bleed is most suitable in terms of pressure (actually providing an excess of pressure), but significant engine performance penalties are incurred when large amounts of compressor bleed are extracted. Removing air from the engine fan stream incurs less engine performance loss, but fan bleed has inadequate pressure for this application. An alternate approach is the use of engine compressor bleed in an ejector, or jet pump, arrangement where a small amount of compressor bleed is used to pump a larger amount of engine fan air or freestream air to pressure levels suitable for fluidic injection. An ejector of this type employs a steady high-pressure primary flow to entrain a lower pressure secondary flow, with the resulting mixed stream having a pressure between that of the primary and secondary flows. For fluidic nozzle applications, it is desired to maximize the amount of secondary flow pumped per unit primary flow in order to reduce the primary flow requirements (and associated engine performance penalties). An attractive approach for increasing the efficiency of ejector systems as described above is the use of pulsed ejection. As shown in Figure 40, this approach uses a pulsed high-pressure primary stream to provide greater entrainment of and mixing with a co-annular secondary stream. This approach could greatly reduce the primary flow required to pump a secondary flow for fluidic injection.

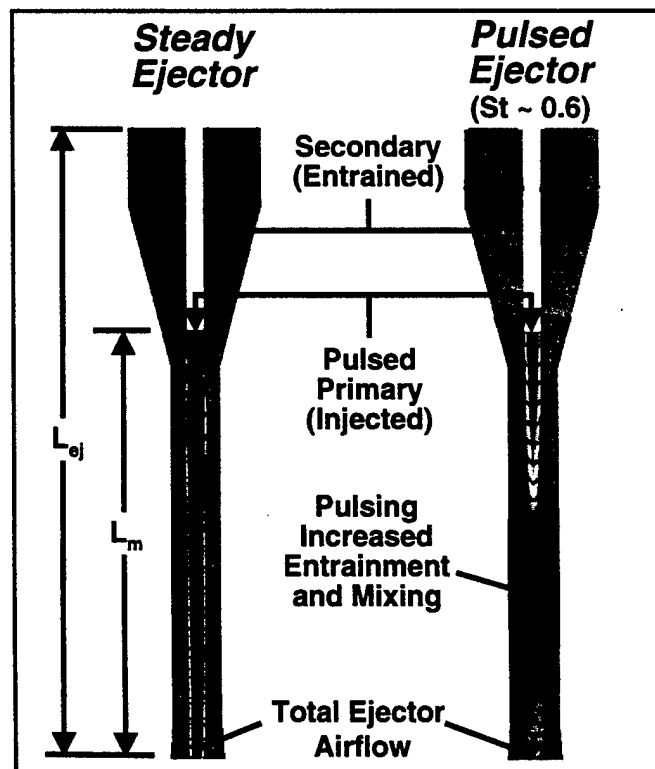


Figure 40: Pulsed Ejector Schematic

Aircraft nacelle ventilation is another application that may benefit from pulsed ejection. Modern aircraft, such as the F-16, use a steady ejector system for nacelle cavity ventilation. A nacelle-ventilation system using a pulsed ejector would have reduced primary mass-flow requirements.

## 5.2 Investigation Approach

An investigation of the pulsed-ejection technique was undertaken to characterize the effects of governing parameters on ejector entrainment. The performance of pulsed-ejector systems was evaluated using the CFD simulation methodology described in Section 2.0. CFD simulations were run to investigate the effects of the following parameters on ejector pumping efficiency: frequency or Strouhal No. based on ejector length ( $St = f \cdot L_{ej} / c$ ), the ratio of ejector mixing tube area to primary flow area, and ejector mixing tube length. The performance of the pulsed ejector was compared with that of a steady ejector.

Lockheed Martin Aeronautics Company's FALCON CFD code was used to perform the analyses. Two-dimensional, axisymmetric solutions were used to determine the sensitivity of ejector pumping ratio to the governing parameters. Axisymmetric CFD solutions were run LES with no model. In these simulations, axisymmetric unsteady structures develop, but the solutions is constrained such that 3-D turbulence is not simulated. The unsteady axisymmetric structures give a reasonable estimate of the mixing processes in the ejector. These solutions provide an efficient means to assess the influence of design parameters for pulsed ejection. The final, detailed evaluation of pulsed-ejector performance was done using 3-D CFD. The 3-D CFD solutions were run using the LES turbulence model.

The axisymmetric CFD grids used for this study contained 5,943 grid points and the 3-D CFD grids contained 240,072 grid points. A time step of  $1.0 \times 10^{-6}$  seconds was used for all CFD runs in the pulsed ejector evaluation. Over the range of frequencies used, this gives between 125 and 500 time steps per pulsing cycle.

Simulations were performed using cold air for both the primary and secondary streams. In order to allow for the possibility of flow reversal at the secondary flow entrance, the secondary flowpath was attached to a large-volume chamber, which was maintained at constant pressure. Likewise, the ejector mixing tube exit exits into a second large-volume chamber. The simulation of the pulsed primary was achieved using a pulsed-flow boundary condition in the FALCON code.

The baseline ejector configuration was as follows:

- ✓ Mixing Tube/Primary Area Ratio: 3
- ✓ Primary/Secondary Total Pressure Ratio: 3
- ✓ Mixing Tube Length/Diameter: 13.5

### 5.3 CFD Investigation

#### 5.3.1 Steady-Jet Ejector Characteristics

Steady-jet (non-pulsed) ejectors were simulated using CFD to determine the effects of ejector geometry on the natural frequencies of the ejector. The analyses were performed using a primary jet total pressure ratio of 1.5. Fast-Fourier-Transform analyses were performed on the time history of the secondary mass-flow rate to determine the natural frequencies of the ejector.

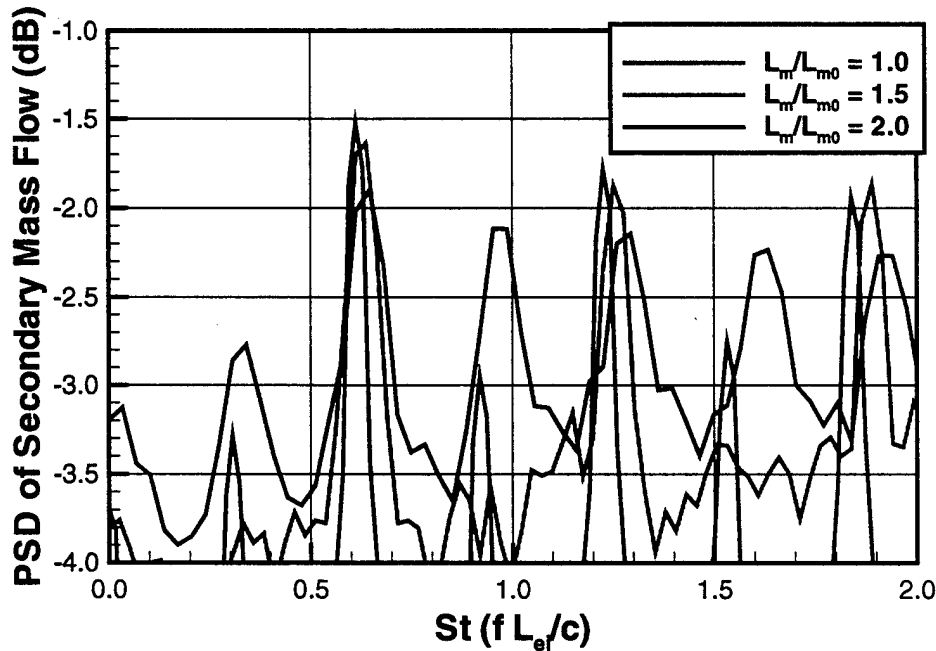


**Figure 41: Effect of Ejector Length on Frequency Response**

Figure 41 shows the effect of ejector mixing tube length on the frequency response of the ejector as measured by a power spectral density (PSD) analysis of the secondary mass flow rate. Ejector lengths of 1.0, 1.5, and 2.0 times the baseline length were evaluated. Note that the Strouhal number of the natural modes remains approximately constant with ejector length. For each of these ejector lengths, the strongest natural mode occurs at a  $St$  of 0.62.

Figure 42 shows the effect of ejector mixing tube area on the frequency response of the ejector. Mixing tube areas of one and two times the baseline area were evaluated. Observe that the Strouhal number of the natural modes increases from 0.62 to 0.68 as the mixing tube area is doubled. This is an increase of almost 10%.

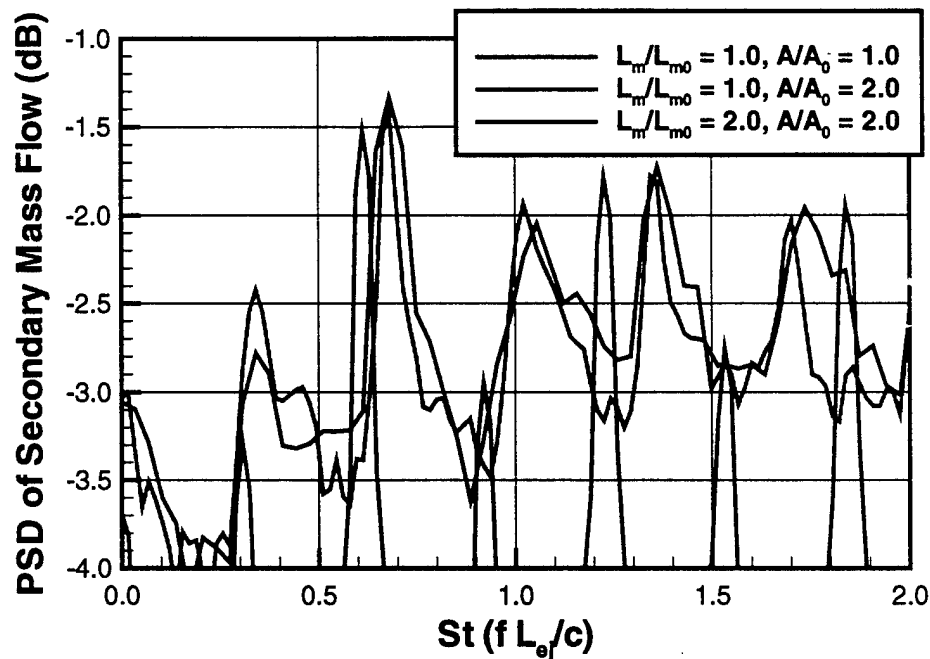
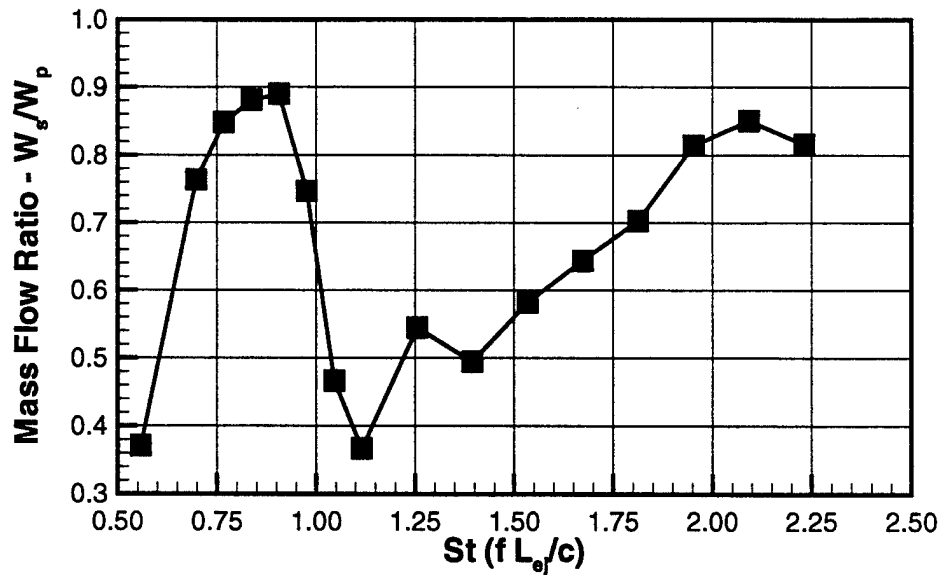


**Figure 42: Effect of Mixing Tube Area on Frequency Response**

### 5.3.2 Pulsed-Jet Ejector: Effect of Frequency

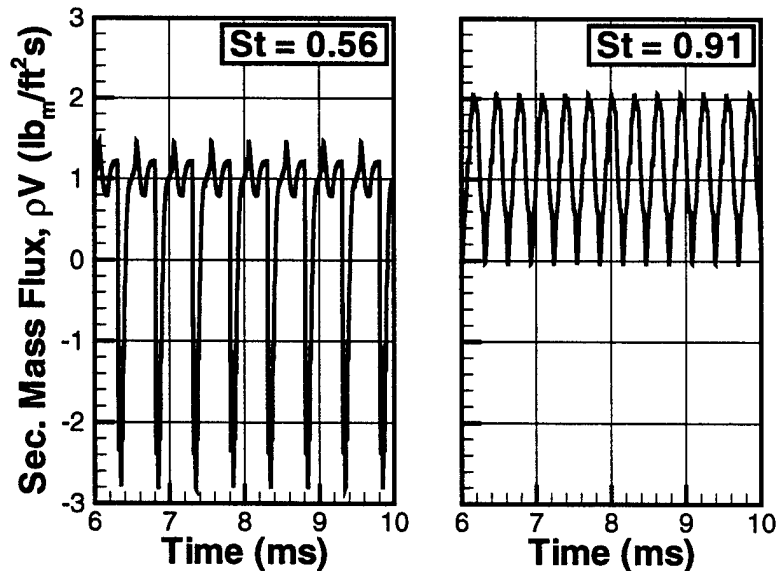
CFD simulations of the baseline ejector geometry were run at several Strouhal numbers to determine the effect of pulsing frequency on ejector performance. The unsteady primary jet was pulsed using a 50% duty-cycle square wave with a total pressure ratio of 3.0 when the jet is flowing. The primary-jet Mach number was varied from zero-flow conditions to a peak value of 1.0. The measure of pumping effectiveness was the ratio of time-averaged secondary (s) to primary (p) mass flow rate.

Figure 43 shows the effect of frequency on the pumping effectiveness of the pulsed ejector. Note that pulsing frequency has a pronounced effect on pumping effectiveness. The ejection ratio at a Strouhal No. of 0.91 is nearly 140% greater than at a Strouhal No. of 0.56. The entrainment of the secondary flow is dramatically effected by the phasing between the primary pulses and pressure rarefaction waves in the mixing tube.



**Figure 43: Effect of Pulsing Frequency on Pumping Effectiveness**

Note that when pulsed at a frequency close to a strong natural mode ( $St = 0.56$ ), the pumping effectiveness is relatively poor. Pulsing at a frequency that does not correspond to a strong natural mode ( $St = 0.91$ ) results in a much larger pumping effectiveness. Figure 44 shows time histories of secondary mass flux for  $St$  of 0.56 and 0.91. The  $St$  of 0.91 simulation has higher peak mass-flux levels and no reverse flow. However, the  $St$  of 0.56 solution has lower peak mass-flux levels and larger levels of reverse flow. It is much more effective to pulse at a frequency that is out of phase with the strong natural modes of the pulsed ejector.



**Figure 44: Secondary Mass Flux Time Histories**

### 5.3.3 Pulsed-Jet Ejector: Effect of Geometry

Time-accurate CFD simulations of two alternate pulsed ejector geometries were also conducted. These analyses were performed at several pulsing frequencies to determine the effects of changing the geometry on pumping effectiveness. The effects of varying mixing-tube length and mixing-tube area are shown in Figure 45. Doubling the mixing tube length relative to the baseline geometry had a small effect on maximum entrainment, increasing the peak pumping effectiveness by 5%. For this case, the frequency for peak entrainment increased 10%. Increasing mixing-tube length also reduced the sensitivity of entrainment to frequency, as seen by the broadening of the mass-flow-ratio characteristic in Figure 45. Doubling the mixing tube area had the effect of raising the peak ejection ratio by 24% while reducing the frequency at which the peak occurs by 8%.

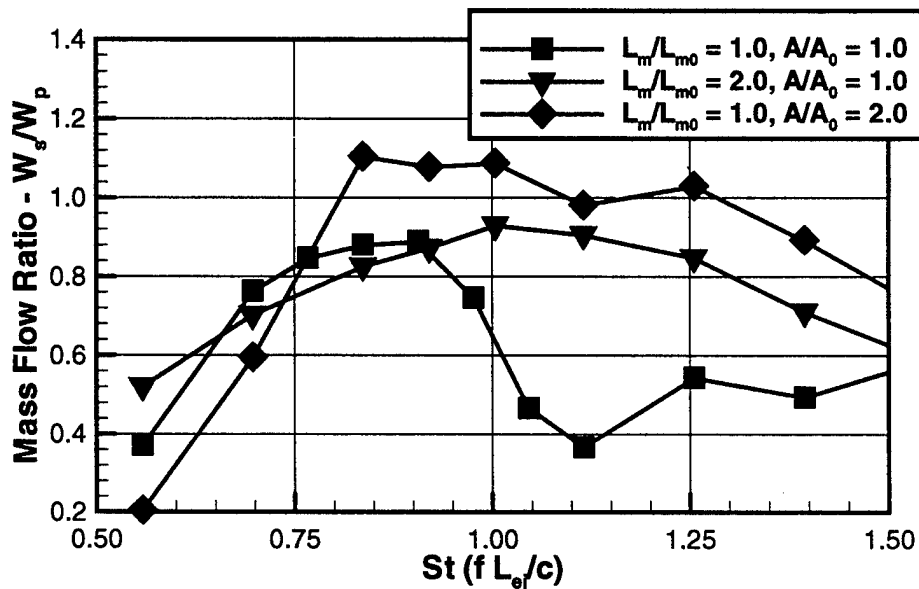
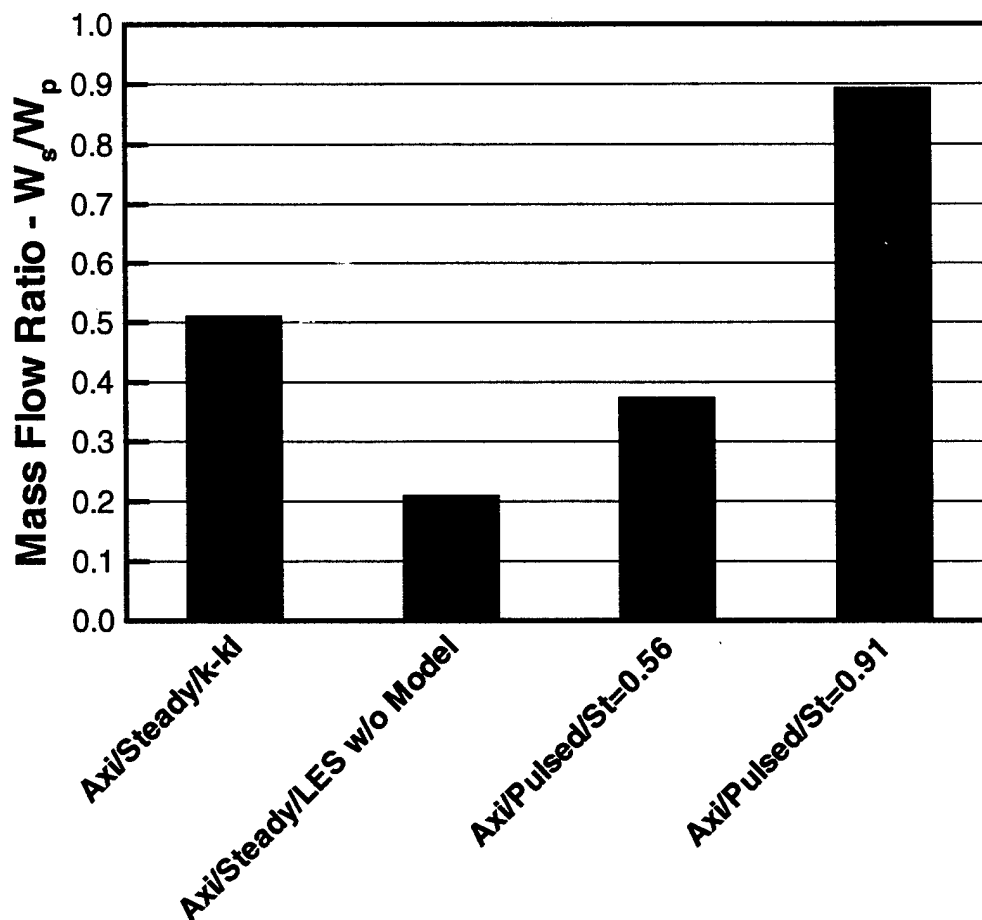


Figure 45: Effect of Pulsed-Ejector Geometry on Pumping Effectiveness

### 5.3.4 Comparison of Steady vs. Pulsed Ejector Performance

Steady-state ejector solutions were run using the same baseline geometry to compare the pumping performance with that of the pulsed ejector case. Axisymmetric steady-jet solutions were run steady state with the *k-kl* two-equation turbulence model and time-accurate LES with no model. The steady-jet solutions were run with a primary-jet total-pressure ratio of 3.0 and Mach number of 1.0. The axisymmetric pulsed-jet solutions were run as described in Section 5.3.2. The results of these simulations are shown in Figure 46 along with the pulsed ejection performance.



**Figure 46: Comparison of Steady and Unsteady Ejector Performance**

Note that the *k-kl* steady-jet solution has much better pumping performance than the LES no-model steady-jet solution. The *k-kl* solution was performed time-warped. The steady-jet, axisymmetric LES no-model solution may underestimate the mixing because it constrains the unsteady structures to be axisymmetric. Reynolds averaging treats the turbulent structure in the shear layer between the primary and secondary as mean Reynolds stresses. Reynolds averaging should predict steady ejector performance well.

To assess the accuracy of the steady-jet ejector solutions, a comparison was made to existing parametric ejector data. The data of DeLeo and Wood (1953) was extrapolated to the conditions evaluated here. The test data showed an ejector mass-flow ratio of approximately 0.5. This result is similar to the *k-kl* steady-jet solution.

Also shown in Figure 46 is the performance of two of the pulsed ejector simulations discussed in Section 5.3.2. The less effective ( $St = 0.56$ ) pulsed ejector simulation shows greater pumping effectiveness than the laminar steady-jet ejector, while not pumping as effectively as the *k-kl* simulation of the steady-jet ejector. The more effective pulsed-ejector simulation ( $St = 0.91$ ) exhibits much greater pumping effectiveness than either of the steady-jet ejector simulations. The  $St$  of 0.91 pulsed

ejector pumped the secondary stream 330% more effectively than the laminar steady-jet ejector simulation, and 75% more effectively than the *k-k* modeled steady-jet ejector simulation.

### 5.3.5 Comparison of 3-D and Axisymmetric CFD

As stated earlier, axisymmetric CFD simulations were used to characterize pulsed-ejector performance. Three-dimensional CFD simulations, which required up to 4 weeks of continuous calculation for a single time-accurate solution, were too costly given the number of simulations required by this investigation. However, a limited number of 3-D simulations (Figure 47) were performed to validate the performance trends observed in the axisymmetric results.

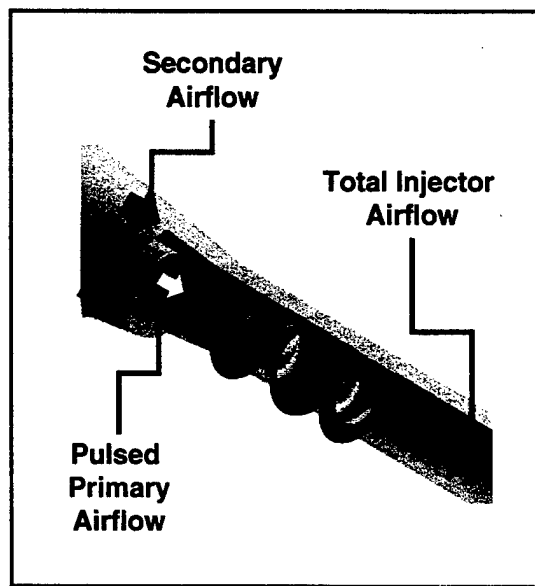


**Figure 47: 3-D Ejector CFD Solution**

Figure 48 shows a comparison of pumping effectiveness for steady and pulsed ejectors from axisymmetric and 3-D simulations. The 3-D steady-ejector simulation shows almost 50% more effectiveness than the axisymmetric simulation. This may be the result of three-dimensional mixing effects not modeled by an axisymmetric solution. This additional mixing enhances the entrainment of the secondary stream by the primary jet.

Results of the axisymmetric solution compared favorably to the 3-D pulsed-ejector solution in terms of pumping effectiveness (mass flow ratio).

In addition to the comparison between axisymmetric and 3-D simulations, the effects of grid-resolution were examined. For axisymmetric simulations, increasing the number of grid points from 5,953 to 23,207 resulted in a 10% change in the pumping performance of the pulsed ejector. For 3-D simulations, increasing the number of grid points from 240,072 to 618,312 resulted in a 10% change in pulsed-ejector performance.

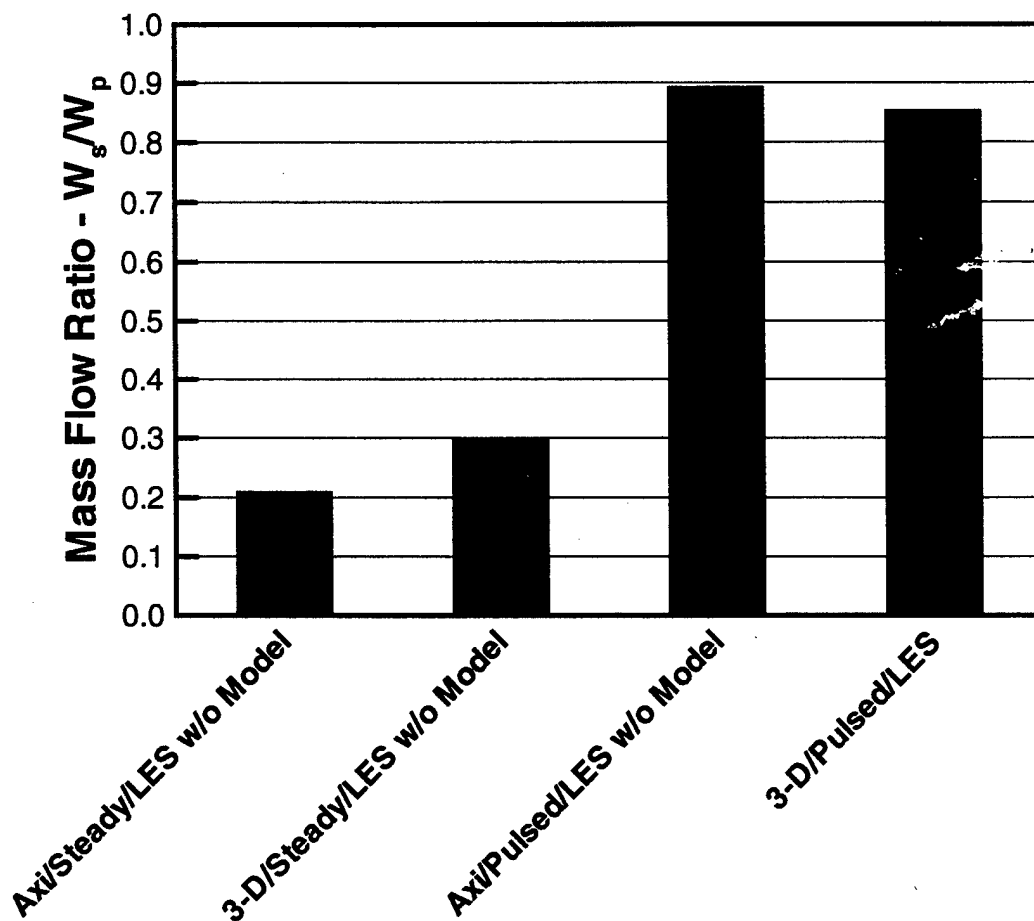
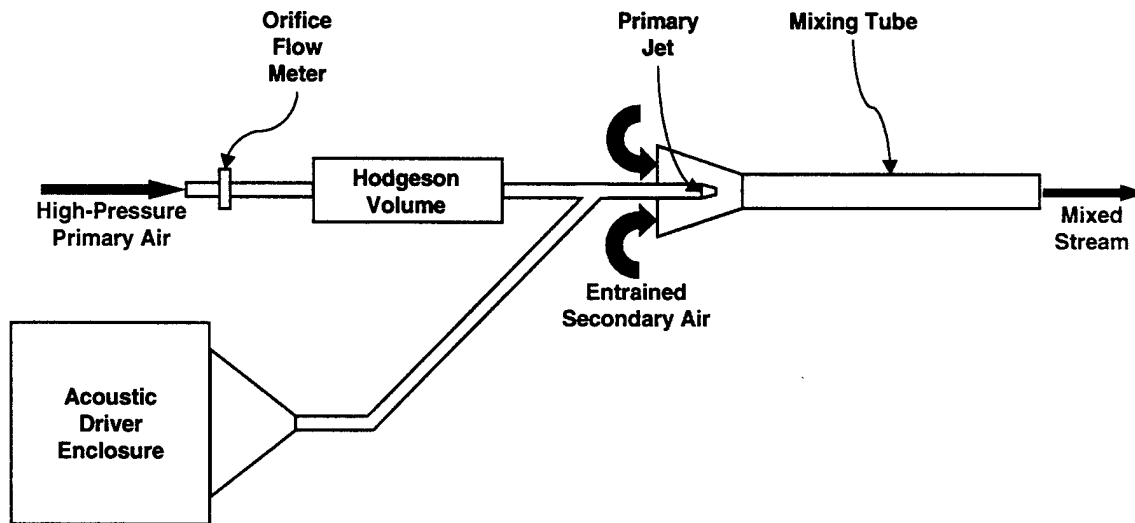


Figure 48: Comparison of Axisymmetric and 3-D CFD Simulations

### 5.4 Preliminary Experimental Investigation

A complementary experimental investigation of pulsed ejection has been performed using LM Independent Research and Development (IR&D) funds. This basic test was performed to provide a preliminary confirmation of the pulsed ejection technique presented in this research effort. The experimental effort was performed at the University of Calgary by Dr. Peter J. Vermeulen.



**Figure 49: Pulsed Ejector Test Apparatus Schematic**

Shown in Figure 49 is a schematic of the test apparatus. The primary jet was supplied by a high-pressure air source whose flow rate was measured via an orifice flow meter. The secondary air source was provided by ambient laboratory air. The mixed primary and secondary air exited the ejector into ambient air. The acoustic driver enclosure was a large volume to which an acoustic speaker had been mounted. When the speaker was powered, the enclosure superimposed an oscillatory, sinusoidal flow component (which had zero net mass flow) onto the steady flow supplied by the primary air source. The pulsed primary jet issued into a co-annular, ejector mixing tube. The Hodgeson volume served to isolate the orifice flow meter from the oscillatory nature of the pulsed jet.

Preliminary results were obtained for an ejector with a mixing tube to primary-jet area ratio of 3.0 and a mixing tube length to diameter ratio of 10. The primary jet mass flow was held constant for both steady and pulsed cases. The primary jet velocities were low enough that the ejector flow was considered incompressible. For a steady-jet ejector with a primary jet velocity of 20 meters per second, the pumping ratio  $W_s/W_p$  was 0.91. For a pulsed ejector with a mean primary jet velocity of 20 meters per second and a peak velocity of 66 meters per second,  $W_s/W_p$  was 2.44, an improvement in ejector pumping effectiveness of 170%.

These initial, experimental results provide a basic confirmation of the pulsed ejection technique.

### **5.5 Task Summary**

A basic characterization of the performance of pulsed ejectors has been conducted using CFD simulations. The Strouhal number of the natural mode of a steady-jet ejector scales with ejector length. Increases in mixing-tube area increase the Strouhal number of the natural mode. The pumping performance of pulsed ejectors was shown to have a strong sensitivity to pulsing frequency and mixing tube area, while mixing tube length had less effect. Pulsed ejectors pumped the secondary stream far more effectively than a steady-jet ejector with the same geometry.

## 6.0 A Simplified Model of Pulsed Ejection Using 1-D CFD

### 6.1 Motivation

The use of CFD for the analysis of pulsed-ejector performance is very expensive in terms of computational resources. For preliminary design of the ejector, it would be desirable to have a simpler analytical model of the ejector flow that can rapidly explore the design space. The results of the preliminary design study could then be verified with more expensive two and three-dimensional CFD analysis and experiment.

A model is presented here that attempts to accomplish this. The model exploits the predominant flow features in the ejector by using a quasi-one dimensional flow model. The approach is based on treating the primary and secondary flows as quasi-one dimensional flows that are coupled with a simplified viscous mixing model. The model can be run on a workstation in a matter of minutes, where a full 3-D CFD solution takes several weeks on a multi-processor supercomputer.

The intent of this simplified model is to derive representative steady-state boundary conditions for an injector that is supplied by air from a pulsed ejector. Such boundary conditions can be used in the analysis of fluidic nozzle control concepts.

### 6.2 Governing Equations

The following assumptions are made in this model:

- Primary and secondary streams are treated as quasi-1D unsteady flows
- The pressure is constant normal to the flow in the mixing region, i.e.

$$P(x, t)_{primary} = P(x, t)_{secondary}$$

- The stream surface between the primary and secondary streams is allowed to vary to allow the primary and secondary pressures to balance to satisfy assumption 2
- A viscous shear model is applied at the interface of the primary and secondary streams to simulate momentum transfer from the primary to secondary flow

Assumption (3) requires that the area for the primary and secondary vary as function of both space and time, i.e.

$$A_{ejector}(x) = A_{primary}(x, t) + A_{secondary}(x, t)$$

although the total area only varies with space (x). The Euler equations for quasi 1-D flow with time varying area are

$$\frac{\partial}{\partial t}(\rho A) + \frac{\partial}{\partial x}(\rho u A) = 0$$

$$\frac{\partial}{\partial t}(\rho u A) + \frac{\partial}{\partial x}((\rho u^2 + p)A) = p \frac{\partial A}{\partial x}$$

$$\frac{\partial}{\partial t}(\rho EA) + \frac{\partial}{\partial x} \left( \rho u \left( E + \frac{p}{\rho} \right) A \right) = -p \frac{\partial A}{\partial t}$$

$\rho$  and  $u$  are the flow density and velocity, respectively and  $E = e + \frac{u^2}{2}$  is the total energy per unit mass. The pressure,  $p$ , is related to the internal energy per unit mass,  $e$ , by the perfect gas equation of state  $p = (\gamma - 1)\rho e$ , where  $\gamma$  is the ratio of specific heats.

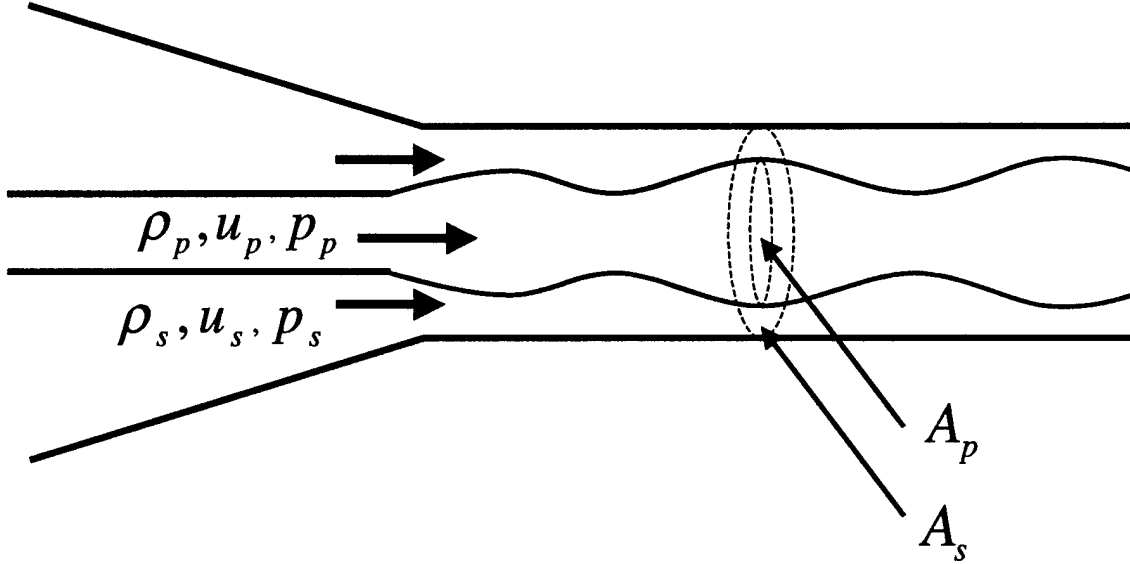


**Figure 50: Schematic of Ejector Geometry**

Using the assumptions made above, the flow equations for the ejector can be written as two sets of 1-D, coupled equations for the primary stream

$$\frac{\partial}{\partial t}(\bar{\rho}_p) + \frac{\partial}{\partial x}(\bar{\rho}_p u_p) = 0$$

$$\frac{\partial}{\partial t}(\bar{\rho}_p u_p) + \frac{\partial}{\partial x}(\bar{\rho}_p u_p^2 + \bar{p}_p) = \left( \frac{\bar{p}_p + \bar{p}_s}{A} \right) \frac{\partial A_p}{\partial x} - V_M$$

$$\frac{\partial}{\partial t} \left( \frac{\bar{p}_p}{\gamma - 1} + \frac{\bar{\rho}_p u_p^2}{2} \right) + \frac{\partial}{\partial x} \left( u_p \left( \frac{\bar{p}_p}{\gamma - 1} + \frac{\bar{\rho}_p u_p^2}{2} \right) \right) = -\frac{A_s}{A} \frac{\partial \bar{p}_p}{\partial t} + \frac{A_p}{A} \frac{\partial \bar{p}_s}{\partial t} - V_E$$

and the secondary stream

$$\frac{\partial}{\partial t}(\bar{\rho}_s) + \frac{\partial}{\partial x}(\bar{\rho}_s u_s) = 0$$

$$\frac{\partial}{\partial t}(\bar{\rho}_s u_s) + \frac{\partial}{\partial x}(\bar{\rho}_s u_s^2 + \bar{p}_s) = \left( \frac{\bar{p}_p + \bar{p}_s}{A} \right) \frac{\partial A_s}{\partial x} + V_M$$

$$\frac{\partial}{\partial t} \left( \frac{\bar{p}_s}{\gamma-1} + \frac{\bar{\rho}_s u_s^2}{2} \right) + \frac{\partial}{\partial x} \left( u_s \left( \frac{\bar{p}_s}{\gamma-1} + \frac{\bar{\rho}_s u_s^2}{2} \right) \right) = -\frac{A_p}{A} \frac{\partial \bar{p}_s}{\partial t} + \frac{A_s}{A} \frac{\partial \bar{p}_p}{\partial t} + V_E$$

The subscripts  $p$  and  $s$  denote primary and secondary flow properties, respectively (see Figure 50).  $V_M$  and  $V_E$  are viscous mixing terms for the momentum and energy equations, respectively, and are described below. The primary and secondary areas are related to the ejector area  $A$  by

$$A(x) = A_p(x, t) + A_s(x, t)$$

The pressure and density in these equations are scaled by their respective areas:

$$\bar{p}_p = A_p p, \quad \bar{p}_s = A_s p$$

and

$$\bar{\rho}_p = A_p \rho_p, \quad \bar{\rho}_s = A_s \rho_s$$

The use of area scaled quantities puts the convective terms in pure one dimensional form, allowing easy application of existing numerical flux schemes. Note that the unscaled primary and secondary pressures are equal.

### 6.3 Viscous Mixing Model

The viscous mixing terms in the momentum and energy equations are defined as follows in terms of a turbulent shear stress  $\tau$  and heat diffusion  $q$  applied to the wetted interface area between the primary and secondary flows:

$$V_M = A_i \tau$$

$$V_E = A_i \left( \frac{1}{2} (u_p + u_s) \tau + q \right)$$

$A_i$  is the wetted interface area factor (which, in the one-dimensional differential form of the equations, has the dimensions of length). If the wetted-interface area is assumed to be axisymmetric, then  $A_i = 2\sqrt{\pi A_p}$ .

The form of  $\tau$  is based on algebraic stress models for axisymmetric developing and fully developed jet flow. For details on these models see Schlichting (1968) and White (1974). Based on these models, the shear stress is assumed to be proportional to the velocity difference between the primary and secondary flows

$$\tau = \mu_t (u_p - u_s) / l$$

A length scale,  $l$ , represents the thickness of the shear layer.

The turbulent viscosity  $\mu_t$  is defined as

$$\mu_t = \frac{c}{2} (\rho_p + \rho_s) |u_p - u_s| l$$

where  $c$  is an empirical constant. Note that when the turbulent viscosity is substituted into the equation for  $\tau$ ,  $\tau$  becomes independent of  $l$ . Similarly, the heat diffusion term is assumed to be proportional to the temperature difference between the secondary and primary flows

$$q = k_t (T_p - T_s) / l$$

$k_t$  is related to  $\mu_t$  through a turbulent Prandtl number  $Pr_t = 0.9$  and specific heat at constant pressure  $c_p$

$$k_t = \frac{\mu_t c_p}{Pr_t}$$

The empirical constant  $c$  is to be determined from calibration with CFD and experimental results. Based on experimental evidence documented in Schlichting (1968) and White (1974) an initial estimate of  $c = 0.02$  has been made.

#### 6.4 Numerical Approach

The convective terms in the primary and secondary flow equations are discretized using the upwind flux difference procedure of Roe (1981) and third order MUSCL (1995) extrapolation. The source term  $pA_x$  in the momentum equations is approximated using second order central differences.

The discrete equations are integrated in time using an explicit second order Runge-Kutta algorithm. Being an explicit algorithm, the numerical time step is CFL limited. Stable operation of the code with CFL numbers of 0.8 has been achieved, typically a CFL of 0.4 is used in normal operation.

#### 6.5 Preliminary Results and Validation

Solutions using the model described above have been obtained for a simplified ejector geometry. The primary and secondary tubes are of constant area with an area ratio  $A_s / A_p = 2.34$ , with the diameters of the primary jet exit and mixing tube being 0.127 inches and 0.231 inches, respectively. The length of the mixing tube was 2.45 inches and the overall length of the ejector was 2.98 inches.

The total pressure and temperature were specified as boundary conditions for the inlet of the primary and secondary flows. The primary-jet total pressure and temperature were 16.78 psia and 527 Rankine, while the secondary jet conditions were 16.46 psia and 527 Rankine. A static pressure of 16.53 psia was specified as a downstream boundary condition, giving a slight adverse pressure gradient with respect to the secondary inflow conditions.

Two solutions are presented here using the geometry and boundary conditions described above. The first was run with the turbulent viscosity coefficient  $c$  set to 0.02, which was estimated from the literature as was described above. The model was integrated in time until it reached a steady state solution. Plots of the time history of the primary and secondary mass flux and Mach number at the ejector exit are given in Figure 51.

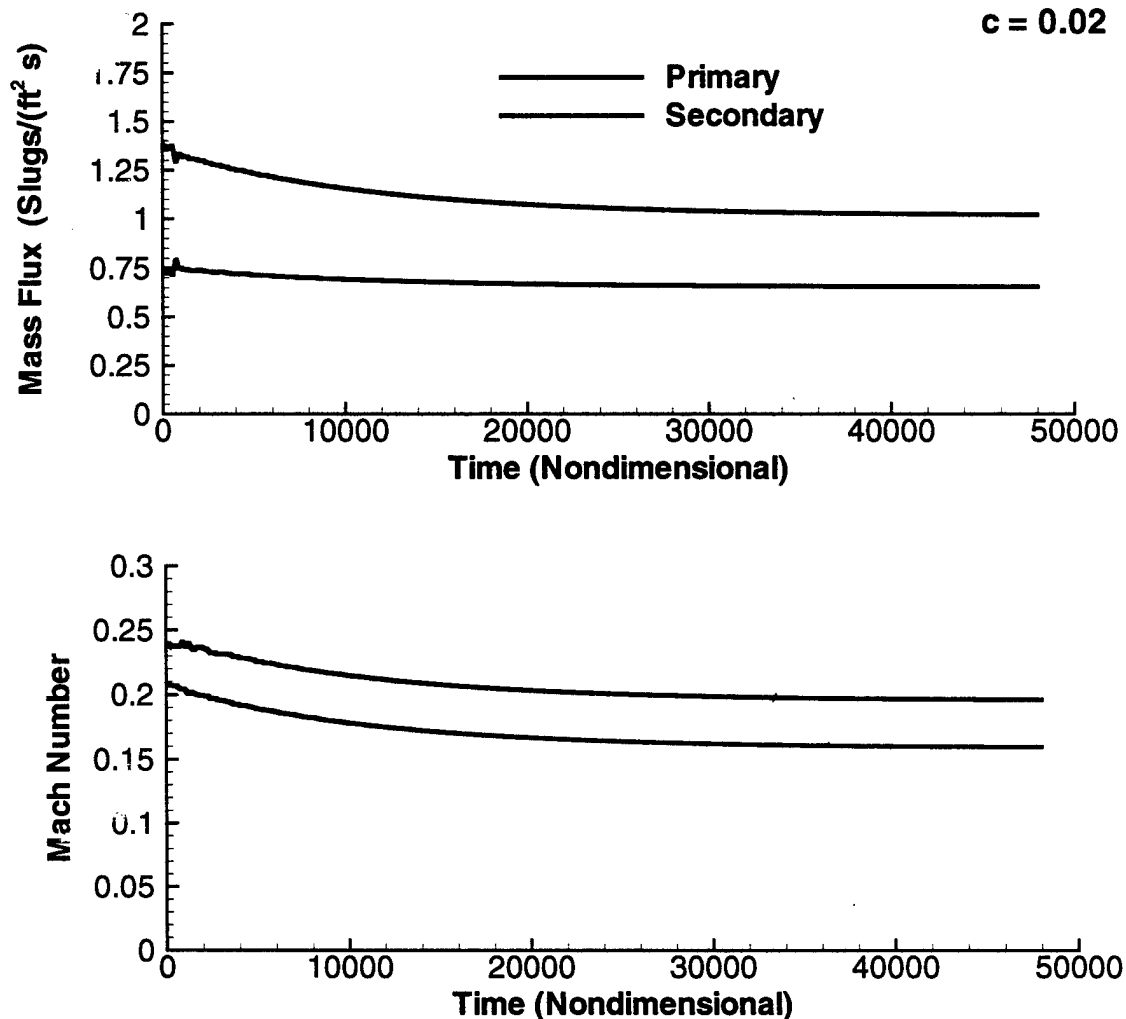


**Figure 51: Mass flux and Mach number as a function of time for  $c=0.02$**

As can be seen in the figure, the primary jet exit Mach number stabilizes at 0.2. Entrainment of the secondary flow is evident with a secondary flow exit Mach number of 0.16. The ratio of secondary to primary mass-flux ratio is 1.55, which seems to be high based on previous CFD results.

A second case was attempted with the turbulent viscosity coefficient  $c$  set to 0.002 in order to see if the entrainment of the secondary flow could be reduced. The results are shown in Figure 52. While the entrained secondary flow is reduced substantially, the code encountered an instability as it approached a steady state solution.

The instability in this result has been encountered when running the model under a variety of conditions, and is exacerbated when larger pressure ratios are specified. The stability of the model also appears to be sensitive to the specification of initial conditions. It is not sensitive to the local CFL number as long as the  $CFL < 0.8$ , which is a known limitation imposed by the explicit Runge-Kutta algorithm. The instability seems to be related to the behavior of the variation of the flow areas  $A_p$  and  $A_s$ , and the ultimate cause of failure in the model occurs when either  $A_p$  or  $A_s$  is driven negative.

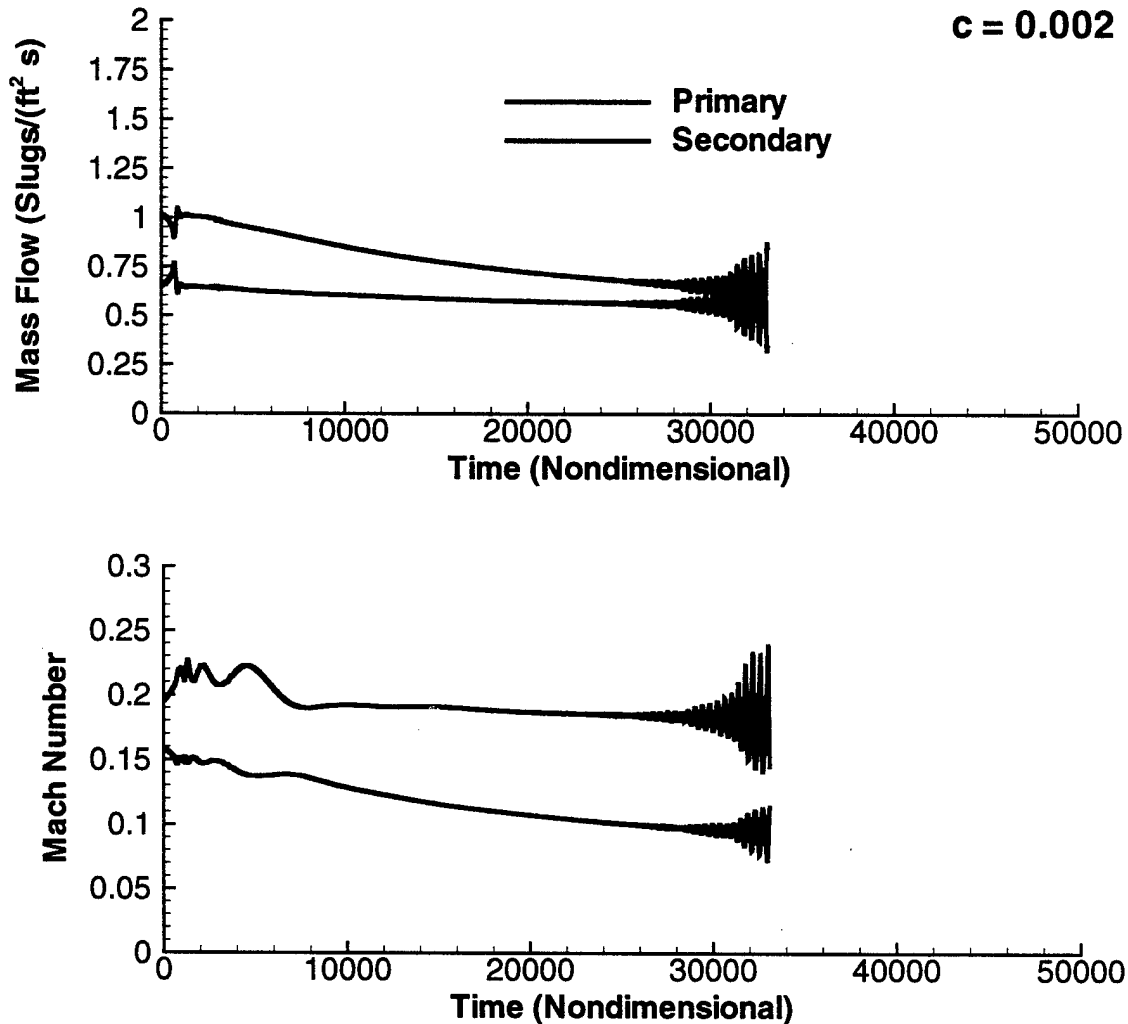


**Figure 52: Mass flux and Mach number as a function of time for  $c=0.002$**

Currently, the cause of the instability is not known. It is felt that the assumptions of quasi 1-D flow and constant pressure between primary and secondary flow may not be valid near the primary-jet exit due to large pressure variations encountered there. Alternative strategies should be considered in future work that incorporate a partial relaxation of the constant pressure assumption in order to prevent the computed areas from becoming negative.

## **6.6 Task Summary**

A quasi 1-D model has been developed for predicting behavior of pulsed-jet ejectors. The model is based on two coupled quasi 1-D flows modeling the primary and entrained secondary flows. The two flows are coupled by allowing the interface between them to vary in order to balance the pressure. In addition an algebraic viscous mixing model is incorporated that transfers momentum and energy from the primary to the secondary stream to simulate entrainment.

Current validation efforts have shown that the model in its present form suffers from an instability that has prevented calibration of the model to practical ejector flows. The nature of the instability seems to be related to the violation of the assumptions of quasi 1-D flow and the equality of the primary and secondary pressures. Strategies to address this instability need to be investigated to increase the robustness of the model.

## 7.0 Overall Project Conclusions

Computational fluid dynamics (CFD) and experimental methods were used to investigate two unsteady injection techniques for increasing the penetration and blockage of an injected stream in a confined, expanding crossflow. The motivation of this research effort was to improve the efficacy of fluidic nozzle control techniques, which rely on the use of an injected stream to produce a localized obstruction to the crossflow.

A systematic study comparing unsteady CFD analysis to experimental data has been performed to determine parametric requirements to accurately simulate pulsed-injector jets injecting into a crossflow. The effects of grid resolution, turbulence modeling, and numerical discretization were examined. Considerably better grid resolution was required for pulsed-injector jet simulations as compared to a steady-injector jet of the same mass flow. The time averaging of the two-equation model in the steady-injector jet simulation smoothes spatial gradients reducing resolution requirements. The RANS-based turbulence models were not adequate for pulsed-injector jet simulations, however, since the time-averaging process removes relevant features of the unsteady flow. The accuracy of the pulsed-injector jet simulations was very sensitive to treatment of the upwind discretization. In particular, flux limiting methods must be carefully selected since the flux limiter can be highly diffusive. The use of third-order discretization of the convective fluxes improved the prediction of injector-jet penetration height over second-order discretization.

An investigation of pulsed injection into a confined, expanding crossflow was conducted using CFD simulations. Results of these simulations revealed that pulsing generally produced a measured increase in injector-jet stream penetration and diameter over that of a steady injector. The vortex-ring diameter generally increased (relative to the exit diameter) in the near field region, as a likely result of the rapid entrainment associated with the regions of high vorticity and shear near the rings. The injector-jet blockage was relatively unaffected by pulsing frequency. Increasing time-averaged pulsing Mach number in the case of pulsing produced gains in injector-jet penetration and blockage over that of steady injection. Results suggested that an increase in blockage over that of the steady case was primarily related to an increase in the time-averaged momentum flux. Pronounced entrainment effects may confound the relationship between injector-jet penetration and blockage, for the case of pulsing. Increasing the number of injector holes across the nozzle span decreased penetration, but increased blockage for the cases of steady and pulsed injection. Maximum injector-jet penetration and blockage was obtained when the injector was angled upstream into the crossflow at 45 degrees. Gains in penetration using pulsing were smaller than observed in previous incompressible studies.

The findings in this CFD-based investigation have several implications for defining requirements of pulsing actuators to be used for increasing injector-jet penetration and blockage in the transonic flow regime. To achieve an increase in near-field penetration, actuators must be able to operate at very high frequencies. In this investigation, a  $St$  of 0.3 achieved peak penetration of the injector jet. For a full-scale

configuration, this translates to roughly 1500 Hz and as much as 15 kHz for a model-scale configuration. To achieve an increase in blockage, actuators must be able to produce peak exit Mach numbers greater than 1.0 during pulsing, while modulating the flow as much as possible during the remaining portion of the pulsing period. The actuators should be integrated in a distributed fashion to produce pulsing across an array of injector holes across the span of the flowpath. The injector exit should be directed upstream to oppose the crossflow. This investigation has demonstrated the feasibility of using pulsing to increase injector-jet penetration and blockage in a transonic crossflow. However, limitations on the frequency and exit velocity capability of current pulsing actuators will likely leave further experimental investigations of this technique to future studies.

Two pulsing actuators were experimentally evaluated for modulating an injected stream issuing into a nozzle crossflow. Bench test measurements on the ASFDV revealed that the flow at the device exit did not display a fully modulated square velocity waveform, which was considered ideal for pulsed injection. Test results using the ASFDV to pulse the injected flow in the nozzle revealed no discernable gain in blockage over that of a steady injector case at a comparable mass flow rate. Unsteady pressure measurements in the injector plenum showed a relatively weak and quasi-periodic waveform. The stability of the measured ASFDV waveform was found to be sensitive to differences in backpressure of the two output legs. It also is believed that the capacitance of the flow passages in the valve and injector are partly responsible for the relatively weak output waveform. Unsteady pressure measurements in the injector plenum using the AFPG showed a relatively high frequency capability ( $\sim$ kHz), but the output waveform at the injector was also relatively weak and non-periodic. PIV measurements of the nozzle flow field revealed a small increase in injector-jet penetration and spreading using the AFPG to pulse the injected stream, however, no discernable vortex ring structures were observed.

A basic characterization of the performance of pulsed ejectors has been conducted using CFD simulations. The Strouhal number of the natural mode of a steady-jet ejector scales with ejector length. Increases in mixing-tube area increase the Strouhal number of the natural mode. The pumping performance of pulsed ejectors was shown to have a strong sensitivity to pulsing frequency and mixing tube area, while mixing tube length had less effect. Pulsed ejectors pumped the secondary stream far more effectively than a steady-jet ejector with the same geometry.

A quasi 1-D model has been developed for predicting behavior of pulsed-jet ejectors. The model is based on two coupled quasi 1-D flows modeling the primary and entrained secondary flows. The two flows are coupled by allowing the interface between them to vary in order to balance the pressure. In addition an algebraic viscous mixing model is incorporated that transfers momentum and energy from the primary to the secondary stream to simulate entrainment. Current validation efforts have shown that the model in its present form suffers from an instability that has prevented calibration of the model to ejector flows of interest to this research project.

## 8.0 Acknowledgements

This work was sponsored by the Air Force Office of Scientific Research, USAF, under contract number F49620-98-C-0016. The AFOSR program manager was Dr. Thomas J. Beutner. The views and conclusions contained herein are those of the authors and should not be interpreted as necessarily representing the official policies or endorsements, either expressed or implied, of the Air Force Office of Scientific Research or the U.S. Government. The research team gratefully acknowledges the significant contributions of the following individuals: Dr. Thomas J. Beutner and Dr. Steven H. Walker, AFOSR, for their support of CFD methods for flow control research; Dr. Peter J. Vermeulen, University of Calgary, for his thorough insight and consulting on pulsed injection; Mr. C.F. Chin for making his experimental data, with interpretations, fully available; and Mr. John L. Richey, LM Aero, for assistance with test article fabrication.

## 9.0 Recommendations for Future Work

The use of time-accurate CFD shows potential for analysis and design of fluidic flow control techniques that are fundamentally unsteady such as the use of pulsed injectors and ejectors studied in this work. In order to allow accurate and efficient application of CFD to the research and development of active flow control systems, two subjects need to be addressed to a greater extent - numerical solution accuracy and computational cost.

The numerical approach used in unsteady, compressible CFD analysis needs further study. Unsteady flows have more stringent accuracy requirements than their steady counterparts, and higher order numerical discretization is required to obtain this accuracy. True higher-order-accurate methods are difficult to apply in compressible flows, due to the presence of flow discontinuities such as shocks. In an upwind discretization, these discontinuities are frequently resolved numerically with the use of flux limiters. Limiters reduce the accuracy of the discretization to first order at the location of a discontinuity to avoid spurious numerical oscillations. Many limiting strategies such as the MINMOD limiter reduce to first order accuracy at all local extrema in the flow. Since unsteady flows with mixing layers are rich in local extrema, the accuracy of a numerical solution can be seriously compromised. Future work on compressible unsteady flows needs to address the deficiencies of these numerical devices and investigate improved methods for handling flow discontinuities.

Even with the rapidly increasing power of computers, the computational cost of unsteady CFD analyses prohibits their use in for rapid design. More approaches to reduce this cost need to be investigated. An approach investigated in this work, specifically for ejector flows, has been to develop a one-dimensional mixing model of the ejector. The purpose of the model is to provide an expedient means for exploring the design space, using more thorough 3-D CFD to validate particular point designs. Currently the model as devised has instabilities that need to be addressed. A relaxation of some of the assumptions made in developing the model and reformulation of the governing equations based on the modified assumptions may help to remove these instabilities. Upon successful completion of the model development, calibration of the model against CFD and experimental data would be needed.

Other approaches to reduce computational cost may be fruitful. In this work it has been shown that conventional RANS derived turbulence models are inadequate for accurately predicting unsteady phenomena in pulsed injector jets. However, new models based on a hybrid approach are being developed that combine large eddy simulation and transport equation based models. The intent of these models is to reduce the range of length scales that need to be resolved so that the size of the numerical problem can be reduced substantially. These models need to be applied to problems like the pulsed injectors and ejectors studied here to determine their suitability and potential cost savings. This approach would allow the computational power to be focused on the interaction between larger turbulent and unsteady scales of motion instead of the small near wall

scales, which are closer to equilibrium and easier to model. In the case of the geometrically axisymmetric pulsed ejector, for example, this work shows differences in the axisymmetric and 3D numerical solutions that may be attributed to the effects of the three dimensional nature of turbulence. A properly developed hybrid model may be able to model the all of the three dimensionality of the turbulence, allowing the numerical problem to be solved exploiting the axisymmetric geometry.

More research is required into pulsing actuators, which provide sufficiently large modulation and frequency of an injected flow in the compressible regime. Previous efforts have addressed pulsing actuators for low-speed applications. In the present study, a preliminary evaluation of two actuators revealed many challenges associated with the use of such devices for higher-speed applications. From the CFD simulations described in sections three and five, a set of basic requirements have been developed for defining and evaluation actuators in future studies. Future research should also address the manifold system required for integrating the actuators into an injection system using detailed CFD analyses. One possible concept for a future pulsing actuator system is one that periodically varies the temperature, rather than the pressure. Compressible studies showed that pulsing the pressure produced greater losses by increasing the injector-jet shock strength. By transiently increasing the temperature, the sonic velocity can be increased to boost injector-jet velocity and momentum without increasing the Mach number.

## 10.0 References

1. Bender, E., Miller, D., Smith, B., Yagle, P., Vermeulen, P., Walker, S., 2000, "Simulation of Pulsed Injection in a Crossflow Using 3-D Unsteady CFD," AIAA No. 2000-2318.
2. Broadwell, J.E. and Breidenthal, R.E., 1984, "Structure and Mixing of a Transverse Jet in Incompressible Flow," J. Fluid Mechanics, Vol. 148, pp. 405-412.
3. Blaszkak, J.J. and Fahrenholz, F.E., 1960, "Rocket Thrust Control by Gas Injection," Massachusetts Institute of Technology, Naval Supersonic Laboratory, Technical Report 430.
4. Catt, J.A., Miller, D.N. and Giuliano, V.J., 1995, "A Static Investigation of Fixed-Geometry Nozzles Using Fluidic Throat-Area Control," AIAA, Paper No. 95-2604.
5. Catt, J.A., Miller, D.N., and Walker, S.H., 1997, "Extending Flow Control of Fixed Nozzles: A Static Investigation of Assisted Reinjection," ASME, Paper No. FEDSM97-3230.
6. Chiarelli, C., Johnsen, R.K., and Shieh, C.F., 1993, "Fluidic Scale Model Multi-Plane Thrust Vector Control Test Results," AIAA 93-2433.
7. DeLeo, R.V. and Wood, R.D., 1953, "An Experimental Investigation of the Use of Hot-Gas Ejectors for Boundary Layer Removal," Part II, WADC TR 52-128.
8. Eroglu, A. and Breidenthal, R.E., 1991, "Effects of Periodic Disturbances on Structure and Flame Length of a Jet in a Crossflow," AIAA, Paper No. 91-0317.
9. Federspiel, J. et al., 1995, "Fluidic Control of Nozzle Flow - Some Performance Measurements," AIAA, Paper No. 95-2605.
10. Fric, T.F. and Roshko, A., 1989, "Structure in the Near Field of the Transverse Jet," Seventh International Symposium on Turbulent Shear Flows, Stanford Univ., pp. 225-237.
11. Gerlinger, P. et al., 1996 "Numerical Simulation of Mixing for Turbulent Slot Injection," AIAA Journal, Vol. 34, No. 1.
12. Gridley, M.C. and Walker, S.H., 1996, "Inlet and Nozzle Technology for 21st Century Aircraft," ASME, Paper No. 96-GT-244.
13. Gruber, M.R. et al., 1995, "Mixing and Penetration Studies of Sonic Jets in a Mach 2 Freestream," Journal of Propulsion and Power, Vol. 11, No. 2.
14. Gunter, F.L. and Fahrenholz, F.E., 1961, "Final Report on a Study of Rocket Thrust Control by Gas Injection," Massachusetts Institute of Technology, Naval Supersonic Laboratory, Technical Report 448.
15. Holdeman, J.D. and Walker, R.E., 1977, "Mixing of a Row of Jets with a Confined Crossflow," AIAA Journal, Vol. 15, No. 2, February, 1977.
16. Kral, L.D., Donovan, J.F., Cain, A.B., and Cary, A.W., "Numerical Simulation of Synthetic Jet Actuators," AIAA 97-1824.
17. McAulay, J.E., 1959, "Cold-Air Investigation of Three Variable-Throat-Area Convergent-Divergent Nozzles," NASA TM X-42.
18. Miller, D.N., Bender, E.E., Smith, B.R., Yagle, P.J., and Vakili, A.D., 1999, "Pulsed Injection for Nozzle Throat Area Control," Tech. Rep. AFOSR No. F49620-98-C-0016
19. Miller, D., Yagle, P., Hamstra, J., 1999, "Fluidic Throat Skewing for Thrust Vectoring in Fixed-Geometry Nozzles," AIAA No. 99-0365.
20. Miller, D.N. and Catt J.A., 1995, "Conceptual Development of Fixed-Geometry Nozzles Using Fluidic Throat-Area Control," AIAA, Paper No. 95-2603.
21. Miller, D.N., Catt J.A., and Walker, S.H., 1997, "Extending Flow Control of Fixed Nozzles Through Systematic Design: Introducing Assisted Reinjection," ASME, Paper No. FEDSM97-3680.

22. Okong'o, N. and Knight, D.D., 1998, "Accurate Three Dimensional Unsteady Flow Simulation Using Unstructured Grids," AIAA 98-0787.
23. Papamoschou, D. and Roshko, A., 1986, "Observations of Supersonic Free Shear Layers," AIAA, Paper No. 86-0162.
24. Reed, C.L., 1998, "Implementation of Low Speed Preconditioning in the Splitflow Code," AIAA 97-1867.
25. Rizzeta, D.P., Visbal, M.R. and Stanek, M.J., 1998, "Numerical Investigation of Synthetic Jet Flowfields," AIAA Paper No. 98-2910.
26. Roe, P.L., 1981, "Approximate Riemann Solvers," *J. of Comp. Physics*, Vol. 43, pp. 357-372.
27. Roe, P.L., 1981, "Some Contributions to the Modeling of Discontinuous Flows," *Proceedings of the SIAM/SMS Seminar*.
28. Schlichting, H., "Boundary Layer Theory," 3<sup>rd</sup> Ed. McGraw Hill, New York, 1968.
29. Smagorinski, J., 1963, "General Circulation Experiments with the Primitive Equations," *Mon. Weather Rev.*, Vol. 91, pp. 99-164.
30. Smith, B.R., 1990, "The k-kl Turbulence Model and Wall Layer Model for Compressible Flows," AIAA 90-1483.
31. Stone, H.L., 1968, "Iterative Solution of Implicit Approximations of Multidimensional Partial Differential Equations," *SIAM J. of Numer. Anal.*, Vol. 5 1968, pp. 530-538.
32. Strykowski, P. And Krothapalli, A., 1994, "Thrust Vector Control of Rectangular Jets Using Counter Flow," AFOSR Contractors Meeting Abstract.
33. Sweby, P.K., 1984, "High Resolution Schemes Using Flux Limiters for Hyperbolic Conservation Laws," *SIAM J. Numer. Anal.*, Vol. 21, pp. 995-1101.
34. Terrier, D.A. et al., 1995, "Vehicle Integration Technology Planning Study," Final Report, Lockheed Martin, No. FZM-8381.
35. Vakili, A., Sauerwein, S., Miller, D., 1999, "Pulsed Injection Applied to Nozzle Internal Flow Control," AIAA No. 99-1002.
36. Vakili, A.D., Chang, Y.K. and Wu, J.M., 1991, "Vortex Rings in Uniform Crossflow," AIAA, Paper No. 91-0522.
37. Vakili, A.D., Wu, J.M., Chang, Y.K. and Yu, F.M., 1990, "Pulsed Jets in Crossflow," *Int'l Symposium on Nonsteady Fluid Dynamics, FED-Vol. 92*.
38. van Leer, B., 1976, "MUSCL, a New Approach to Numerical Gas Dynamics," *Computing in Plasma Physics and Astrophysics*, Max-Planck-Institut fur Plasma Physik, Garching, Germany, April, 1976.
39. Vermeulen, P.J., Chin, C.F., and Yu, W.K., 1990, "Mixing of an Acoustically Pulsed Air Jet within a Confined Cross Flow," *J. Propulsion*, Vol. 6, No. 6, Nov. 1990, pp. 777-783.
40. Vermeulen, P.J., and Ramesh, V., 1997, "NOx Measurements for Combustor with Acoustically Controlled Primary Zone," *J. of Engineering for Gas Turbines and Power*, Vol. 119, No. 6, Jul. 1997, pp. 559-565.
41. Vermeulen, P.J. et al., 1988, "An Experimental Study of Mixing Behavior of an Acoustically Pulsed Air Jet with a Confined Crossflow," AIAA, No. 88-3296.
42. Vermeulen, P.J. et al., 1986, "Measurement of Entrainment by Acoustically Pulsed Axisymmetric Air Jets," *Journal of Engr. for Gas Turbines and Power*, Vol. 108.
43. Vermeulen, P.J. et al., 1996, "NOx Measurements for Combustor with Acoustically Controlled Primary Zone," ASME, Paper No. 96-GT-129.
44. Vermeulen, P.J., et al., 1993, "Temperature and Combustion Analysis of Combustor with Acoustically Controlled Primary Zone Air-Jet Mixing," AGARD Conference Proceedings 536, Fuels and Combustion Technology.
45. Walker, S., 1997, "Lessons Learned in the Development of a National Program," AIAA 97-334.
46. Wernet, M.P. and Bright, M., 'Dissection of Surge in a High Speed Centrifugal

- Compressor Using Digital PIV", 1999, AIAA-99-0270
47. White, F.M., "Viscous Fluid Flow," McGraw Hill, New York, 1974.
  48. Wing, D.J., 1994, "Static Investigation of Two Fluidic Thrust-Vectoring Concepts on a Two-Dimensional C-D Nozzle," NASA TM 4574.
  49. Wu, J.M., Vakili, A.D., and Yu, F.M., 1988, "Investigation of the Interacting Flow of Nonsymmetric Jets in a Crossflow," AIAA Journal, Vol. 26, No. 8.
  50. Yagle, P., Miller, D., Ginn, K., Hamstra, J., 2000, "Demonstration of Fluidic Throat Skewing for Thrust Vectoring in Structurally Fixed Nozzles," ASME No. 2000-GT-0013.

## 11.0 Appendix: Test Data Plots

### 11.1 Publications

"Simulation of Pulsed Injection in a Cross Flow Using 3-D Unsteady CFD," Bender, E., Miller, D., Smith, B., Yagle, P., Vermeulen, P., Walker, S., 2000, AIAA No. 2000-2318.

"Pulsed Injection Applied to Nozzle Internal Flow Control," Vakili, A., Sauerwein, S., Miller, D., 1999, AIAA No. 99-1002.

"Fluidic Throat Skewing for Thrust Vectoring in Fixed-Geometry Nozzles," Miller, D., Yagle, P., Hamstra, J., 1999, AIAA No. 99-0365.

### 11.2 Awards Received

AIAA Best Paper Award, 35<sup>th</sup> Joint Propulsion Conference, Los Angeles, CA. Title: "Fluidic Throat Skewing for Thrust Vectoring in Fixed-Geometry Nozzles"

Invention Disclosure Award, Lockheed Martin Corporation.

AIAA Poster Award, Art of Flow Control Session, Fluids 2000 Conference, Denver, CO.

### 11.3 Transitions

The CFD methodology and associated validation, developed in part from this project, has been used in the development of fluidic nozzle technology in the AFRL Internal Flow Control program (point of contact at Lockheed Martin: Brant.Ginn@lmco.com, 817.935.1033, point of contact at AFRL/VA: Denis.Mrozinski@va.afrl.af.mil, 937.656.6303), and in the evaluation and development of unsteady actuation techniques in the AFRL Active Weapons Bay Noise Suppression program (point of contact at Lockheed Martin: Tracy.J.Welterlen@lmco.com, 817.935.1127, point of contact at AFRL/VA: leonard.shaw@va.wpafb.af.mil, 937.255.5200).

### 11.4 Personnel

#### 11.4.1 Lockheed Martin Aeronautics Company

Propulsion Systems, Aerodynamics and CFD  
Mail Zone 9333  
P.O. Box 748  
Fort Worth, TX 76101

Researcher	Title	Role
Daniel N. Miller	Engineering Specialist Senior	Principal Investigator
Patrick J. Yagle	Engineering Analyst Senior	CFD Applications
Erich E. Bender	Engineering Specialist Senior	CFD Solvers and Applications
Brian R. Smith	Engineering Specialist Senior	CFD Turbulence Modeling

---

Kerry B. Ginn	Engineering Specialist Senior	Experimental Methods
---------------	-------------------------------	----------------------

---

11.4.2 University of Tennessee Space Institute

Mechanical and Aerospace Engr. Dept.  
Mail Stop 26  
Tullahoma, TN 37388-8897

---

<b>Researcher</b>	<b>Title</b>	<b>Role</b>
Ahmad D. Vakili	Professor	Pulse Actuator Test Evaluation
Abraham Meganathan	Graduate Student	Pulse Actuator Test Evaluation

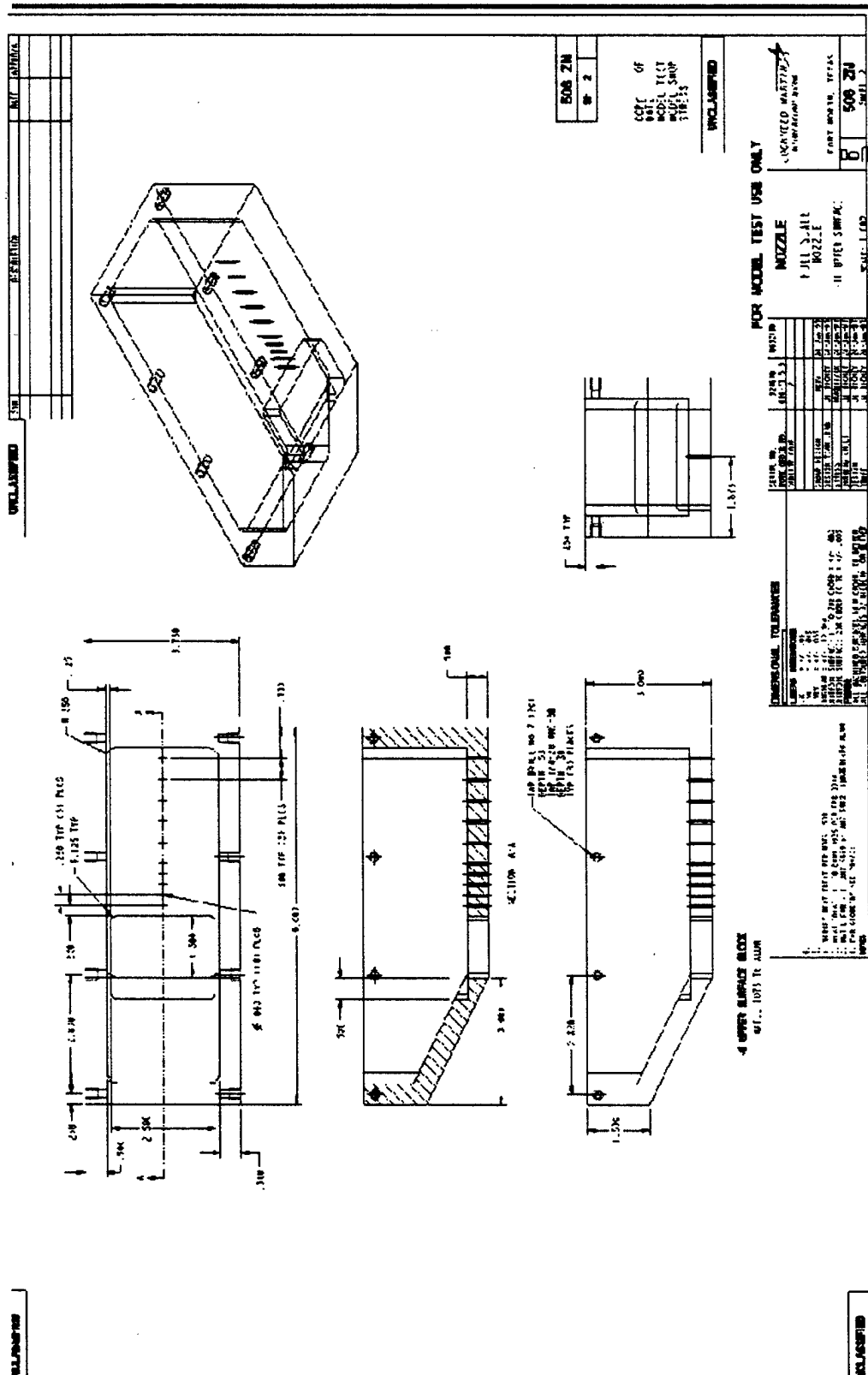
---

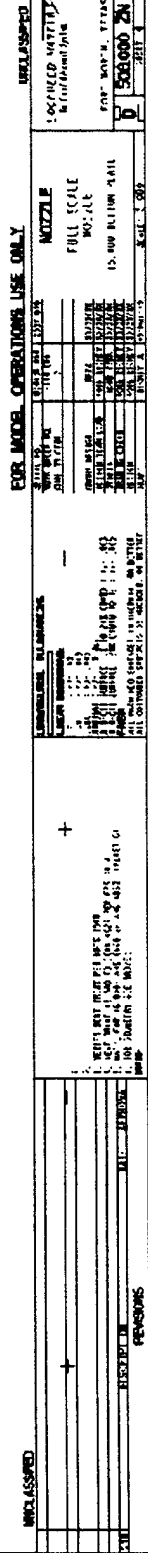
## 11.5 Model Drawings



FZM-8644  
05 February 2001

[illegible]





FZM-8644  
05 February 2001

[illegible]